Spring 2019

Laser welding of metallic glass to crystalline metal in laser-foil-printing additive manufacturing

Yingqi Li

Department: Mechanical and Aerospace Engineering

Recommended Citation

Li, Yingqi, "Laser welding of metallic glass to crystalline metal in laser-foil-printing additive manufacturing" (2019). *Doctoral Dissertations*. 2784.
https://scholarsmine.mst.edu/doctoral_dissertations/2784

LASER WELDING OF METALLIC GLASS TO CRYSTALLINE METAL IN LASER-FOIL-PRINTING ADDITIVE MANUFACTURING

by

YINGQI LI

A DISSERTATION

Presented to the Faculty of the Graduate School of the

MISSOURI UNIVERSITY OF SCIENCE AND TECHNOLOGY

In Partial Fulfillment of the Requirements for the Degree

DOCTOR OF PHILOSOPHY

in

MECHANICAL ENGINEERING

2019

Approved by:

Dr. Ming C. Leu, Advisor
Dr. Hai-Lung Tsai, Co-advisor
Dr. K. Chandrashekhara
Dr. Kelly Homan
Dr. Richard Brow

PUBLICATION DISSERTATION OPTION

This dissertation has been prepared using the Publication Option and consists of four journal papers.

Paper I, “*Building Metallic Glass Structures on Crystalline Metal Substrates by Laser-Foil-Printing Additive Manufacturing*”, on pages 13–44, has been published in *Journal of Materials Processing Technology*.

Paper II, “*Building Zr-based Metallic Glass Part on Ti-6Al-4V Substrate by Laser-Foil-Printing Additive Manufacturing*”, on pages 45–74, has been published in *Acta Materialia*.

Paper III, “*Additive Manufacturing of Zr-based Metallic Glass Structures on 304 Stainless Steel Substrates via V/Ti/Zr Intermediate Layers*”, on pages 75–104, has been published in *Materials Science and Engineering A*.

Paper IV, “*Mechanical Properties of Zr-based Bulk Metallic Glass Parts Fabricated by Laser-Foil-Printing Additive Manufacturing*”, on pages 105–129, has been published in *Materials Science and Engineering A*.

ABSTRACT

The application of metallic glasses has been traditionally limited to parts with small dimensions and simple geometries, due to the requirement of fast cooling during the conventional process of casting. In addition, joining metallic glass to crystalline metal is of interest for many applications that require locally tailored functions and properties, but it is challenging. This research describes a promising additive manufacturing technology, i.e., laser-foil-printing, to make high-quality metallic glass parts with large dimensions and complex geometries and to fabricate multi-material components from metallic glass and crystalline metal. In this research, $Zr_{52.5}Ti_5Al_{10}Ni_{14.6}Cu_{17.9}$ metallic glass parts are fabricated on different crystalline metal substrates, including pure Zr metal, Ti-6Al-4V alloy, and 304L stainless steel. The dissimilar bonding between the metallic glass part and the crystalline metal substrate is studied and then improved through the use of appropriate intermediate layers. The microstructure and properties of the fabricated metallic glass parts are also investigated. The results show that Zr can form a crack-free bonding with Zr-based metallic glass owing to the formation of ductile α-Zr phase, whereas direct joining of Zr-based metallic glass to Ti alloy or stainless steel fails due to the formation of various brittle intermetallic compounds. By using Zr intermediate layers for Ti substrates and V/Ti/Zr intermediate layers for stainless steel substrates, the formation of deleterious intermetallics is suppressed and thus the bonding between metallic glass and crystalline metal is significantly improved. Additionally, fully amorphous and nearly fully dense (~99.9%) metallic glass parts with comparable mechanical properties to as-cast parts have been successfully fabricated.

ACKNOWLEDGMENTS

First and foremost, I would like to express my sincere gratitude to my advisors, Prof. Ming C. Leu and Prof. Hai-Lung Tsai, for everything that they have done to help me get to where I am. Prof. Leu and Prof. Tsai are not only knowledgeable, enthusiastic, and hard-working researchers; they are also caring advisors and wonderful instructors. I am forever indebted to them.

Besides my advisors, I also thank the rest of my committee: Prof. K. Chandrashekhara, Prof. Kelly Homan, and Prof. Richard Brow. I appreciate their insightful comments and suggestions. I am grateful for financial support from the U.S. Department of Energy and the Intelligent Systems Center of Missouri S&T.

I am grateful to my group member, Dr. Yiyu Shen, for teaching me how to use the laser systems and characterization equipment. I would also like to thank my other group members, Dr. Chen Chen and Chia-Hung Hung, for their help in the lab. I value all the deep discussions I had with my group members in the lab.

I also thank Dr. Eric Bohannan for his help with XRD and DSC, Dr. Clarissa Wisner for her help with SEM, and Dr. Jeremy Watts for his help with the mechanical testing. I also appreciate all of the help I have received from Kyle Stagner, Brian Bullock, Ian Wille, Paul Brune, Deborah Sickler, and Lisa Winstead.

Last but not least, I thank my entire family for supporting me through this long journey: my parents, Xuejun Li and Nianlan Qi, my grandparents, Aisheng Li and Zhongying Qi, my sister, Juan Li. I could not have done this without their love and support.

TABLE OF CONTENTS

Page

SECTION

LIST OF ILLUSTRATIONS

PAPER I Page

PAPER II

PAPER III

PAPER IV

LIST OF TABLES

PAPER I Page

PAPER II

PAPER III

PAPER IV

SECTION

1. INTRODUCTION

1.1. OVERVIEW

Metallic glasses (MGs) usually exhibit many exceptional properties, such as high strength, elasticity, hardness, corrosion resistance, wear resistance, etc., compared to conventional crystalline metals. However, current applications of MGs are limited by small dimensions and simple geometries owing to the requirement of fast cooling during casting – the conventional method of bulk MGs manufacturing. Laser foil printing (LFP), a new additive manufacturing technology, has great potential for efficient production of high-quality MG parts with large dimensions and complicated geometries due to the high heating and cooling rates of laser processing, the intrinsic advantage of fabricating complex geometries with additive manufacturing technology, and the benefits of using metal foil as feedstock.

In LFP, crystalline metals have to be used as the substrates upon which MG parts are built, since thick, large as-cast MG plates are nearly impossible to produce. A good bonding between the MG and the crystalline metal is therefore critical for the success of the MG parts made by LFP. On the other hand, joining dissimilar materials is increasingly needed as engineering applications are seeking creative new structures with locally tailored functions and properties. The LFP technology provides a unique opportunity for directly building up a component with varied properties by welding dissimilar metal foils at different layers or locations during fabrication as desired. Such components are difficult to fabricate by casting or other conventional manufacturing technologies. The ability to manufacture multi-material net shapes from MG and crystalline metal will provide more flexibility in product design and manufacture, and will help create novel structures with optimized performance and reduced cost. A major challenge to building such multi-material components is to obtain a crack-free bonding between MG and crystalline metal, since direct fusion welding of MG to crystalline metal usually leads to the formation of various brittle intermetallic compounds.

In this dissertation, $Zr_{52.5}Cu_{17.9}Ni_{14.6}Al_{10}Ti_5$ MG parts have been fabricated on different crystalline metals substrates, including pure Zr metal, Ti alloy, and stainless steel, using LFP technology. The dissimilar bonding between MG and different crystalline metals have been studied and then improved through the use of appropriate intermediate layers. The microstructure and properties of the printed MG parts have been investigated. The overall goal of this dissertation was to understand and ultimately improve the dissimilar bonding between the selected MG and crystalline metals in the LFP process and to build high-quality fully amorphous MG parts. This research has built foundations for the production of MG parts with large dimensions and complex geometries, and for the manufacture of multi-material components from MG and crystalline metal using additive manufacturing technology.

1.2. BULK METALLIC GLASSES

Metallic glasses (MGs), also known as amorphous alloys, liquid metals, or glassy metals, are solid metallic materials with disordered atomic structures [1]. Traditional metals, such as Ti alloys and steels, are crystalline in the solid state, which means they have a highly ordered and repeating arrangement of atoms. The atomic configurations of molten metals are disordered. Upon solidification of a molten metal, crystallization usually occurs. However, if the molten metal is cooled down fast enough, the formation of equilibrium crystalline phases can be suppressed and a disordered atomic configuration similar to liquid structure can be maintained down to room temperature [2]. Thus, MGs can be formed if crystallization is avoided during solidification. The amorphous nature of MGs endows them with many exceptional properties, such as high strength, elasticity, hardness, corrosion and wear resistance, etc. [3-5].

For a molten metal, there is a critical cooling rate from above the melting point to below its glass transition temperature necessary to suppress crystallization. For early MGs, because metal melts crystallize so rapidly owing to their high atomic mobility, the critical cooling rates are on the order of 10^5–10^6 K/s [6]. They are usually fabricated by rapid solidification techniques, e.g., the melt spinning method [2]. Due to the high critical cooling rates, early MGs could only be tens or hundreds of microns thick, which is too thin for many practical applications. The thickness limitations have been drastically reduced by the discovery of bulk MG (BMG) alloy compositions, which require much lower critical cooling rates (as low as ~ 0.1 K/s). The significantly reduced critical cooling rate or improved glass-forming ability of BMGs is achieved through correct choice of constituent elements [2]. BMGs are usually designed based on binary alloy systems with deep eutectics, such as Cu–Zr and Zr–Be [7]. For an alloy with deeper eutectic (lower meting temperature), it is easier to cool the molten metal below the glass transition temperature without allowing enough time for crystal nucleation and growth [7]. In addition, most of BMGs are comprised of 4–5 elements. Since four or more elements are involved during solidification, it is difficult to select a viable crystal structure, and hence the glass-forming ability is improved, which is called the “confusion principle” [2]. The excellent glass-forming ability of BMGs also has been generally attributed to the large differences in atomic size between constituent elements, which leads to large atomic packing density and thus greater stability. The dramatic decrease in the critical cooling rate has enabled the production of thicker MG parts, as well as a drastic change in the production method of MG from melt quenching to copper mold casting [8,9]. The maximum thickness of glass formation achieved by copper mold casting has reached as large as > 10 mm for BMGs based on Zr, Pd, Pt, Mg, La, Ni and Cu, and > 5 mm for BMGs based on Fe, Co and Ti [6].

Due to the requirement of critical cooling rates for amorphous formation and the limitation of heat conduction, there is a maximum thickness of glass formation that can be achieved by casting for a BMG alloy composition. As heat can only be dissipated from the outer surface of an ingot to its surroundings, heat at the internal locations must be transferred by conduction to the outer surface. Therefore, the cooling rates, which are controlled by the metal’s thermophysical properties (e.g., thermal conductivity), are different across the entire cross-section of an ingot during casting. The outer surfaces have the highest cooling rate, while the center has the lowest cooling rate. If the cooling rate of the center is larger than the critical cooling rate, the entire ingot will be amorphous. However, when the part has a large cross-section area, the center cannot achieve the critical cooling rate for amorphous formation. This greatly limits the fabrication of large-size MG parts by casting. In addition, only a limited range of geometries can be fabricated through direct casting of MGs [3]. This is because fast cooling is necessary for amorphous formation, whereas ideal molding conditions require slow filling of mold cavity for complex geometries. The small dimensions and simple geometries of as-cast MG products limit their applications. To exploit the potential of MGs, it is necessary to develop new processing methods for the production of MG parts with larger dimensions and complex geometries.

1.3. ADDITIVE MANUFACTURING OF METALLIC GLASS PARTS

Laser-based additive manufacturing technology has the potential to overcome the size and geometry limitations imposed by casting MG products. First, the ability to fabricate 3D parts with intricate geometries is the intrinsic advantage of additive manufacturing, since it builds 3D parts by depositing materials layer-by-layer [10]. In addition, during additive manufacturing of a MG part, the “casting” process is “separated” into a series of thin layers, which means that the requirement of high cooling rates can be decoupled from the part dimensions in additive manufacturing [11]. Theoretically, as long as high cooling rates can be fulfilled in each layer, MG parts of any dimension can be made. On the other hand, in laser material processing, as a large amount of energy is focused onto a very small area, the heating and cooling rates could be as high as 10^4–10^5 K/s [12], which greatly facilitates the formation of an amorphous layer.

Laser-based additive manufacturing of MG parts from Zr-based and Ti-based MGs with good glass-forming ability as well as Fe-based MGs with poor glass forming ability has been studied in the literature [11,13–25]. Most of these studies were conducted using selective laser melting (SLM) in which metal powder is used as feedstock material and a part is made by laser melting of selected areas of the powder bed pass-by-pass and layer-by-layer. SLM is widely used to build high density parts for crystalline metals. However, when using SLM to fabricate MG parts, it is challenging to reduce the porosity and make the part fully amorphous at the same time [11]. This is because of the low power bed density which leads to as much as 40–50% free space in the initial powder bed [26]. Such high percentage of free space results in much lower thermal conductivity of the powder bed than the bulk material. For example, for a 316L stainless steel powder bed, the measured thermal conductivity is only around 0.3–5% of that of the bulk material [27]. Because of such low thermal conductivity, heat cannot be rapidly removed if the laser energy input is large. Therefore, to suppress crystallization, small laser energy input is required when processing MG. On the other hand, owing to the high percentage of free space, large effort is needed to remove the entrapped gas in the powder bed. Generally, higher laser energy input is desired to fully melt powder and reduce porosity, but this might cause crystallization of MG.

Metal foil also can be used as feedstock material for additive manufacturing, which has advantages over metal powder for additive manufacturing of MG parts. Unlike a metal powder bed with large empty space, foils have no pores inside. Therefore, at the same or similar laser processing conditions, because of the higher thermal conductivity of foil than the powder bed, the heating and cooling rates should be higher when using foil [21,27]. In addition, less effort is needed to reduce porosity when using foil since there is less entrapped gas compared to a powder bed [21,28,29]. Hence, by using foil as feedstock, it is possible to further reduce the porosity of an additive manufactured MG part without sacrificing its fully amorphous structure. In this dissertation, MG foil was utilized as feedstock to build MG parts by using a newly developed additive manufacturing technology, called laser-foil-printing (LFP), in which a 3D part is built by laser welding of metal foils layer-by-layer in selected areas and laser cutting of metal foils along the contour of the welded areas [21,30]. In a previous publication, we have demonstrated the capability of LFP technology to fabricate fully amorphous, high density, and crack-free Zr-based MG parts with 3D geometries and dimensions exceeding the maximum thickness achieved by casting [21]. This dissertation was focused on the microstructure, thermal properties, and mechanical properties of the fabricated MG parts, to demonstrate the potential of the LFP technology for achieving high-quality MG parts.

1.4. JOINING OF METALLIC GLASS TO CRYSTALLINE METAL

In LFP additive manufacturing technology, a large and thick metal plate may need to be used as the foundation substrate upon which additional materials are added layer-by-layer to build the 3D part. For LFP of MG parts, conventional crystalline metals, such as Ti alloys, steels, have to be used as substrates, because it is difficult or even impossible to produce large and thick MG plates by casting. To successfully build a MG part on a crystalline metal substrate, creating a strong bonding between the MG and the crystalline substrate is crucial; otherwise, with the accumulation of residual stresses, the welded MG foils would peel off from the substrate before the desired part is fully built.

On the other hand, multi-material components are highly desirable in applications in which the required properties vary with location, but rarely does a single material meet all these requirements [31]. The freeform fabrication nature of additive manufacturing enables building net-shaping components from multiple materials by depositing different materials at different desired layers or locations to achieve the desired properties changes. Such components are difficult or impossible to fabricate by conventional manufacturing methods. As a sheet lamination technology, LFP provides a unique possibility for directly manufacturing a freeform component consisting of multiple materials. Theoretically, any metal which can be laser welded is a candidate material for LFP. Multi-material components can be produced by welding various metal foils at different desired layers or locations during LFP. Resultant property change therefore can be obtained to meet various application needs. For example, by changing materials it is possible to optimize corrosion resistance, strength, ductility, and other properties at specific locations within a component.

Despite high hardness, strength, corrosion resistance, etc., MGs lack macroscopic plasticity because they do not have microstructures or other stabilizing features to arrest a slipping shear band and nucleate another [32]. For example, $Zr_{52.5}Cu_{17.9}Ni_{14.6}Al_{10}Ti_5$ MG has a yield strength of ~1524 MPa, a Vickers micro-hardness of ~563 HV, and superior corrosion resistance to 316 stainless steel, but it shows negligible tensile ductility (~1.6%) (data source: Liquidmetal® datasheet). In addition, many commercially available BMGs are costly since they are made from expensive, high purity metals, e.g., Zr. In addition to size and geometry limitations, these factors also limit the applications of MGs. Hence, the ability to manufacture multi-material components from MG and conventional crystalline metal, e.g., Ti alloys, stainless steels, etc., would either help extend the applications of MGs or provide additional functions to the crystalline metal components.

No matter for which motivation mentioned above, obtaining a good dissimilar bonding between MG and crystalline metal is critical, but this is very challenging due to the large differences in physical and chemical properties between MG and crystalline metal [33]. Direct fusion welding of MG to crystalline metal usually leads to the formation of brittle intermetallic compounds, which could result in crack or even fracture of the bonding. To achieve low critical cooling rates, BMG alloy compositions usually consist of more than three elements, e.g., $Zr_{52.5}Cu_{17.9}Ni_{14.6}Al_{10}Ti_5$. Owing to lack of solubility and atomic structure mismatch between different elements, when welding such MGs to dissimilar metals, various detrimental intermetallic phases could form at the interface. Laser welding of MG to same MG has been extensively studied [34-53]. On the other hand, laser welding of MG to crystalline metal is rarely reported. Several studies on the electron beam welding of MG to crystalline metal can be found in the literature. Kagao et al. studied the electron beam welding of a Zr-based MG plate to a Ti alloy and to a Zr alloy plate, but only succeeded to form a crack-free bonding between MG and Zr due to the formation of α-Zr whereas the welded MG and Ti plates formed a very brittle interface due to the formation of intermetallics [54]. Using electron beam welding, Kim et al. successfully welded a Zr-based MG plate to a Ti plate [55], to a Ni plate [56], and to a stainless steel plate [57] without the formation of interfacial intermetallics. The method they adopted to avoid the formation of intermetallics was to minimize the melting of crystalline plates through the adjustment of the beam irradiation position or the joint geometry. However, the considerable melting of underlying crystalline substrate is unavoidable in LFP technology. Thus, minimizing the melting of crystalline substrate is not a feasible way for LFP to avoid the formation of detrimental intermetallics. Instead, a feasible way to reduce the brittleness caused by the formation of intermetallics is to use intermediate metal at the bonding interface that is compatible with both the crystalline metal and MG. Therefore, in this dissertation, based on binary phase diagrams, specific transition routes have been designed from Zr-based MG to specific crystalline metal, i.e., Ti alloy, or stainless steel, to improve the dissimilar bonding and the designed transition routes have been experimentally verified.

1.5. ORGANIZATION OF DISSERTATION

In this dissertation, $Zr_{52.5}Ti_5Al_{10}Ni_{14.6}Cu_{17.9}$ metallic glass (MG) parts were fabricated on different crystalline metal substrates, including pure Zr metal, Ti-6Al-4V alloy and 304L stainless steel, using LFP additive manufacturing technology. $Zr_{52.5}Ti_5Al_{10}Ni_{14.6}Cu_{17.9}$ MG was selected for this study since it has excellent glass-forming ability and is commercially available. In addition, this MG exhibits very high strength (a yield strength of ~1524 MPa), high hardness (Vickers ~563 HV), large elasticity (~1.8%), and superior corrosion resistance to 316 stainless steel and titanium [58]. It has potential application in biomedical implants, medical devices, sporting goods, etc. This dissertation focused on understanding the dissimilar bonding between MG and different crystalline metals and how to improve those dissimilar joints. The microstructure, thermal properties, and mechanical properties of the fabricated MG parts by LFP were also investigated. This dissertation consists of four papers as follows:

In the first paper, we tested the suitability of two materials, i.e., pure Zr metal and Ti-6Al-4V alloy, as substrates for LFP of Zr-based MG parts. Weldability studies for laser welding of Zr-based MG to pure Zr and Ti-6Al-4V alloy were conducted. Factors affecting the dissimilar bonding are discussed. The results show that Zr is a suitable substrate for Zr-based MG part since crack-free weld joints could be obtained owing to the formation of ductile α-Zr phase, whereas Ti is not an appropriate substrate since the dissimilar bonding between Ti and Zr-based MG has high cracking susceptibility due to the formation of a large amount of hard and brittle intermetallics.

In the second paper, the dissimilar bonding between Zr-based MG part and Ti-6Al-4V substrate was improved by using Zr intermediate layers. From the results obtained in the first paper, we saw that the joints made between Zr-based MG and Ti alloy were brittle due to the formation of brittle intermetallics, whereas Zr could be directly welded to Zr-based MG without cracking. In addition, mixtures of Ti and Zr form solid solutions, instead of intermetallics, over the complete composition range in their binary phase diagram. Therefore, pure Zr intermediate layers that were placed between Zr-based MG part and Ti substrate prevented the formation of undesirable intermetallics.

In the third paper, the dissimilar bonding between Zr-based MG and 304L stainless steel was studied and improved by using intermediate layers. The direct welding of MG on stainless steel would lead to the formation of various brittle intermetallics and the consequent peeling off of the welded MG foils from the SS substrate. This was resolved by the use of V/Ti/Zr intermediate layers. The transition route SS → V → Ti → Zr → MG was designed based on the results obtained in the second paper and because V is completely soluble in both Ti and Cr, and considerably soluble in Fe, according to their binary phase diagrams.

In the fourth paper, the microstructure, density, thermal properties, and mechanical properties of the MG parts fabricated by LFP were studied, in order to demonstrate the potential of LFP for achieving high-quality MG parts. The results show that LFP is able to produce fully amorphous and nearly fully dense MG parts with mechanical properties comparable to parts made by conventional casting.

The last section of this dissertation is a summary of this research, the major conclusions drawn from these studies, and some suggestions for future work in this area.

PAPER

I. BUILDING METALLIC GLASS STRUCTURES ON CRYSTALLINE METAL SUBSTRATES BY LASER-FOIL-PRINTING ADDITIVE MANUFACTURING

Yingqi Li, Yiyu Shen, Chen Chen, Ming. C. Leu, and Hai-Lung Tsai

Department of Mechanical and Aerospace Engineering, Missouri University of Science
and Technology, Rolla, MO 65409, United States

ABSTRACT

In laser-foil-printing additive manufacturing, 3D metallic glass structures can be built by laser welding of amorphous foils, layer by layer, upon a crystalline metal substrate. In this paper, weldability studies for laser welding of $Zr_{52.5}Ti_5Al_{10}Ni_{14.6}Cu_{17.9}$ amorphous foils onto a Ti-6Al-4V (Ti 6-4) or Zr 702 substrate are conducted. After laser welding, the weldments are analyzed using X-ray diffractometer, optical microscope, scanning electron microscope equipped with energy dispersive spectroscopy and micro-hardness tester. The results show that Zr 702 is a suitable substrate for Zr-based metallic glass structure since crack-free weld joints can be obtained owing to the formation of ductile α-Zr, while Ti 6-4 is not an appropriate substrate since it has high cracking susceptibility due to the formation of a large amount of hard and brittle intermetallics near the foil-substrate interface. It was found that the mixing between melted substrate and foil is not uniform but exhibits a distinct “swirl” pattern. The swirl structure is more pronounced in Ti 6-4 than in Zr 702 substrate which may contribute to its high cracking

susceptibility. The aforementioned mixing leads to partial crystallization of the first amorphous layer; however, fully amorphous is achieved in the additional welding layers.

1. INTRODUCTION

Amorphous alloys, or metallic glasses (MGs), exhibit many superior properties, such as high strength, elasticity, hardness, corrosion resistance, etc., as compared with conventional crystalline metals (Inoue, 2001). Currently, MG parts are mainly fabricated by direct mold casting or thermoplastic forming that takes the advantage of considerable softening of an MG in its supercooled liquid state (Schroers, 2010). Fast cooling is necessary to the mold casting of an MG part for achieving amorphous phase; however, ideal molding conditions require slow filling. Thus, casting of MG parts with large sizes and/or intricate shapes is difficult (Wang et al., 2004). In addition, the use of thermoplastic forming is rather limited due to the very high viscosity of supercooled liquid during the net shaping of MG parts with complex shape (Chen et al., 2014). So far, it is still a huge challenge to fabricate MG parts in complex geometries with section-thickness of more than a few centimeters or even millimeters.

Due to the advantages of high heating/cooling rates and non-contact processing, laser-based additive manufacturing (AM) is a promising technology to build 3D MG structures with complex geometry and large size. In a recently developed laser-based AM technology, called laser-foil-printing (LFP), a laser is used to weld metal foils, layer-by-layer, upon substrates to produce 3D parts (Chen et al., 2016). The LFP technology shows its unique advantages on the fabrication of 3D MG structures over powder-based

AM methods since the heating and cooling rates can be much higher, particularly in the heat-affected zone (HAZ). The method, system and procedure for LFP to construct 3D MG structures were discussed in authors' other publication (Shen et al., 2017).

Normally, a large, thick metal is used as the foundation substrate in an AM technology upon which additional materials are gradually added. Since it is difficult or even impossible to obtain large, thick amorphous plates, conventional crystalline metals have to be used as substrates. As dissimilar metals have different chemical compositions and thermal properties, the weldability between the first layer of amorphous alloy foil and the crystalline metal substrate is critical for the success of the MG structure by LFP. In addition, in some occasions it may be necessary to weld amorphous foils on or around crystalline metals in order to take advantages of the specific properties of each metal. For example, if a steel pillar is welded and wrapped around by an amorphous layer, the steel would be protected from possible corrosion or wear at its surfaces.

Compared with the numerous reports on alloy compositions and properties of MGs, there are relatively fewer publications on the welding of MGs, especially to crystalline metals. Welding methods of MGs can be generally divided into two groups: solid state welding and liquid phase welding. Solid state welding methods of MGs mainly include friction welding (Wang et al., 2012) and diffusion welding (Wen et al., 2015). For liquid phase welding of MGs, the method mainly includes electron beam welding and laser beam welding which have high heating and cooling rates. Kawamura et al. (2003) successfully joined Zr-based MGs plates without crystallization using electron beam welding. They also attempted electron beam welding of Zr-based MG plate to Ti alloy or Zr alloy plate, but only Zr alloy was successfully welded to Zr-based MG without defects. Based on these studies, Zr-based MG plate was successfully welded to Ti plate (Kim and Kawamura, 2007), Ni plate (Kim and Kawamura, 2008), or stainless steel plate (Kim and Kawamura, 2011) using electron beam welding, by minimizing the melting of crystalline plates through adjusting the beam irradiation position or the joint geometry. Some studies have been conducted on laser welding of MGs to MGs. For example, Wang et al. (2010) attempted laser welding of $Zr_{53}Cu_{30}Ni_9Al_8Si_{0.5}$ MG plate in bead-on-plate form, and they found that the heat affected zone was more liable to crystallize than the weld fusion zone and crystallization-free weldment can be produced using a liquid cooling device. Kim et al. (2006) investigated the phase evolution of Cu-based MG in laser welding, and found that the increase of laser energy deposition and concomitant decrease of cooling rate and chemical composition change of MG weld would enhance the crystallization susceptibility of the weld metal. However, there are few publications on laser welding of MGs to crystalline metals. In addition, no matter for electron beam welding or laser welding of MGs, almost all previous studies are focused on single-pass welding in butt-joint or bead-on-plate form. In LFP technology, multi-pass welding, which has much more complicated thermal history and mass transport than single pass welding, and lap-joint, in which the melting of underlying substrate is considerable, have to be adopted and investigated.

In this study, $Zr_{52.5}Ti_5Al_{10}Ni_{14.6}Cu_{17.9}$ amorphous foils were laser welded onto a Ti-6Al-4V (Ti 6-4) or Zr 702 (commercially pure Zr) substrate to construct MG structures using LFP, and this paper will focus on the study of dissimilar metals welding between the first layer of amorphous foil and substrate. As the main element of the selected amorphous foil is Zr, Zr 702 was chosen as the substrate. Ti alloy was chosen for the reason that Zr is completely soluble with Ti in both liquid and solid phases (Massalski et al., 1986), and Ti 6-4 is the most common Ti alloy. In the following, parametric studies of laser welding of Zr-based amorphous foil onto a Ti 6-4 or Zr 702 substrate were first conducted, and then the weldability of amorphous foil to Ti 6-4 or Zr 702 substrate was discussed and analyzed.

2. EXPERIMENTAL

The thickness of as-received $Zr_{52.5}Ti_5Al_{10}Ni_{14.6}Cu_{17.9}$ (at. %) (Liquidmetal® LM105) amorphous foils was approximately 100 µm, while the thickness of Ti 6-4 or Zr 702 substrate plate was 3.5 mm. Table 1 shows the nominal chemical compositions of Ti 6-4 and Zr 702. Before laser processing, the substrates and foils were first grinded using silicon carbide papers to remove surface oxides, and then cleaned using ethanol.

Table 1. Nominal chemical compositions of Ti 6-4 and Zr 702 (wt.%).

Ti 6-4	**Ti**	**Al**	**V**	**Fe**	**H**	**N**	**C**	**O**
	87.69 - 91.00	5.50 - 6.75	3.50 - 4.50	≤ 0.30	≤ 0.0125	≤ 0.05	≤ 0.10	≤ 0.2
Zr 702	**Zr + Hf**	**Hf**	**Fe + Cr**	**H**	**N**	**C**	**O**	-
	≥ 99.2	≤ 4.5	≤ 0.2	≤ 0.005	≤ 0.025	≤ 0.05	≤ 0.16	-

The LFP system developed at the Laser-Based Manufacturing Lab, Missouri S&T, as shown in Figure 1, was used in this experiment. This system mainly consists of two lasers: a continuous wave fiber laser (IPG YLP-1000) with 1070 nm wavelength for foil-welding and a pulsed UV laser (Coherent AVIA-355X) with 355 nm wavelength and 30 ns pulse duration for foil-cutting. In this study, the welding laser beam entered a scanner (SCANLAB) and then was focused on the foil surface through an F-theta lens with an equivalent focal length of 33 cm, and the beam diameter (D, defined at $1/e^2$ of the maximum intensity) at the focus was about 170 µm. The substrates were mounted on a computer controlled three-axis motion stage (Aerotech). A layer of foil was placed and fixed on the substrate via laser spot welding using a mold-plate with a predetermined hole-pattern (see Figure 2(a)). As the foil thickness was about 100 µm, two sheets of foil were used as one layer to increase efficiency and construction speed. Hence, a layer of foil was approximately 200 µm thick. Then, the scanner scanned multi-passes to weld the foil onto the substrate, as shown in Figures 2(b) and 2(d). After the welding process was done, the motion stage shifted the workpiece to the location under the UV laser and the foil was cut by the UV laser along the contour of the welded region to remove the redundant foil (see Figure 2(c)). Another layer of fresh foil can be placed on the top of the workpiece for the process of next layer if needed. More details for the system, method, and procedure of the LFP technology can be found in Ref. (Chen et al., 2016). For each of the laser power for welding, i.e., P = 300, 400, or 500 W, the laser scan speed (v) was selected to achieve three desired values of heat input, i.e., Q = 1.25, 1 or 0.85 J/mm, where $Q = P/v$. For example, if P = 400 W, v = 470 mm/s would be selected to achieve Q = 0.85 J/mm. For Ti 6-4, the hatch space (Δd) was 0.25 mm. For Zr 702, Δd was 0.25 mm when Q = 1.25 or 1 J/mm and 0.2 mm when Q = 0.85 J/mm. To reduce heat accumulation, the time lapse between two adjacent scan passes was 10 s. In other words, after finishing, for example, the first pass of line-welding, the laser stopped for 10 s and then the second pass of line-welding began with the starting point aligned with the first pass. No extra cooling method was used during the fabrication; however, all samples were processed inside a chamber with Ar shielding gas flow.

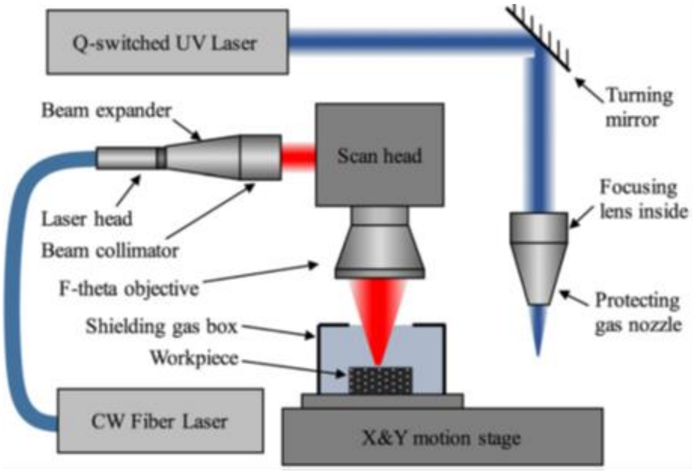

Figure 1. Schematic of the LFP system at the Laser-Based Manufacturing Lab, Missouri S&T. Reprinted from Ref. (Chen et al., 2016).

After laser welding, X-ray diffractometers (XRD, Philips X'pert MPD), optical microscope (OM, Nikon Epiphot 200), and scanning electron microscope (SEM, Helios Nano Lab 600) equipped with energy dispersive spectroscopy (EDS, Oxford AZtec) were used to analyze the microstructure, penetration depth and chemical composition. The sample surface area for XRD test was 10×10 mm^2. The metallographic specimens for OM and SEM were prepared by sectioning, mounting, grinding, mechanical polishing, and then etching with a solution of 100 ml H_2O, 5 ml H_2O_2, and 2 ml HF for Ti 6-4, or chemical attack polishing with a solution of 250 ml H_2O, 22 ml HNO_3, and 3 ml HF for Zr 702. The micro-hardness was determined using Vickers micro-hardness tester (Struers, Duramin 5) with 490.3 mN load and 5 s load duration.

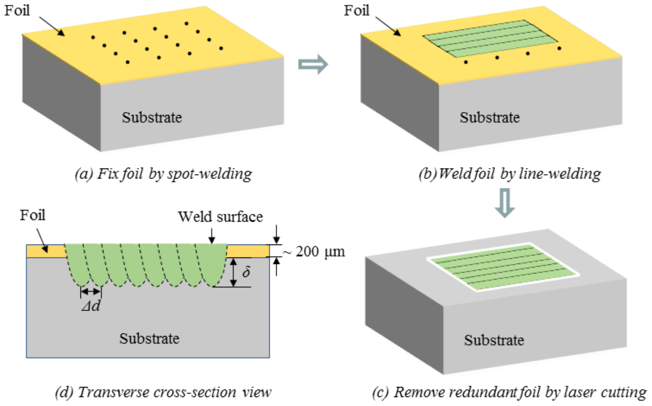

Figure 2. (a–c) Schematic of the experimental procedure and (d) schematic cross-section view of the dissimilar metals joint with one layer of amorphous foil. *Δd* is the hatch space, and *δ* is the penetration depth.

3. RESULTS AND DISCUSSION

3.1. LASER WELDING OF LM105 FOIL ONTO Ti 6-4 SUBSTRATE

Figure 3 shows the weld surface obtained when heat input Q = 1.25, 1 or 0.85 J/mm and each Q value has a combination of different laser powers (P) and laser scan speeds (v). For Q = 1.25 J/mm, it can be seen in Figures 3(a), 3(d), and 3(g) that transverse long cracks formed across the weld surface. For Q = 1 J/mm, discontinuous short cracks can be observed at the weld toe between two adjacent passes, as shown in Figures 3(b), 3(e), and 3(h). However, if Q is decreased to 0.85 J/mm, there is no cracking on the weld surface (see Figures 3(c), 3(f), and 3(i)).

Figures 4 through 6 show the cross-sections perpendicular to (transverse) or parrallel with (longitudinal) the laser scan direction at P = 500, 400 and 300 W, respectively. It should be noted that the longitudinal cross-section may not certainly show the centerline plane of the welding pass. For Q = 1.25 or 1 J/mm, cracks formed in the weld metal, as shown in subfigures (d) and (e) for Figures 4 through 6. For $Q = 0.85$ J/mm, even though cracking was not observed on the weld surface (see Figures 3(c), 3(f), and 3(i)), but cracks formed at the bottom of the weld metal (see subfigure (f) on Figures 4 through 6).

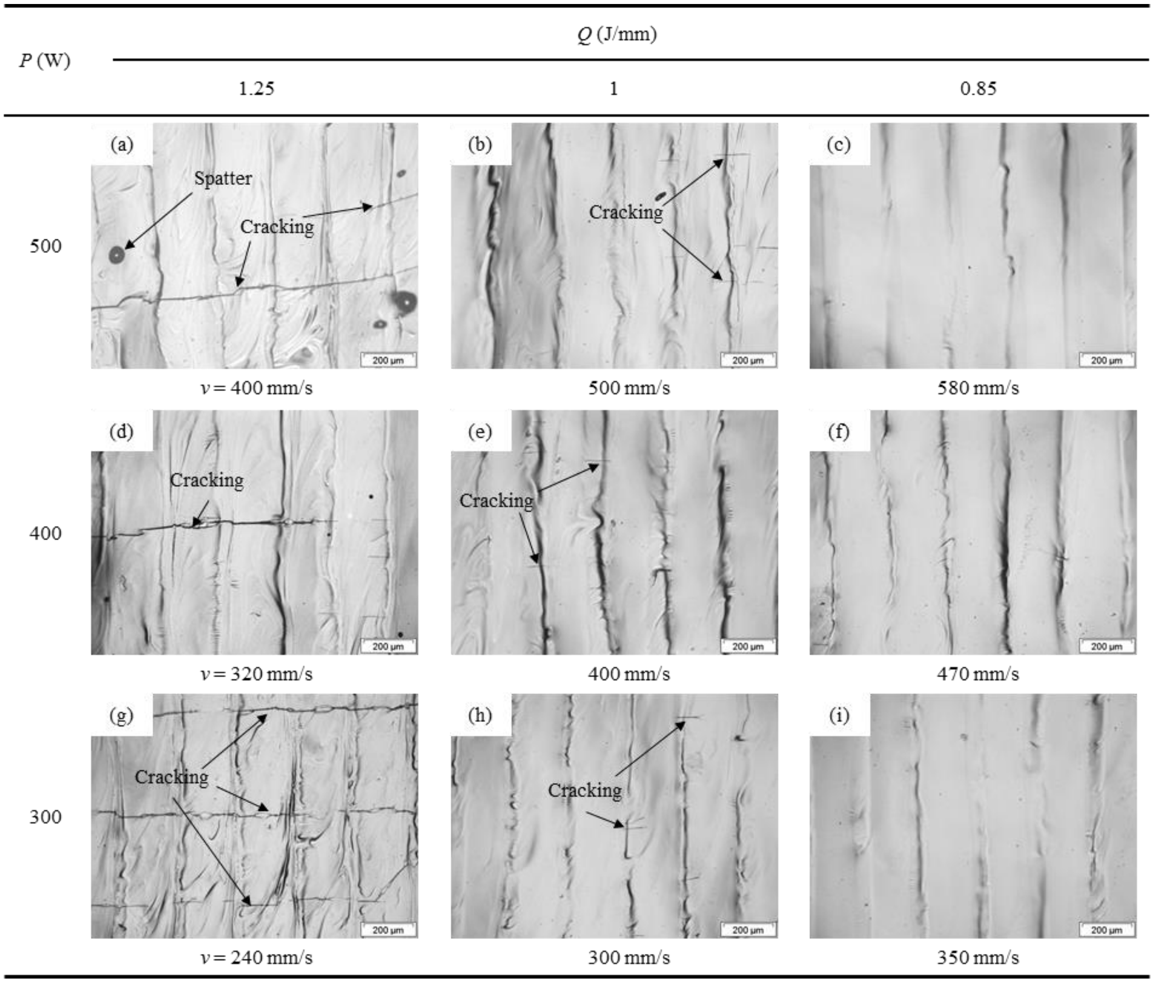

Figure 3. OM images of the weld surface obtained when heat input $Q = 1.25$, 1 or 0.85 J/mm with different laser powers, P, and laser scan speeds, v; Ti 6-4 substrates.

The laser intensity (I) used in this experiment was larger than 10^6 W/cm^2, where $I = P/(\pi D^2/4)$ (Steen and Mazumder, 2010). Such high laser intensity vaporized the metal during welding to form a deep hole from the surface down to the depth of the weld, which is called the keyhole, resulting in a deep weld with high depth-to-width ratio (Zhou et al., 2006), as shown in the transverse cross-section images of Figures 4 through 6. The keyhole characteristic is more pronounced at higher Q value, i.e., higher depth-to-width ratio at higher Q. From Figures 4 through 6, it can be seen that the penetration depth (δ) increases with the increase of Q or the decrease of v under the same P, as expected. When Q is constant, there is no significant difference in δ for Q = 1 or 0.85 J/mm, even though at different P or v values. However, for Q = 1.25 J/mm, δ increases as P increases, which may be caused by more severe keyhole effects because of a higher Q. In a keyhole-mode welding, the molten metal flow plays an important role in energy and mass transport (Zhou et al., 2006). All cross-section images show “frozen” convection swirls indicating the poor mixing between Ti 6-4 and Zr-based foil with significant variation of compositions in the welds. The swirled pattern is much more pronounced at higher Q values (more toward keyhole-welding). Since the time for melting and solidification is short during laser welding, a non-equilibrium condition may exist, which implies that the equilibrium phase diagrams are of little assistance for interpreting these results. In a short interaction time, there may be an apparent miscibility gap between certain compositions (Seretsky and Ryba, 1976).

Moreover, lack of fusion is observed between the adjacent passes because Δd = 0.25 μm is too large for Q = 0.85 J/mm (see subfigure (c) for Figures 4 through 6). The lack of fusion defect can be eliminated by reducing Δd. However, even though the adjacent passes are not overlapped at the interface between the foil and the substrate for Q = 1.25 or 1 J/mm (indicated by the white arows in subfigures (a) and (b) for Figures 4 through 6), lack of fusion does not occur. In order to determine whether metallurgical bonding was formed, SEM images were then taken and EDS line analyses were conducted for those unoverlapped areas, as shown in Figure 7. It shows that the composition changed gradually at the interface (Figure 7(b)) and the metallugical bonding was formed. LM105 has a much lower melting point (800 °C) than Ti 6-4 (1604 °C), and additionally as a kind of metastable material, amorphous alloys can accelerate atomic diffusion and surface reaction (Liu et al., 2013). As a result, a brazing process occurred between the foil and the substrate in the unoverlapped area when a higher *Q* was applied.

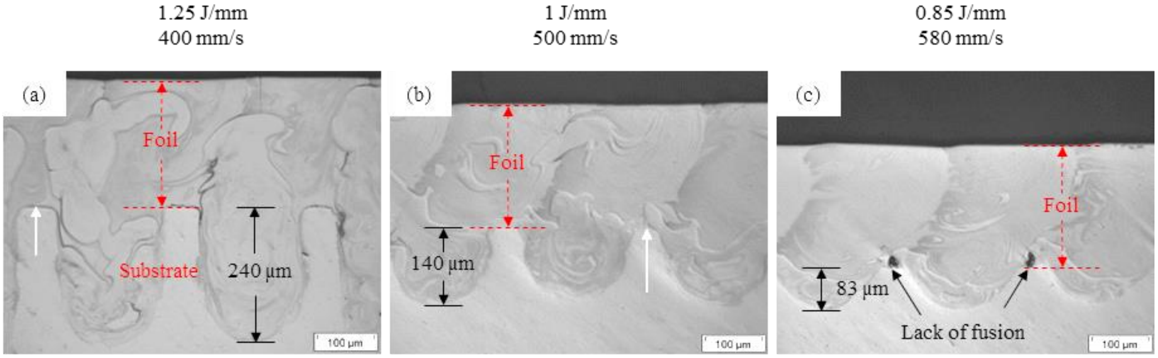

Cross-section perpendicular to the laser scanning direction

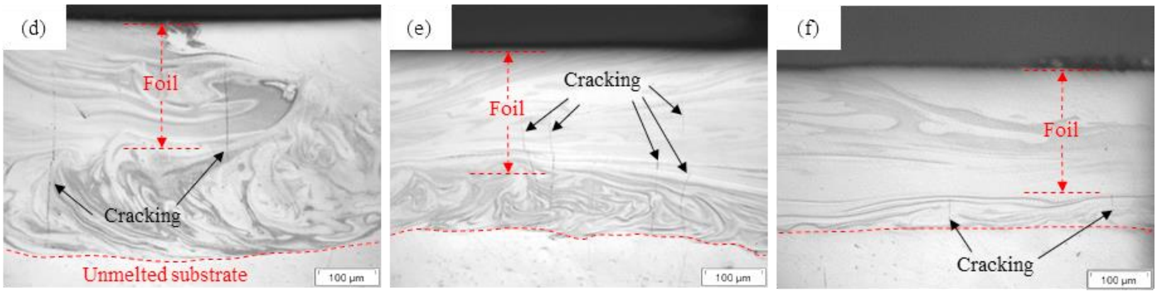

Cross-section parallel with the laser scanning direction

Figure 4. OM images of the cross-sections obtained when *P* = 500 W; Ti 6-4 substrates.

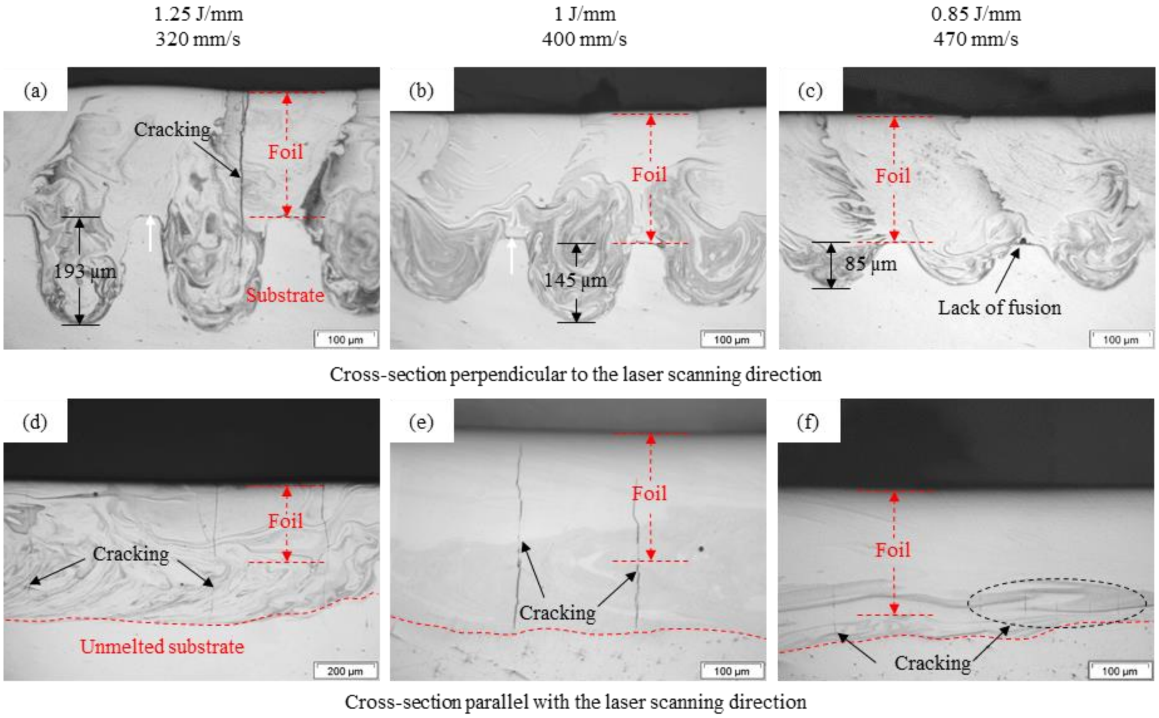

Figure 5. OM images of the cross-sections obtained when *P* = 400 W; Ti 6-4 substrates.

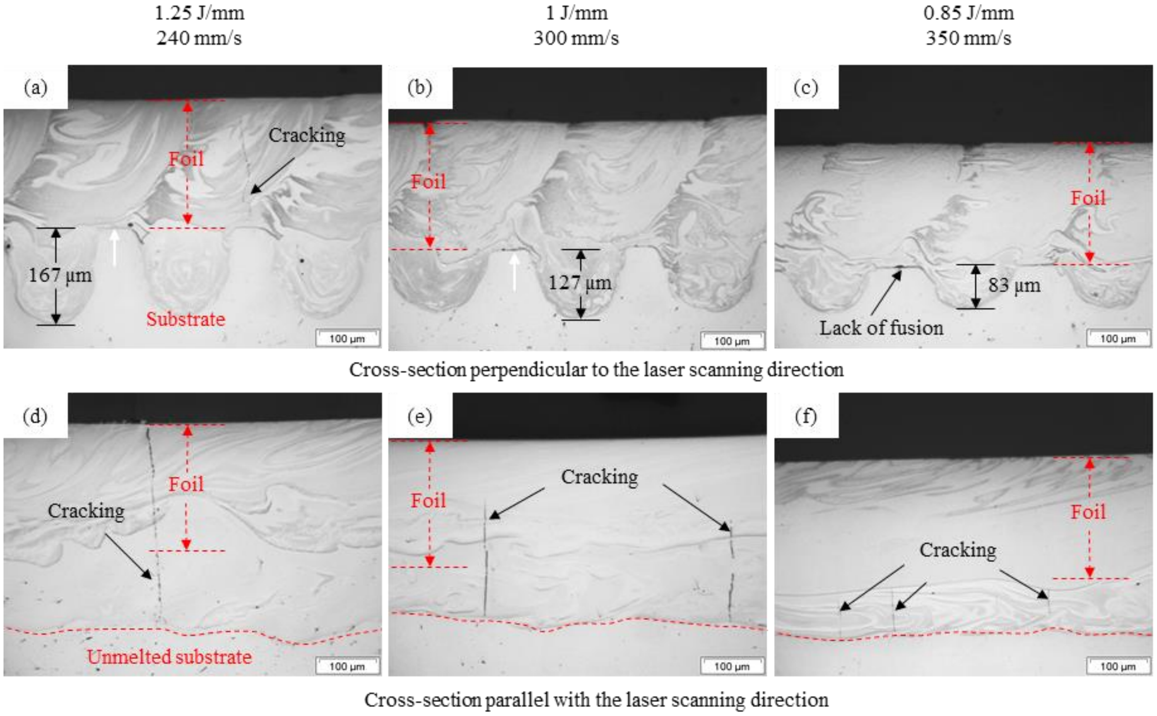

Figure 6. OM images of the cross-sections obtained when *P* = 300 W; Ti 6-4 substrates.

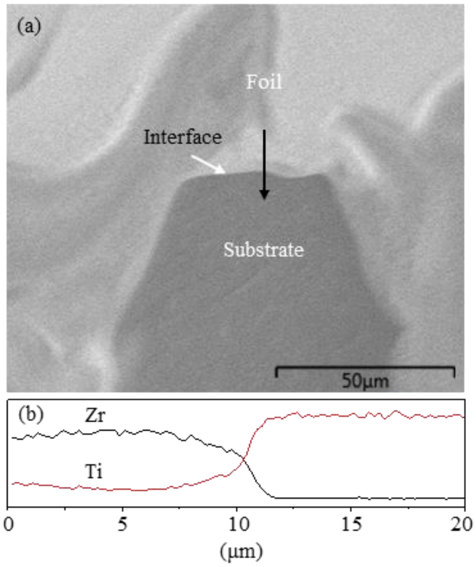

Figure 7. (a) SEM image of the unoverlapped area at the interface and (b) chemical composition distribution along the black arrow when *P* = 500 W and *v* = 500 mm/s; Ti 6-4 substrate.

The XRD patterns of the weld surfaces obtained for *Q* = 1 or 0.85 J/mm are shown in Figure 8. The fact that the sharp Bragg peaks overlapping with the broad peaks indicates that the amorphous foils were partially crystallized after laser welding under the processing parameters. Figure 9(a) shows the backscattered electron image (BEI) of the transverse cross-section obtained for *P* = 500 W and *v* = 500 mm/s. Three main gray scales can be observed (deep gray, gray and light gray) on the BEI image, indicating that these three areas have different chemical compositions. The EDS line and point analyses were then conducted to find the element distributions from the foil to the substrate along the white arrow indicated, and the results are shown in Figure 9(b) and Table 2. The element distributions show that the area with a higher content of Ti is darker in the BEI image, and three areas can be roughly characterized: Ti substrate (deep gray), Ti-rich area (gray), and Zr-rich area (light gray), as indicated in the BEI image. Ti-rich areas are mainly located at the substrate side (i.e., the penetration area). For the penetration area, the content of Ti or Zr fluctuates dramatically (see Figure 9(b)). For example, the difference in Ti content between point 4 and point 5 is about 52 at. %. Due to mixing of the melted Ti substrate and the foil, the chemical composition of the foil side (e.g., point 1) apparently deviates from the original chemical composition of LM105 (compared with EDS calculated rather than nominal chemical composition), and its distribution is not uniform.

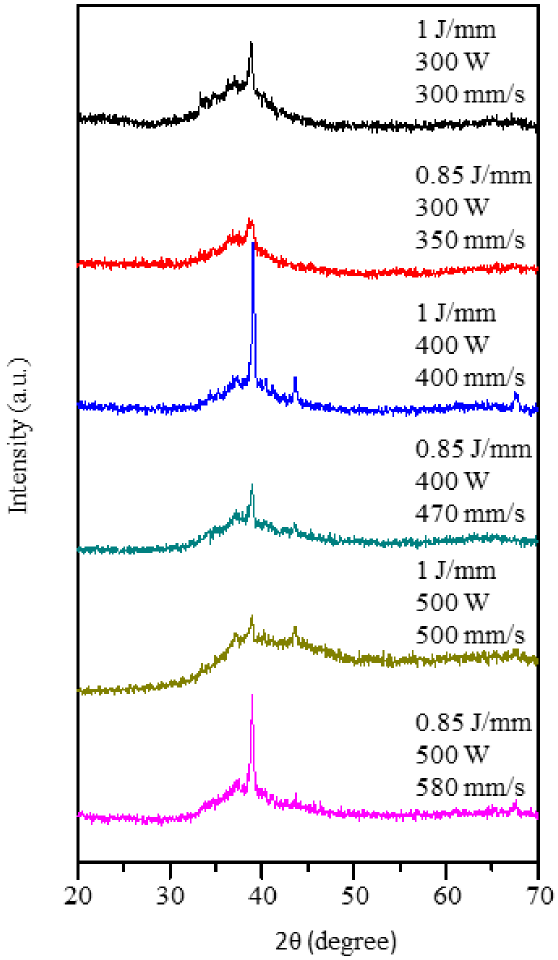

Figure 8. XRD patterns of the weld surfaces obtained when Q = 1 or 0.85 J/mm; Ti 6-4 substrates.

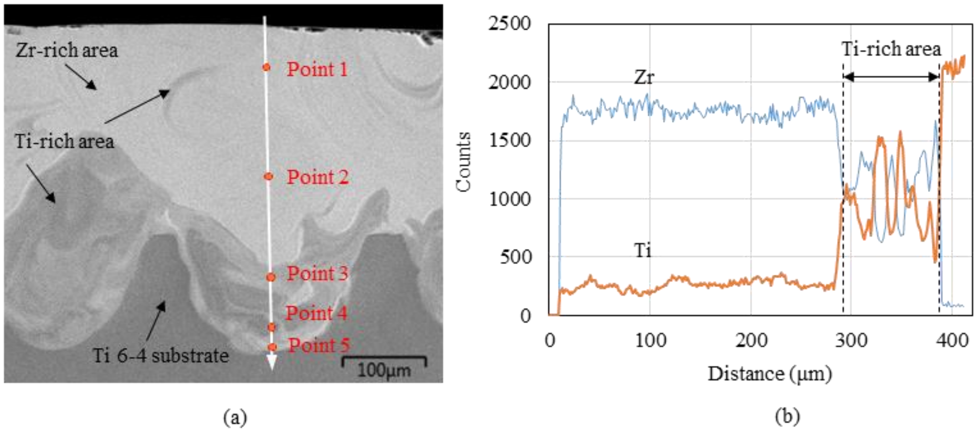

(a) (b)

Figure 9. (a) BEI image and (b) chemical composition distribution along the white arrow when *P* = 500 W, *v* = 500 mm/s; Ti 6-4 substrate.

Table 2. EDS point analysis for Figure 9 (at.%).

Element		**Zr**	**Al**	**Ni**	**Cu**	**Ti**	**V**
Original Foil	Nominal	52.5	10	14.6	17.9	5	-
	EDS calculated	48.55	9.45	14.56	21.98	5.46	-
	Point 1	44.61	9.77	13.04	20.06	12.52	-
	Point 2	43.64	9.23	13.31	20.76	13.06	-
	Point 3	22.68	10.35	6.76	11.25	47.05	1.94
	Point 4	5.83	10.56	1.73	2.72	75.92	3.23
	Point 5	39.15	9.90	10.36	16.71	23.88	-

3.2. LASER WELDING OF LM105 FOIL ONTO ZR 702 SUBSTRATE

Figure 10 shows the weld surface obtained when *Q* = 1.25, 1 or 0.85 J/mm with different *P* and *v* values. Figures 11 through 13 are the OM images of the transverse and longitudinal cross-sections obtained when *P* = 500, 400, or 300 W, respectively. Unlike Ti 6-4 substrates, crack-free joints were obtained under all these parameters; additionally, the weld surfaces were much smoother and the edge of each welding pass was much straighter. When *Q* = 1.25 or 1 J/mm, the adjacent passes were not overlapped at the interface between the foil and the substrate, but gaps were not formed, which is the same as that when using Ti 6-4 substrates, as shown in subfigures (a) and (c) for Figures 11 through 13. As lack of fusion was easy to form at a lower Q, Δd was decreased to 0.2 mm when $Q = 0.85$ J/mm, as shown in subfigure (e) for Figures 11 through 13. Compared with Ti 6-4 substrate, the swirled pattern was less pronounced when using Zr 702 substrate. In addition, when Q was constant, δ increased slightly with P, as shown in Figures 11 through 13. The XRD patterns of the weld surfaces when $Q = 1$ or 0.85 J/mm with different P and v values are shown in Figure 14. Similarly, the amorphous foils were also partially crystallized after laser welding under the aforementioned parameters.

Figure 15 shows the transverse cross-section and the XRD pattern of the weld surface after the second layer of foil was welded to the workpiece when $P = 500$ W and $v = 500$ mm/s which were the same P and v used for the first layer. It can be seen that within the detection limit of XRD (~7%, reported by Miller (2008)), no crystalline phase was observed on the top surface (Figure 15(b)), even though partial crystallization occurred when welding the first layer onto the substrate (Figure 14), indicating that the selected laser parameters would not cause crystallization of LM105 amorphous foil. The crystallization of the first layer of amorphous foil after laser welding might be caused by other reasons, to be discussed next.

Chemical composition analysis of the cross-section was then conducted for $P = 500$ W and $v = 500$ mm/s when welding one layer or two layers of foil onto the substrate, and the results are shown in Figures 16 and 17, and Tables 3 and 4. The BEI images do not show pronounced compositional contrast for Zr 702 substrates (Figures 16(a), 17(a) and 17(b)), due to a small difference in average atomic number between Zr 702 and

LM105. Figures 16(b), 17(c) and 17(d) show the element maps of Zr corresponding to Figures 16(a), 17(a) and 17(b), respectively. On the element map of Zr, an area with higher Zr content is brighter. In general, the weld metal at the substrate side (i.e., the penetration area) has a higher Zr content than that at the foil side. In the penetration area, the Zr content is around 80 at. % (Table 3), and its distribution is relatively stable (Figure 16(d)) compared with that in Ti substrate (Figure 9(b)). Figure 16(c) shows the element distribution along the white lines with a distance of 35 µm (line 1), 65 µm (line 2) and 100 µm (line 3) to the top surface when welding one layer of foil onto the substrate. It shows that the chemical composition distribution of the first layer of foil is not uniform, and the chemical compositions in some areas apparently deviate from the original chemistry of LM105. For example, the difference in Zr content between the original foil and point 5 or point 8 is about 20 at. % (Table 3).

Figures 17(c) and 17(d) shows the element distribution along the white lines with a distance of 50 µm (line 1 and line 3) and 100 µm (line 2 and line 4) to the top surface when welding two layers of foil onto the substrate. The results of the corresponding EDS point analyses are shown in Table 4. Lines 1 through 4 are all located within the second layer of foil. It can be seen that the chemical composition distribution of the second layer is more uniform and stable no matter on the transverse or the longitudinal cross-section, and the difference in Zr content between the original foil and the tested points is only about 1~2 at. % (Table 4).

To find out whether an MG structure can be built on these Ti and Zr substrates, 10 additional layers of LM105 foil were further welded to the workpieces after finishing the first layer of dissimilar metals welding for P = 500 W, v = 500 mm/s. Crystallization of the obtained MG structures built on these two substrates was not observed within the detection limit of XRD. Figure 18 shows the cross-section of the dissimilar metals joint after further welding of 10 layers of foil. It is seen that the welded foils completely peeled off from the Ti 6-4 substrate in the penetration area, while no crack formed at the joint between the foil and the Zr 702 substrate.

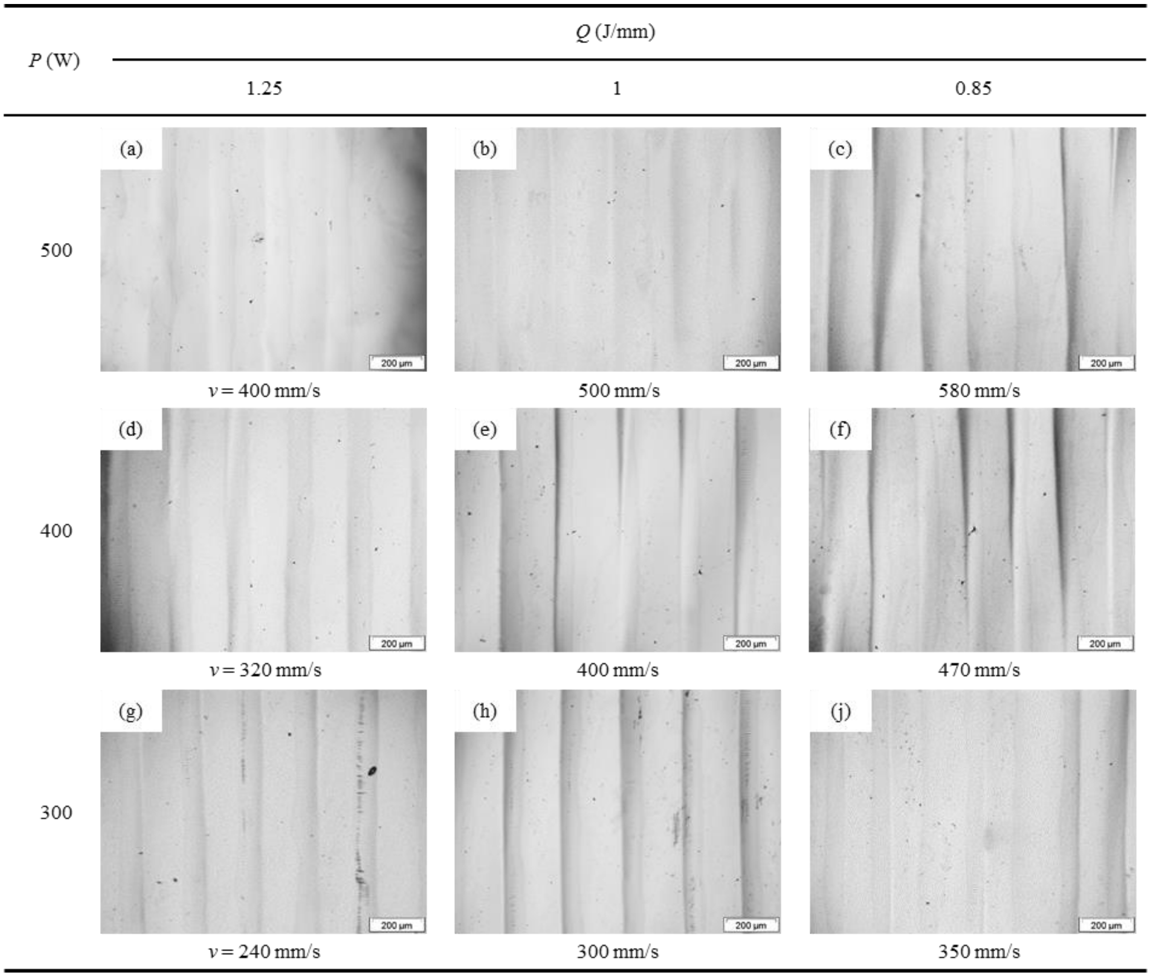

Figure 10. OM images of the weld surface obtained when Q = 1.25, 1 or 0.85 J/mm with different P and v values; Zr 702 substrates.

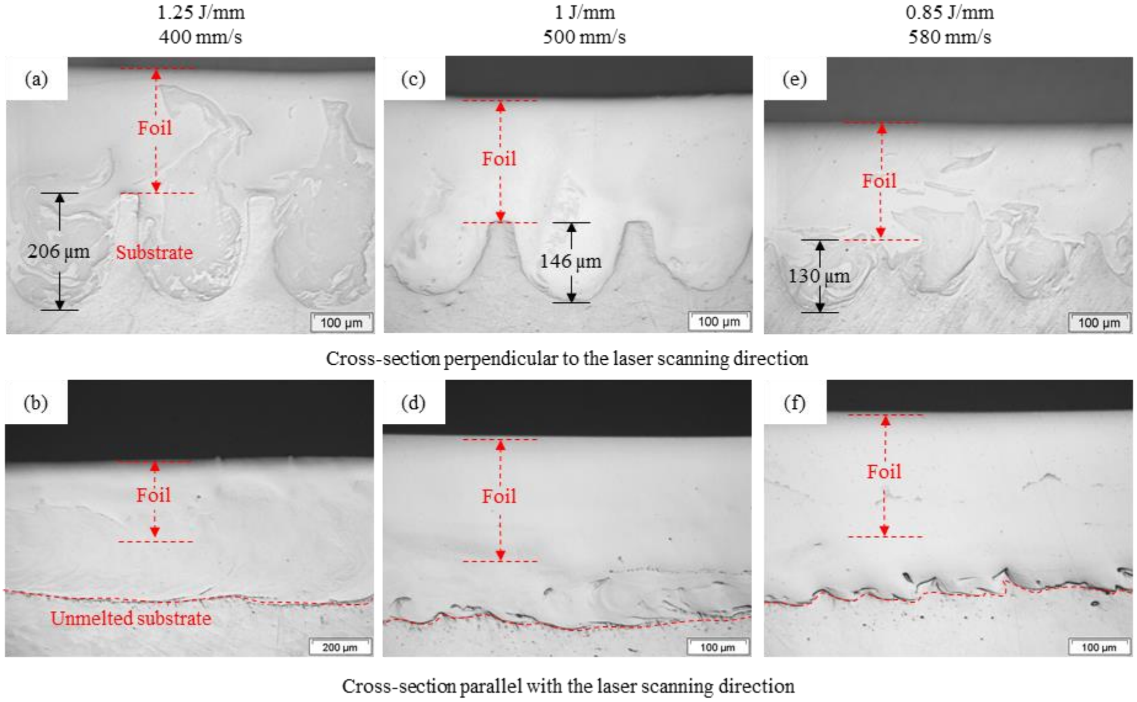

Figure 11. OM images of the cross-sections obtained when P = 500 W; Zr 702 substrates.

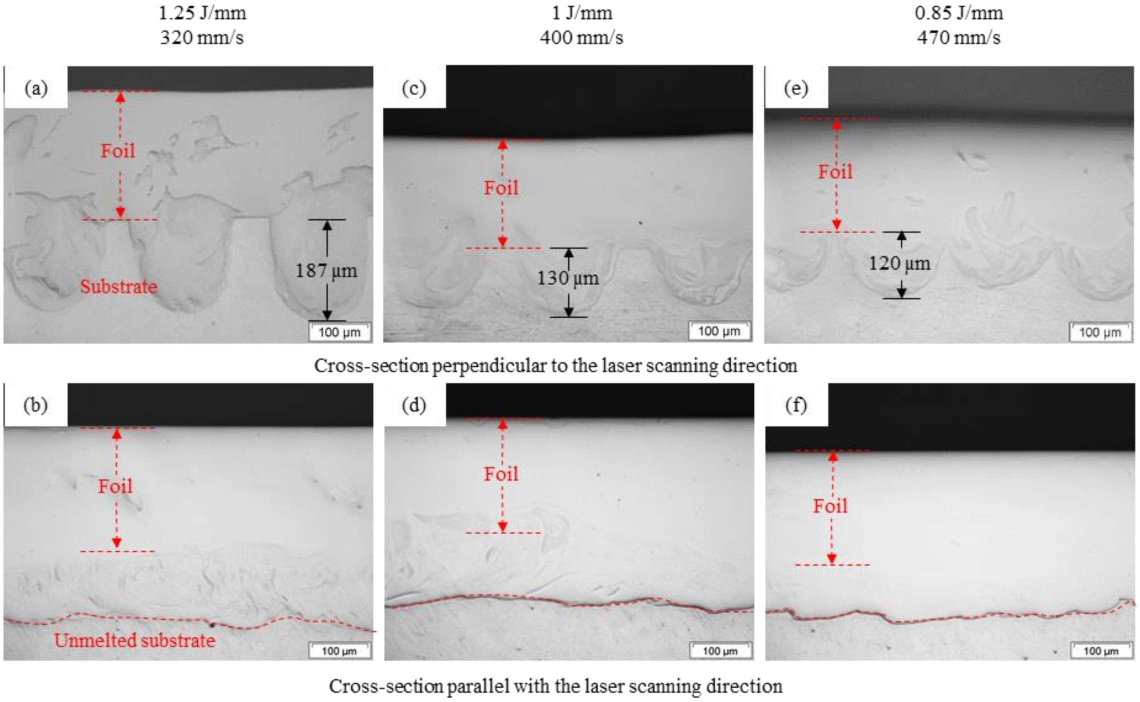

Figure 12. OM images of the cross-sections obtained when P = 400 W; Zr 702 substrates.

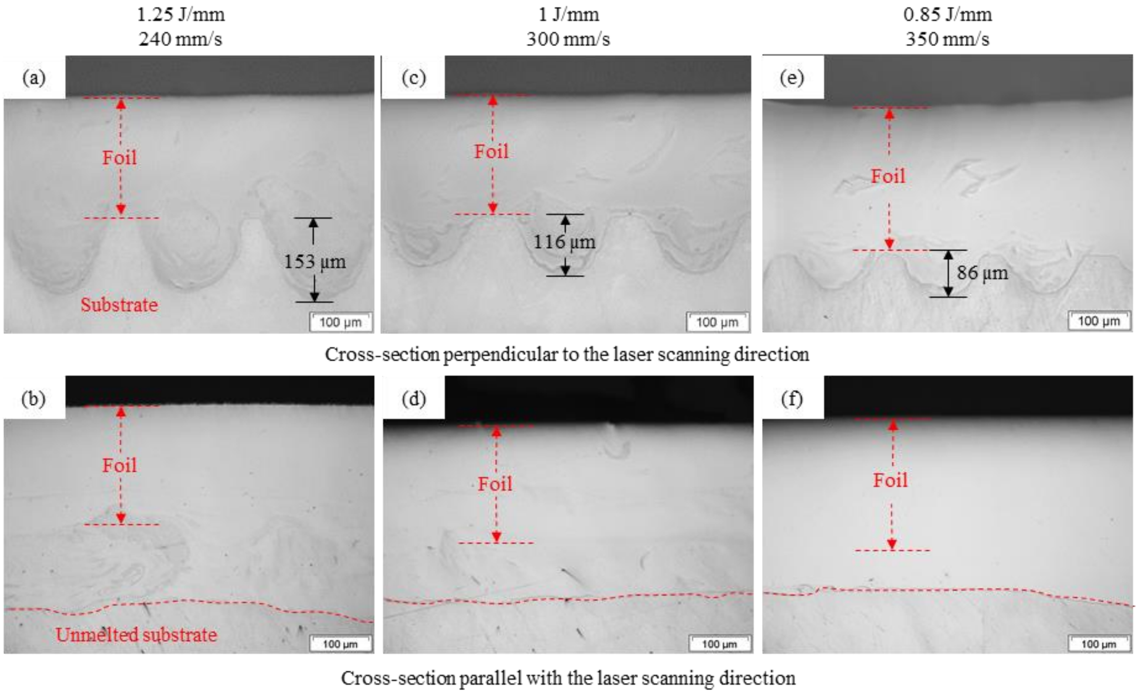

Figure 13. OM images of the cross-sections obtained when *P* = 300 W; Zr 702 substrates.

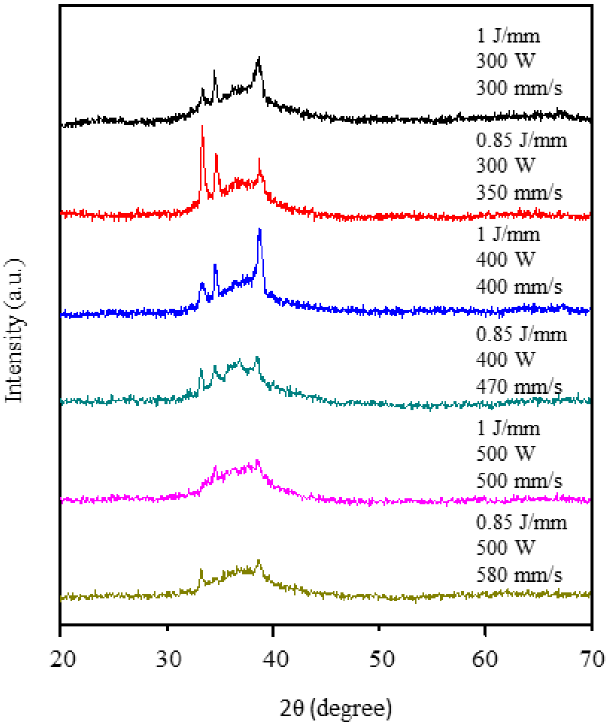

Figure 14. XRD patterns of the weld surface with different *Q*, *P*, and *v* values; Zr 702 substrates.

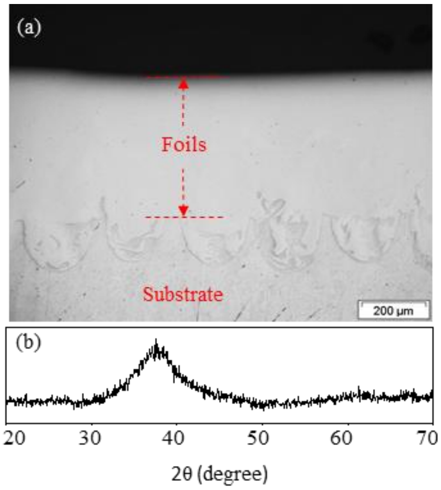

Figure 15. (a) OM image of the transverse cross-section and (b) XRD pattern of the weld surface when 2 layers of foil were welded to the substrate at *P* = 500 W and *v* = 500 mm/s; Zr 702 substrate.

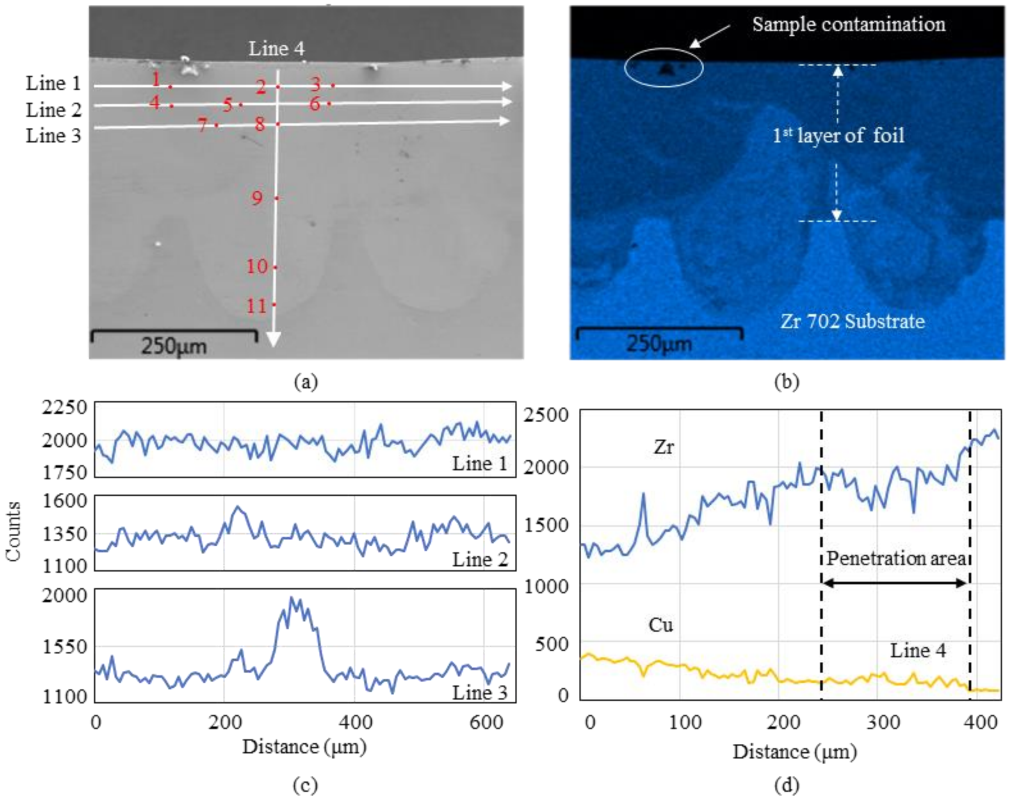

Figure 16. (a) BEI image; (b) corresponding element map of Zr; (c) Zr distribution along lines 1 through 3; (d) Zr and Cu distribution along line 4 when *P* = 500 W, *v* = 500 mm/s; Zr 702 substrate.

Table 3. EDS point analysis for Figure 16 (at.%).

Element		Zr	Cu	Ni	Al	Ti
Original foil	Nominal	52.5	17.9	14.6	10	5
	EDS calculated	48.87	22.10	14.05	9.25	5.72
	Point 1	53.00	19.99	13.12	8.66	5.24
	Point 2	49.59	21.75	14.27	9.04	5.36
	Point 3	50.80	20.69	14.53	8.77	5.21
	Point 4	51.86	20.23	14.23	8.45	5.24
	Point 5	67.52	13.32	10.34	5.50	3.32
	Point 6	51.56	19.99	14.35	8.81	5.29
	Point 7	50.29	20.71	14.99	8.84	5.18
	Point 8	70.38	12.12	8.95	5.00	3.55
	Point 9	82.23	6.98	5.64	2.88	2.27
	Point 10	76.62	9.41	7.16	4.20	2.60
	Point 11	78.74	8.93	6.13	3.55	2.66

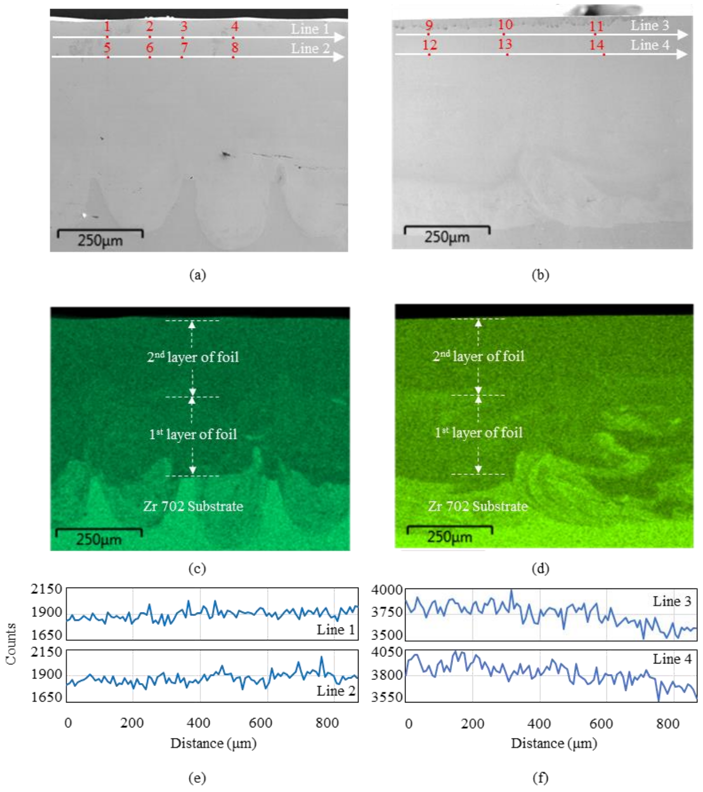

Figure 17. (a) BEI image of the transverse cross-section; (b) BEI image of the longitudinal cross-section; (c) element map of Zr corresponding to (a); (d) element map of Zr corresponding to (b); (e) and (f) Zr distribution along the white lines when *P* = 500 W, *v* = 500 mm/s; 2 layers of foil were welded onto the Zr 702 substrate.

Table 4. EDS point analysis for Figure 17 (at.%).

Element		Zr	Cu	Ni	Al	Ti
Original	Nominal	52.5	17.9	14.6	10	5
LM105	EDS calculated	48.87	22.10	14.05	9.25	5.72
	Point 1	49.39	20.89	15.49	8.79	5.44
	Point 2	49.13	20.92	15.46	9.00	5.48
	Point 3	49.40	20.94	15.14	8.86	5.66
	Point 4	48.32	21.58	15.40	9.04	5.66
	Point 5	49.25	20.22	15.54	9.42	5.58
	Point 6	49.61	20.84	14.44	9.68	5.42
	Point 7	48.79	20.47	15.82	9.21	5.71
	Point 8	48.80	20.99	14.90	9.15	6.17
	Point 9	50.12	19.70	16.01	8.62	5.55
	Point 10	50.05	19.51	15.84	8.79	5.81
	Point 11	49.69	19.26	16.63	8.67	5.75
	Point 12	50.00	19.55	16.07	9.01	5.37
	Point 13	49.98	19.55	16.20	8.69	5.57
	Point 14	49.89	19.14	16.26	8.86	5.84

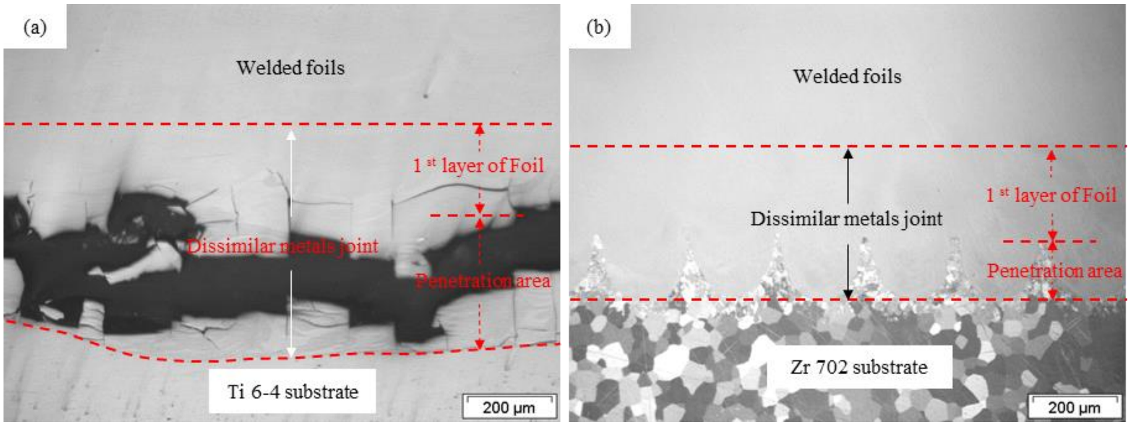

Figure 18. OM images of the cross-section of the dissimilar metals joint after further welding 10 layers of foil onto the substrate: (a) longitudinal cross-section, Ti 6-4 substrate; (b) transverse cross-section, Zr 702 substrate; *P* = 500 W, *v* = 500, *Δd* = 0.22 mm.

3.3. DISCUSSION

In LFP, considerable melting of the substrate occurs and therefore dilution (diluting the amorphous foils with the substrate) can be a major concern. Negligible dilution can be achieved in other solid-state welding processes which rely on either forge bonding or diffusion bonding. However, in laser keyhole welding, the melted substrate near the bottom of the weld pool can be entrained upward and backward by the recoil pressure (forced convection) while the laser beam is moving in one direction (Zhou et al., 2012), leading to a large-scale mixing between the molten substrate and foil. In addition, as the density of Ti 6-4 (4.43 g/cm^3) is less than that of LM105 (6.57 g/cm^3), the molten Ti 6-4 tends to float upward to the top surface (natural convection); hence, the natural convection would enhance the forced convection. On the other hand, the density of Zr 702 is 6.51 g/cm^3, which is almost the same as that of LM105 and, as a result, the effect of natural convection is trivial. However, the mixing is incomplete and is “frozen” by rapid solidification which prevents from further small-scale diffusion mixing. The aforementioned phenomena result in a “swirl” type of mixing, as shown in Figures 4 through 6, and Figures 11 through 13, and a nonuniform chemical composition distribution in the weld metals, as shown in Figure 9 and Figure 16. Because of the convective flow of molten metal, it would be difficult to achieve a low-dilution fusion bond by laser welding, particularly for laser keyhole welding. Consequently, the change of chemical composition of the weld metal would be unavoidable because of the mixing of the melted substrate and foil, and such a change of chemical composition is not uniform due to incomplete mixing.

For MGs, their high glass forming ability is contributed by the optimum chemical composition. During liquid-solid transformation, crystallization of amorphous alloy is dependent on whether the cooling rate is lower than the critical cooling rate, and a change in chemical composition from the optimum original chemistry may have a significant influence on the critical cooling rate (Kim and Kawamura, 2007). Figure 19 shows a typical schematic time-temperature-transformation (TTT) curve of the weld metal of amorphous alloy. The TTT diagram depicts the time until crystallization begins for a given temperature. The chemical composition change will result in the shift of the position (and may be the shape as well) of TTT curve on the time axis, leading to considerable increase of the critical cooling rate ($R_{c1} \rightarrow R_{c2}$). If the cooling rate is less than the new critical cooling rate (R_{c2}), crystallization will happen. In this study, partial crystallization is unavoidable when only weld one layer of amorphous foil (about 200 μm thick) onto the substrate due to the change of chemical composition in some areas. The dilution necessitates the second or more layers of amorphous foil in order to achieve fully amorphous state.

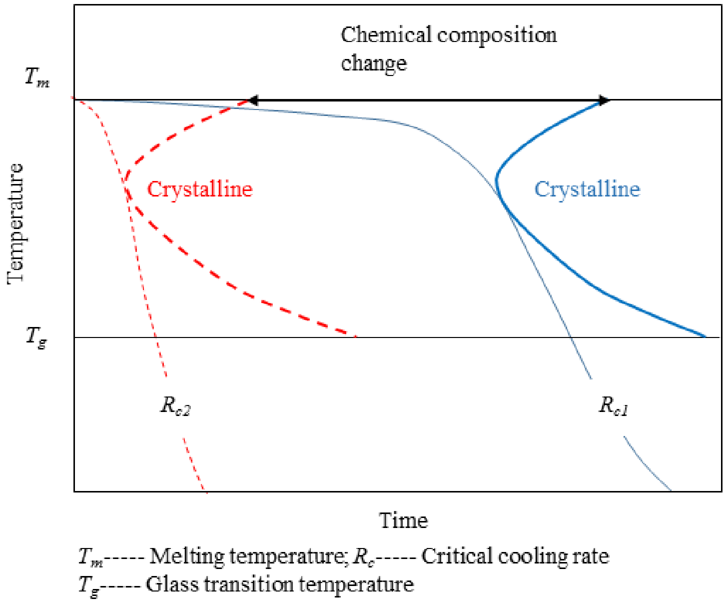

Figure 19. Schematic TTT diagram showing the effect of chemical composition change on the critical cooling rate of amorphous phase formation (adapted from Kim et al., (2006)).

The aforementioned results show that cracking occurred only when using Ti 6-4 substrates. Two factors might contribute to the susceptibility of crack formation in dissimilar metals welding: one is the differences in thermal properties between these two materials (e.g., the coefficient of thermal expansion (CTE), melting point, thermal conductivity, etc.); the other is the formation of brittle intermetallic compounds.

Table 5 shows the typical thermal properties of LM105, Ti 6-4 and Zr 702. In general, larger differences in CTE between joint materials would lead to the formation of larger residual stresses. Compared with Zr 702, the thermal properties of Ti 6-4 are closer to those of LM105. Thus, the differences in thermal properties are not the main reason for crack formation when using Ti 6-4 substrates rather than Zr 702 substrates.

Table 5. Thermal properties of LM105, Ti 6-4 and Zr 702.

Materials	**Melting temperature (°C)**	**Thermal conductivity (W/m-K)**	**Coefficient of thermal expansion (μm/m-°C）**
LM105	800	≈ 6*	12.0
Ti 6-4	1604	6.7	8.6
Zr 702	1852	22	5.8

(Data source: provided by Liquidmetal®, http://asm.matweb.com/search/SpecificMaterial.asp?bassnum=MTP641, and ATI metal. *This data is for LM1B ($Zr_{67.0}Ti_{8.8}Cu_{10.6}Ni_{9.8}Be_{3.8}$), not available for LM105.)

From the cross-section images (Figures 4 through 6 and Figure 18), we can see that the penetration area in Ti substrate is very susceptible to cracking. To examine possible formation of intermetallic phases in the penetration area, the first layer of foil was removed by mechanical grinding and the XRD patterns were obtained at the foil-substrate interface (when P = 500 W, v = 500 mm/s), as shown in Figure 20.

For the Ti 6-4 substrate, at the interface, the microstructure is a blend of amorphous phase, α-Ti and other intermetallic phases (Figure 20). Since at least six elements (Zr, Al, Ni, Cu, Ti, and V) present in the weld metal and their distribution is not uniform, and additionally the ternary and higher-order phase diagrams of these systems are usually not available, it is difficult to exactly identify all of the possible intermetallic phases that may be present and their percentages. The intermetallics could be Ti_3Al, Ni_2Zr_3, Al_3Zr_5, ZrV_2, $CuZr_2$, etc. An addition of 2-5 at. % of Ti into Zr-Cu-Ni-Al amorphous alloys can improve its glass forming ability; however, for higher Ti contents (≥ 10 at. %) and lower Cu, Ni and Al contents (Cu + Ni + Al ≤ 35 at. %), the glass forming ability decreases and, in turn, the formation of crystalline is promoted (Eckert et al., 2002). The high Ti content in the penetration area (see Figure 9(b) and Table 2) would lead to a serious crystallization. Moreover, in the penetration area, the Ti content fluctuates dramatically, larger than 50 at. %, and Ti is not always the predominant element, there are still about 24 ~ 76% of Zr, Al, Ni, Cu and V, which may increase the possibility of forming a large amount of intermetallics. Intermetallics are often hard and brittle. Fusion welds in which a large amount of brittle intermetallic phases formed often exhibit low ductility and high crack susceptibility. However, for the Zr 702 substrate, at the interface, the main phase is α-Zr, with a small amount of intermetallic compounds which could be ZrCu or Zr_6NiAl_2 (Figure 20). According to Figure 16(d) and Table 3, the Zr content in the penetration area is relatively stable and is around 80 at. %, and Cu, Ni and Al only possess about 17 at. %. Because of the low percentages, it seems that they do not considerably contribute to the brittleness of the weldment. And at the same time, the formation of ductile α-Zr phase seems to significantly improve the cracking resistance of the penetration area in Zr substrate (Kagao et al., 2004). The micro-hardness test results further support the above discussion, as shown in Figure 21. It shows that the micro-hardness of the penetration area in Ti substrate, which can reach to 880 HV, is much higher than that in Zr substrate (around 450 HV) and the original LM105 amorphous foil (563 HV). Note the test results shown in Figure 21 for unmelted Ti 6-4 and Zr 702 substrates are consistent with published data (about 340 HV for Ti 6-4 and about 150 HV for Zr 702).

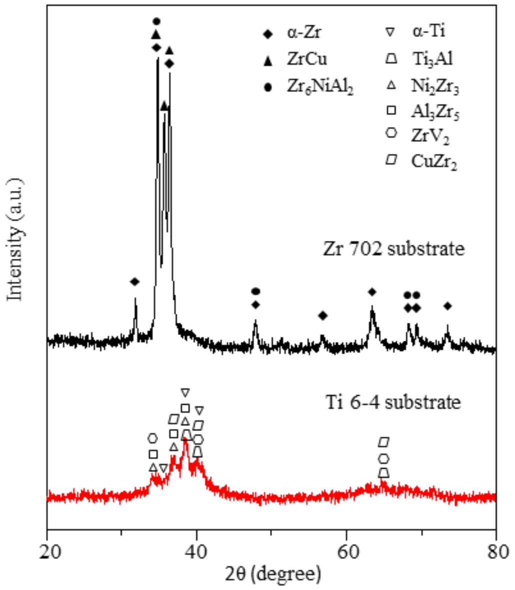

Figure 20. XRD patterns of the welding interface between the foil and the Ti 6-4 or Zr 702 substrate when *P* = 500 W, *v* = 500 mm/s.

As discussed above, welding joints between the foil and Ti 6-4 substrate have pronounced swirling structures, as compared with that between the foil and Zr 702 substrate, and such swirling structure also seems to increase the crack susceptibility of the weldment. Hence, there are three possible factors contributing to the high cracking susceptibility in the laser welding of amorphous foil onto Ti substrate: 1) the formation of a large amount of intermetallics, 2) the pronounced swirling structure, and 3) the residual stresses caused by a large difference in CTE between Ti 6-4 and LM105. Nevertheless, the exact mechanism leading to the crack formation is not yet fully understood, and apparently additional studies are still needed.

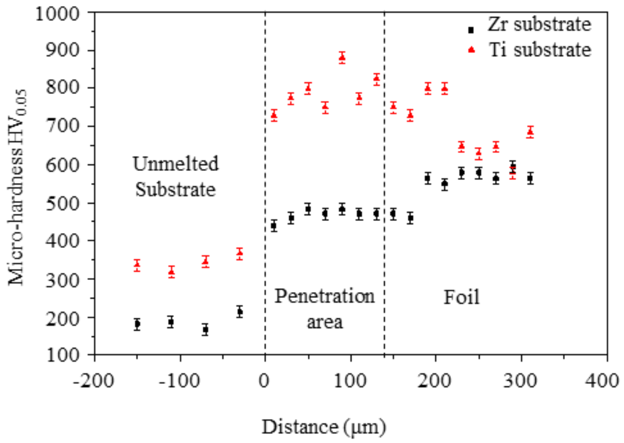

Figure 21. Micro-hardness test results of the dissimilar metals joints when P = 500 W, v = 500 mm/s.

4. CONCLUSIONS

In laser foil printing (LFP) of metallic glasses (MGs) structures, partial crystallization of the first layer of amorphous foil (about 200 μm thick for one layer) was unavoidable due to the dilution caused by the mixing of melted substrate and foil. However, fully amorphous states of the weld surface can be achieved for welding the second and additional layers of foil. For laser welding of LM105 foils onto Ti 6-4 substrates, the dissimilar metals joints have very high cracking susceptibility in the penetration area. On the contrary, for laser welding of LM105 foils onto Zr 702 substrates, cracks were not formed at all parameters tested. The formation of a large amount of intermetallics, the pronounced swirling structure, and the residual stresses caused by a difference in CTE might contribute to crack formation in the laser welding of amorphous foil onto Ti substrate. When building an MG structure on each of these two substrates, the welded amorphous foils completely peeled off from the Ti 6-4 substrate, while no cracks were observed at the dissimilar metals joint for the Zr 702 substrate. Thus, compared with Ti 6-4, Zr 702 is a suitable substrate for LM105 structures fabricated by LFP.

ACKNOWLEDGEMENTS

This work was supported by the Department of Energy (grant number DE-FE0012272); the University of Missouri System (award number FastTrack-16002R).

REFERENCES

Chen, B., Shi, T. L., Li, M., Yang, F., Yan, F., Liao, G. L., 2014. Laser welding of annealed $Zr_{55}Cu_{30}Ni_5Al_{10}$ bulk metallic glass. Intermetallics. 46, 111–117.

Chen, C., Shen, Y., Tsai, H. L., 2016. A foil-based additive manufacturing technology for metal parts. ASME J. Manuf. Sci. Eng. 139, 024501.

Eckert, J., Kühn, U., Mattern, N., He, G., Gebert, A., 2002. Structural bulk metallic glasses with different length-scale of constituent phases. Intermetallics 10, 1183–1190.

Inoue, A., 2001. Bulk amorphous and nanocrystalline alloys with high functional properties. Mater. Sci. Eng. A. 304-306, 1–10.

Kagao, S., Kawamura, Y., Ohno, Y., 2004. Electron-beam welding of Zr-based bulk metallic glasses, Mater. Sci. Eng. A. 375, 312–316.

Kawamura, Y., Shoji, T., Ohno, Y., 2003. Welding Technologies of bulk metallic glasses. J. Non-Cryst. Solids. 317, 152–157.

Kim, J., Kawamura, Y., 2007. Electron beam welding of the dissimilar Zr-based bulk metallic glass and Ti metal. Scripta Mater. 56, 709–712.

Kim, J., Kawamura, Y., 2008. Electron beam welding of Zr-based BMG/ Ni joints: Effect of beam irradiation position on mechanical and microstructure properties. J. Mater. Process. Technol. 207, 112–117.

Kim, J., Kawamura, Y., 2011. Dissimilar welding of $Zr_{41}Be_{23}Ti_{14}Cu_{12}Ni_{10}$ bulk metallic glass and stainless steel, Scripta Mater. 65, 1033–1036.

Kim, J., Lee, D., Shin, S., Lee, C., 2006. Phase evolution in $Cu_{54}Ni_6Zr_{22}Ti_{18}$ bulk metallic glass Nd:YAG laser weld. Mater. Sci. Eng. A. 434, 194–201.

Liu, Y., Hu, J., Shen, P., Guo, Z., Liu, H., 2013. Effects of fabrication parameters on interface of zirconia and Ti-6Al-4V joints using $Zr_{55}Cu_{30}Al_{10}Ni_5$ amorphous filler. J. Mater. Eng. Perform. 22, 2602–2609.

Massalski, T., Okamoto, H., Subramanian, P., Kacprzak, L., 1986. Binary alloy phase diagrams. ASM, Metals Park.

Miller, M., 2008. Microstructure. In: Miller, M., Liaw, P. (Eds.), Bulk metallic glasses. Springer, New York, pp. 122–123.

Schroers, J., 2010. Processing of bulk metallic glass. Adv. Mater. 22, 1566–1597.

Seretsky, J., Ryba, E., 1976. Laser-welding of dissimilar metals–titanium to nickel. Weld. J. 55, 208s–211s.

Shen, Y., Li, Y., Chen, C., Tsai, H. L., 2017. 3D printing of large, complex metallic glass structures. Mater. Des. 117, 213–222.

Steen, W. M., Mazumder, J., 2010. Laser Materials Processing. Springer, London.

Wang, G., Huang, Y. J., Makhanlall, D., Shen, J., 2012. Friction joining of $Ti_{40}Zr_{25}Ni_3Cu_{12}Be_{20}$ bulk metallic glass. J. Mater. Process. Technol. 212, 1850–1855.

Wang, H. S., Chen, H. G., Jang, J. S. C., Chiou, M. S., 2010. Combination of a Nd:YAG laser and a liquid cooling device to $(Zr_{53}Cu_{30}Ni_9Al_8)Si_{0.5}$ bulk metallic glass welding. Mater. Sci. Eng. A. 528, 338–341.

Wang, W. H., Dong, C., Shek, C. H., 2004. Bulk metallic glasses. Mater. Sci. Eng. R. 44, 45–89.

Wen, C., Shi, T., Chen, B., Zhu, Z., Peng, Y., Liao, G., 2015. Diffusion bonding of $Zr_{55}Cu_{30}Ni_5Al_{10}$ bulk metallic glass to Cu with Al as transition layer. Mater. Des. 83, 320–326.

Zhou, J., Tsai, H. L., Wang, P. C., 2006. Transport phenomena and keyhole dynamics in pulsed laser welding. ASME J. Heat Transfer. 128, 680–690.

Zhou, J., Tsai, H. L., Wang, P. C., 2012. Hybrid laser-arc welding in aerospace. In: Chaturvedi, M.C (Eds.), Welding and joining of aerospace materials. Woodhead Publishing, Cambridge, pp. 109–141.

II. BUILDING ZR-BASED METALLIC GLASS PART ON Ti-6AL-4V SUBSTRATE BY LASER-FOIL-PRINTING ADDITIVE MANUFACTURING

Yingqi Li, Yiyu Shen, Ming C. Leu, and Hai-Lung Tsai

Department of Mechanical and Aerospace Engineering, Missouri University of Science and Technology, Rolla, MO 65409, United States

ABSTRACT

Through using Zr intermediate layers, $Zr_{65.7}Ti_{3.3}Al_{3.7}Ni_{11.7}Cu_{15.6}$ metallic glass (MG) parts are successfully built on Ti-6Al-4V substrates by laser-foil-printing (LFP) additive manufacturing technology in which MG foils are laser welded layer-by-layer onto the substrate. The printed MG part is free of porosity, cracking and crystallization; additionally, its glass transition temperature, crystallization temperature, micro-hardness, and tensile strength are very similar to the original MG material. The Zr intermediate layers are aimed at preventing direct interaction between the first layer of MG foil and the Ti substrate; otherwise, the welded MG foils would peel off from the substrate due to the formation of hard and brittle intermetallic compounds. With the use of Zr intermediate layers, the bonding strength between the printed MG part and the Ti substrate can reach 758 MPa owing to the formation of α-Zr phase.

1. INTRODUCTION

The amorphous atomic structure and concomitant lack of grain boundaries or slip planes endow metallic glasses (MGs), i.e., amorphous alloys, with many superior properties, such as high strength, corrosion resistance, wear resistance, etc., compared with conventional crystalline metals [1−3]. However, current applications of MGs are limited by small dimensions and simple geometries (rod, foil, thin plate, etc.) because fast cooling is necessary to produce fully amorphous structures [2].

Laser-based additive manufacturing (AM) technology is a promising method to fabricate large and complex MG parts owing to the very high heating and cooling rates of laser processing. Some studies have been conducted on the fabrication of MG parts using powder-based laser AM methods, e.g., laser engineered net shaping [4,5], selective laser melting [6,7], etc. However, it is difficult for powder-based laser AM methods to fabricate dense, crack-free and fully amorphous MG parts, particularly in the heat-affected zone, since powders have voids in between and thus have poor thermal contacts. Recently, a variety of three-dimensional Zr-based MG parts without crystallization were successfully built using a newly developed laser-foil-printing (LFP) AM technology. In this technology, MG foils are laser welded layer-by-layer upon the substrates to produce MG parts [8]. Since metal foils, instead of powders, are used as feedstock, the LFP technology shows its unique advantages over powder-based AM methods on the fabrication of MG parts, such as easy to fabricate full-density parts, higher cooling rates at the same laser processing conditions, etc. The LFP technology can expand MG products to three-dimensional freeform geometries with large dimensions.

In LFP technology, a large and thick metal plate may be used as the foundation substrate upon which additional materials are gradually added layer-by-layer. Since it is difficult or even impossible to obtain large, thick as-cast MG plates, conventional crystalline metals (e.g., Ti alloys, steels) have to be used as substrates. Thus, a good bonding between the MG foil and the crystalline substrate is crucial to the success of MG parts manufactured by LFP; otherwise, the welded MG foils would peel off from the substrate before the desired part has been built because of the accumulation of residual stresses.

On the other hand, many engineering applications require structures with different properties in different locations [9]. For example, a structure may need corrosion or wear resistance in one location while needs high toughness in another location. Besides properties, cost of the structure may also need to be taken into consideration. But rarely a single material can meet all these requirements. The LFP technology provides unique opportunity for printing a structure consisting of multiple materials. Theoretically, any metal which can be laser welded is a candidate material for LFP. Resultant property changes may be obtained through welding various metal foils at different desired layers or locations during LFP to meet various application needs. MGs have excellent corrosion resistance and wear resistance, but their fracture toughness are usually insufficient [10]. In addition, to date many commercially available MGs are made from expensive metals with high-purity, e.g., high-purity Zr, resulting in very costly MGs. These factors also limit MG’s application. In many applications, there is no need to fabricate an entire MG structure; instead, most portions of the structure may be printed using cost-competitive conventional metals with favorable toughness, and only components that need to serve in extreme environment (e.g., corrosive, wear) are printed with MG. Hence, the ability to print MG parts on conventional crystalline metals, e.g., Ti alloys, stainless steels, etc., would either extend the engineering application of MGs or provide additional functions to the crystalline metal structures.

Laser welding of MGs to crystalline metals is therefore required, but is very challenging due to the large differences in physical and chemical properties which may be present between them. One of the challenges when welding MGs to crystalline metals is the formation of detrimental intermetallic phases, which would significantly deteriorate the mechanical properties of the joint. To obtain high glass forming ability, MGs usually consist of more than three elements, e.g., $Zr_{65.7}Ti_{3.3}Al_{3.7}Ni_{11.7}Cu_{15.6}$. When welding such MGs to dissimilar crystalline metals, various detrimental intermetallic phases would form due to the crystallization of MGs caused by mixing of dissimilar materials, lack of solubility, and atomic structure mismatch between different elements, etc. Laser welding of MG to the same MG has been studied in butt-joint or bead-on-plate form [11−14]. However, to the best of our knowledge, there is only one published study on laser welding of MGs to crystalline metals, which was conducted by our group [19]. In that study, we attempted to directly build Zr-based MG parts on Ti-6Al-4V (Ti64) substrates or Zr substrates. The results showed that the MG parts were successfully built on Zr substrates due to the formation of α-Zr phase, but peeled off from the Ti64 substrates due to the formation of hard and brittle intermetallics. Several studies on the welding of MGs to crystalline metals using electron beam welding can be found in the literature. Kagao et al. attempted electron beam welding of a Zr-based MG plate to a Ti alloy or Zr alloy plate, but only MG/Zr bonding succeeded due to the formation of α-Zr while the welded

MG/Ti plate had a very brittle interface due to the formation of intermetallics [15]. By minimizing the melting of crystalline plates through adjusting the beam irradiation position or the joint geometry, Kim et al. successfully welded a Zr-based MG plate to a Ti plate [16], a Ni plate [17], or a stainless steel plate [18] using electron beam welding without the formation of intermetallics. However, for LFP technology, in which multi-pass welding and lap-joint have to be used, the considerable melting of underlying crystalline substrate is unavoidable. Thus, minimizing the melting of crystalline substrate is not a feasible way for LFP to avoid the formation of detrimental intermetallics.

In this study, $Zr_{65.7}Ti_{3.3}Al_{3.7}Ni_{11.7}Cu_{15.6}$ MG parts were built on Ti64 substrates using LFP technology. Ti64 alloy was chosen because it is widely used in engineering applications (e.g., aerospace, automotive, marine, etc.) and is also less expensive than Zr metals. A feasible way to reduce the brittleness of the dissimilar bonding is to use an intermediate layer to separate the two dissimilar materials. The intermediate layer should be highly soluble with both materials. Zr has similar chemical properties to Ti, and Ti−Zr system can form h.c.p. solid solutions over the complete composition range [20]. On the other hand, Zr is the main element of the selected MG, and the previous study shows that Zr-based MG parts can be built on Zr substrates by LFP without peeling off due to the formation of α-Zr phase [19]. Thus, pure Zr foil was chosen as the intermediate layer to improve the bonding between Zr-based MG part and Ti64 substrate in this study. The properties of the printed MG part will be discussed first, and then this paper will focus on the study of the dissimilar bonding between the MG part and the Ti64 substrate.

2. EXPERIMENTAL

Since this paper focuses on the bonding between Ti64 alloy and MG, Ti64 plates, instead of 3D printed Ti64 parts, were used as the substrates in this experiment to shorten the fabrication time. The thickness of a layer of MG foil with nominal chemical composition of $Zr_{65.7}Ti_{3.3}Al_{3.7}Ni_{11.7}Cu_{15.6}$ (wt.%) (Liquidmetal®, LM105) was approximately 200 µm. 200-µm-thick pure Zr foil (Zr702) was used as the intermediate layer. Before laser processing, the substrate and foils were slightly grinded using abrasive papers to remove surface oxides, and then cleaned using ethanol.

The LFP system used in this experiment is shown in Figure 1. More details for the LFP system and procedure can be found in Ref. [8], and a short introduction is given below. This system has two lasers: a continuous wave fiber laser with 1070 nm wavelength for foil-welding and a pulsed UV laser with 355 nm wavelength and 30 ns pulse duration for foil-cutting. In this study, the welding laser beam entered a scanner and then was focused on the foil surface. The beam diameter (D) at the focus was about 170 µm. The substrate was mounted on a three-axis motion stage. A layer of foil was placed and fixed on the substrate via laser spot welding. Then, the scanner scanned multi-passes to weld the foil onto the substrate. After the welding process was done, the motion stage moved the workpiece to the location under the UV laser and the foil was cut by the UV laser along the contour of the welded region to remove the excessive foil. Another layer of fresh foil was placed on the top of the workpiece for the process of next layer. The above processes were repeated until the desired part was built. All samples were processed inside a chamber with Ar shielding gas.

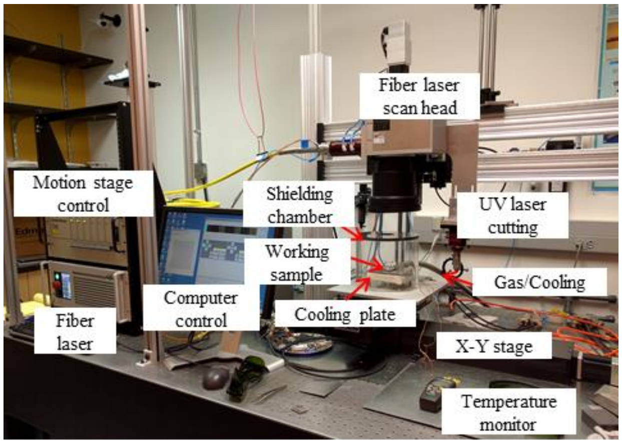

Figure 1. The LFP system developed at Missouri S&T. Reprinted from Ref. [8].

Three cases were compared in this experiment, i.e., without any intermediate layer (Case 1), with one Zr intermediate layer (Case 2), and with two Zr intermediate layers (Case 3). For Case 2, the first layer was Zr foil. For Case 3, the first and second layers were both Zr foils. After that, MG foils were welded layer-by-layer onto the workpieces to construct MG parts (see Figure 2). Theoretically, any dimension can be printed through welding different layers of MG foil and adjusting the laser scanning area. To reduce heat accumulation, the time lapse between two adjacent scan passes was 10 s. The used laser power (P), laser scanning speed (v) and hatch space (Δd) for each layer of welding are listed in Table 1. The P and v values were selected after a parametric study to ensure continuous and stable welding passes and small penetration depth at the same time. In this paper, the depth of penetration (δ) is the distance that fusion extends into the substrate or the previous layer from the original surface of the substrate or the previous layer, as schematically shown in Figure 2(b). In order to conveniently determine the position of the original surface for measuring δ, the laser cutting area was slightly larger than the laser welding area, as shown in Figure 2(b).

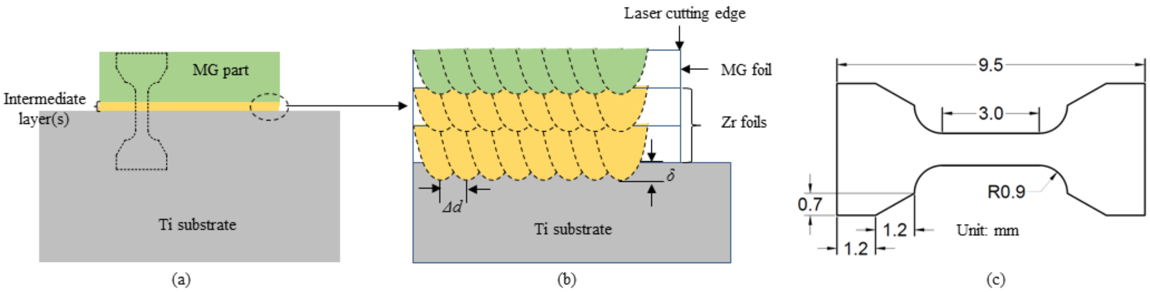

Figure 2. (a) Schematic of a MG part built on a Ti substrate with intermediate layer(s); (b) schematic of the MG–Ti bonding with two Zr intermediate layers; (c) dimensions of the miniature tensile test specimen. Δd is the hatch space, and δ indicates the penetration.

Table 1. Parameters for each layer of welding.

Layer	**Laser power (P) (W)**	**Laser scanning speed (v) (mm/s)**	**Hatch space (Δd) (mm)**
1st layer of Zr foil (if any)	500	500	0.12
2nd layer of Zr foil (if any)	500	450	0.12
1st layer of MG foil	500	570	0.12
2nd–nth layer of MG foil	500	650	0.14

To test the bonding strength between the MG part and the Ti substrate, miniature tensile test specimens were cut from a 5-mm-thick MG part printed on a 12-mm-thick Ti substrate by wire electric discharge machining (EDM), as schematically shown in Figure 2(a). The dimensions of the miniature tensile test specimens are shown in Figure 2(c), with the thickness of 1 mm. The tensile test was conducted on an INSTRON testing machine with a clip-on extensometer. The speed of the machine crosshead was maintained to be 0.015 mm/mm/min throughout the test. The extensometer was set to be removed when the specimen yielded (0.2% offset). The overstrain protection limit for the extensometer was set to be 1%. After removing the extensometer, the specimen was pulled to fracture and the strain was measured by the machine crosshead. Five specimens were tested, and the mean value was reported. The tensile strength of the printed MG part along the laser scanning direction was also tested using the same method. The microstructure, chemical composition, and fracture surfaces after tensile testing were analyzed using X-ray diffraction (XRD, Philips X'pert MPD), optical microscope (OM, Nikon Epiphot 200), and scanning electron microscope (SEM, Helios Nano Lab 600) equipped with energy dispersive spectroscopy (EDS, Oxford). The used EDS has a silicon drift detector (Oxford X-Max). The accelerating voltage, emission current, and working distance for EDS analysis were 15 kV, 1.4 nA and 5 mm respectively. The spectra were collected and analyzed in an EDS microanalysis software (Oxford, AZtec Version 3.3). Factory standardizations were used for the calculation of quantitative results. All elements identified and confirmed in qualitative analysis were quantified. The quantitative results were normalized and reported with three standard deviations based on counting statistics. The metallographic specimens for OM, SEM and EDS analysis were prepared following the general procedure of metallurgical sample preparation. Micro-hardness was measured using a Vickers micro-hardness tester (Struers, Duramin 5) with 50 g load and 10 s load duration. The reported micro-hardness value was an average of seven measurements with one standard deviation. A differential scanning calorimeter (DSC 2010, TA Instruments) was used to measure the glass transition temperature and crystallization temperature of the MG part.

3. RESULTS AND DISCUSSION

3.1. THE PRINTED MG PART

Figure 3(a) shows a 3.5×15×65 mm^3 MG part printed on a 6-mm-thick Ti substrate with two Zr intermediate layers. Note the striation on the Ti substrate was caused by machining, not by LFP. This MG part was cut off from the substrate to do analysis. Figure 3(b) shows the OM image of the transverse (perpendicular to the laser scanning direction) cross-section of the MG part. This cross-section was etched using a solution of 100 ml H_2O, 2 ml H_2O_2 and 0.1 ml HF which can reveal the crystallization of LM105 MG occurred during laser scanning [8]. The cross-section is featureless; no pore, cracking and crystallization are observed. The XRD result of the MG part, which was conducted on the longitudinal (parallel with the laser scanning direction) cross-section of the middle plane, also confirms that the MG part is fully amorphous within the detection limit of XRD (~ 7% [21]) (see Figure 3(c)). DSC was used to compare the glass transition temperature (T_g) and the crystallization temperature (T_x) of the built MG part with those of the original MG at a heating rate of 20 °C/min, and the results are shown in Figure 3(d). For the MG part, $T_g \approx 397$ °C, $T_{x1} \approx 475$ °C and $T_{x2} \approx 482$ °C. These values are very close to those of the original MG, in which $T_g \approx 394$ °C, $T_{x1} \approx 470$ °C and $T_{x2} \approx 478$ °C. Micro-hardness and tensile tests were conducted to investigate the mechanical properties of the MG part. For comparison, the tensile strength of the original MG with a thickness of 750 μm was also tested. The micro-hardness of the MG part is 528 ± 17 HV, which is close to that of the original MG foil (560 ± 18 HV). The original MG has an ultimate tensile strength (UTS) of 1533 ± 52 MPa, while the MG part exhibits higher

UTS (1758 ± 17 MPa), as shown in Figure 3(e). The above observations show that the printed MG part is extremely similar to the original MG material.

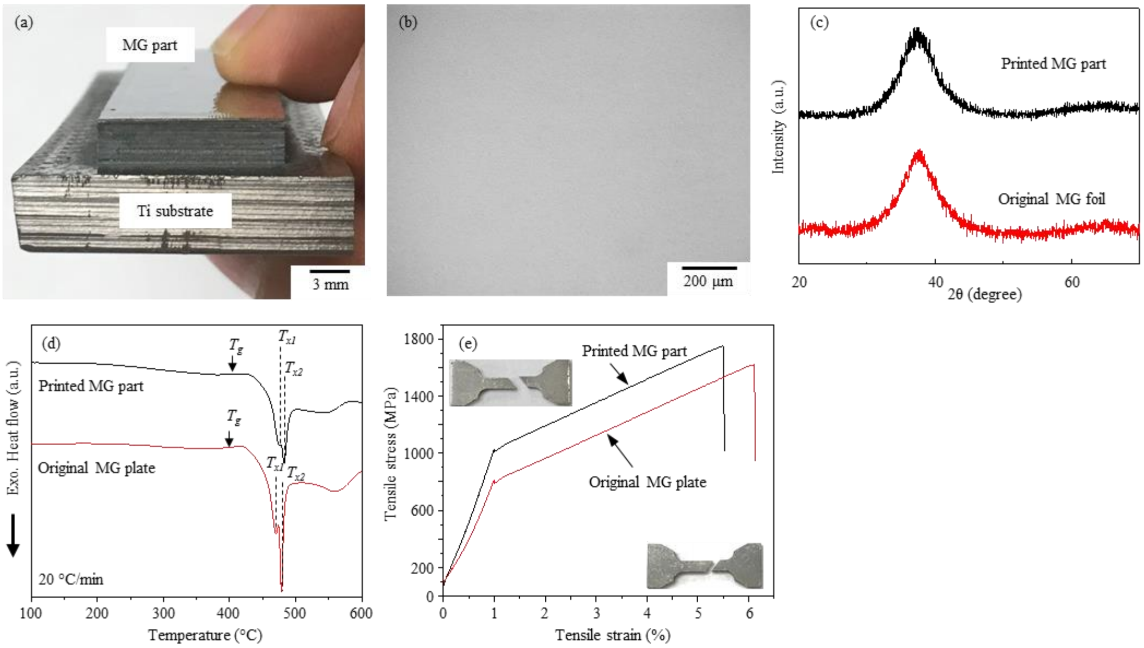

Figure 3. The printed MG part: (a) a 3.5×15×65 mm^3 MG part built upon a Ti substrate with two Zr intermediate layers; (b) OM image of the transverse cross-section; (c) XRD pattern; (d) DSC profile; (e) tensile stress-strain curve. For comparison, the data for the original MG are also included.

3.2. THE BONDING BETWEEN THE MG PART AND THE Ti SUBSTRATE

Figure 4 shows the bonding between the MG part and the Ti substrate without intermediate layer (Figure 4(a)), with one Zr intermediate layer (Figure 4 (b)), or with two Zr intermediate layers (Figure 4 (c)). When a MG part was directly built on a Ti substrate, the welded MG foils completely peeled off from the substrate after 10 layers of MG foil were welded, indicating a weak bonding between the MG and the Ti, as shown in Figure 4(a). When one intermediate layer was used, even though the MG part did not peel off from the substrate during part fabrication, the sample fractured at the interface between the MG and the Zr layer during cutting tensile test specimens by EDM, as shown in Figure 4(b). On the contrary, when two intermediate layers were used, the sample did not fracture after part fabrication and EDM cutting (see Figure 4(c)).

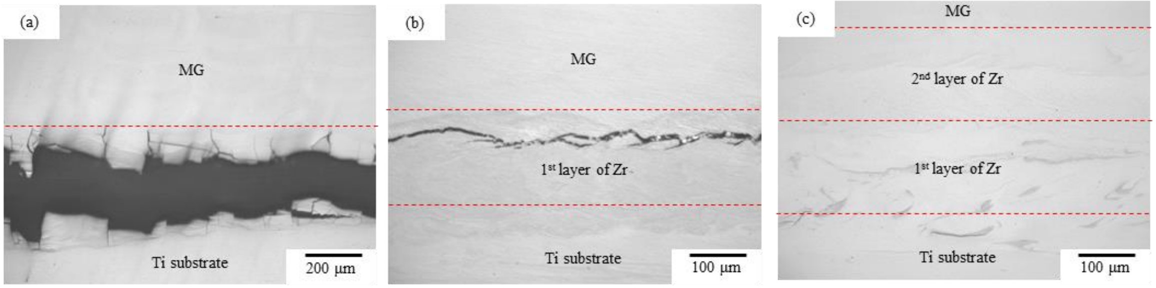

Figure 4. OM images of the longitudinal cross-section of the bonding between the MG part and the Ti substrate: (a) without intermediate layer; (b) with one Zr intermediate layer; (c) with two Zr intermediate layers.

The chemical composition, microstructure and properties were then analyzed and compared on the bonding between the first layer of MG foil and the Ti substrate for these three cases. A layer of MG foil was first directly welded onto the Ti substrate without any intermediate layer at P = 500 W, v = 580 mm/s, Δd = 0.25 mm. Figure 5(a) is the backscattered electron image of the transverse cross-section of the bonding. It can be seen that the welding is a keyhole-mode, instead of conduction-mode, which is consistent with the calculated laser intensity $I = P/(\pi D^2/4) = 2.2\times10^6$ W/cm^2. The depth of penetration (δ) is about 95 µm. In addition, the transverse cross-section shows a swirling structure, especially at the bottom of the welding metal, i.e., the penetration area or the MG−Ti interface. Note the interface refers to the penetration area in this paper. This swirling structure indicates the incomplete mixing between the melted Ti substrate and the MG foil due to rapid solidification in laser welding. Figure 5(b) shows the longitudinal cross-section of the bonding area, from which cracking can be easily observed at the MG−Ti interface. The micro-hardness profile of the bonding is shown in Figure 5(c). It can be seen that the micro-hardness of the MG−Ti interface (indicated by δ) can reach ~ 800 HV, and is much higher than that of the unmelted Ti substrate (~ 340 HV), the MG foil side (~ 640 HV) or the original MG foil (~ 560 HV).

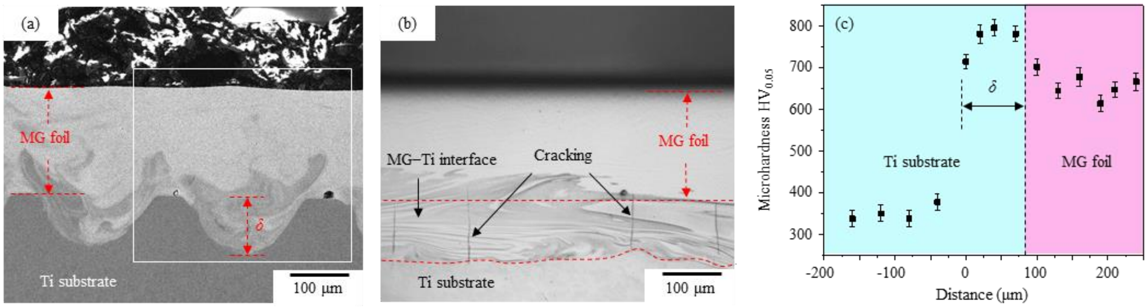

Figure 5. The MG–Ti bonding without intermediate layer: (a) backscattered electron image of the transverse cross-section; (b) OM image of the longitudinal cross-section; (c) micro-hardness profile.

Figure 6 shows the distribution of the constituent elements in the MG−Ti bonding corresponding to the rectanglular area in Figure 5(a). Along the white arrow in Figure 6(a), a series of points were measured for composition in weight percent, and all the EDS point data were plotted in Figure 7. EDS was also used to measure the chemical composition of the Ti64 substrate (Ti: 89.8 ± 1.0 wt.%, Al: 6.2 ± 0.8 wt.%, V: 4.0 ± 0.9 wt.%) and the original MG foil (Zr: 61.5 ± 1.2 wt.%, Ti: 3.6 ± 0.6 wt. %, Al: 3.5 ± 0.4 wt.%, Ni: 12.2 ± 0.9 wt.%, Cu: 19.3 ± 1.1 wt.%). The above reported compositions for the Ti64 substrate and the original MG foil were the mean values of five spectra with three standard deviations. It can be seen that the MG−Ti interface, which has highest cracking susceptibiliy, is a Ti−rich area that has higher Ti content and less Zr than the

MG foil (see Figures 6(a), 6(b) and 7). In addition, the distribution of Ti is not uniform at the MG−Ti interface (see Figures 6(h) and 7), which is consistent with the swirling structure shown in Figure 5(a). An addition of 2−5 at.% of Ti can improve the glass forming ability of Zr-Cu-Ni-Al amorphous alloys; however, for higher Ti content (≥ 10 at.%) and lower contents of Cu, Ni and Al ($Cu + Ni + Al \leq 35$ at.%), the glass forming ability decreases and, in turn, the formation of crystalline is promoted [22]. In most area of the MG–Ti interface, the Ti content is larger than 41 wt.% (i.e., 50 at.%), and Cu + Ni + Al ⩽ 22 wt.% (i.e., 26 at.%) (see Figure 7). Thus, the formation of crystalline phases is promoted. There are at least six elements (Zr, Ti, Al, Ni, Cu, and V) existing at the MG−Ti interface, and these elements are not all mutually soluble [23], which would increase the possibility of forming a large amount of intermetallic compounds.

The XRD pattern, tested at the MG−Ti interface after removing the MG by mechanical grinding, shows that the microstructure is a blend of amorphous phase and intermetallics, as shown in Figure 8. Since at least six elements are present in the weld metal and their distribution is not uniform (see Figure 6), and additionally the ternary and higher-order phase diagrams of these elements are usually not available, it is difficult to exactly identify all the possible intermetallics that may be present. Thus, only several possible intermetallics based on the binary systems, i.e., $ZrCu_2$, Ni_2Ti, Ni_2Zr_3, and Al_2Zr, are labeled in Figure 8, and there might be other binary, ternary or higher order intermetallics formed but not identified. Intermetallics are often hard and brittle, and their formation is responsible for the very high micro-hardness and cracking susceptibility at the MG−Ti interface [24]. On the other hand, the large difference in the coefficient of thermal expansion (CTE) between LM105 MG (12.0 µm/m-°C) and Ti64 (8.6 µm/m-°C) would result in large residual stresses, which might promote the formation of cracking in the area with high cracking susceptibility.

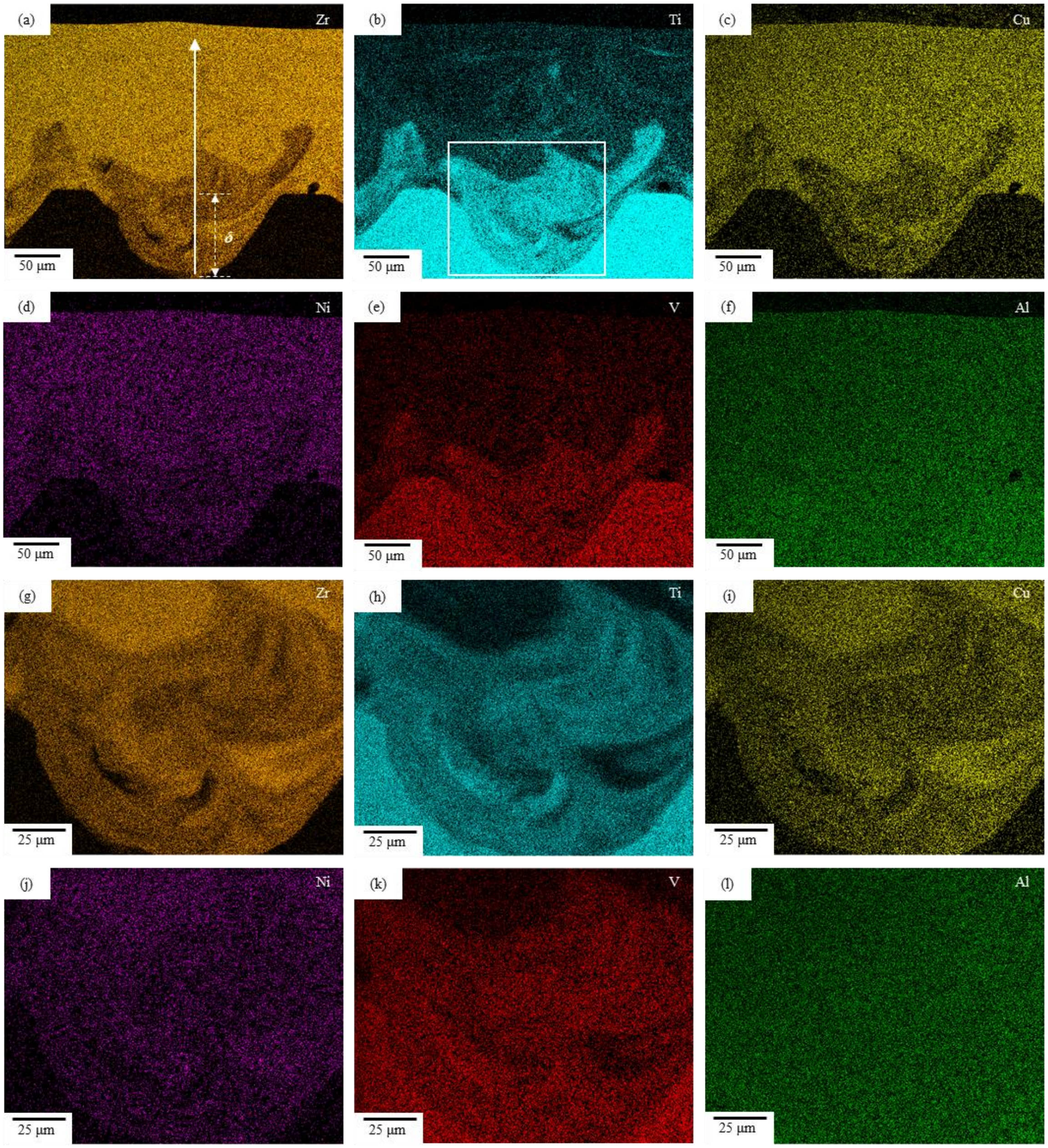

Figure 6. (a–f) EDS maps of the constituent elements for the rectangular area in Figure 5(a); (g–l) magnified elemental maps for the rectangular area in (b).

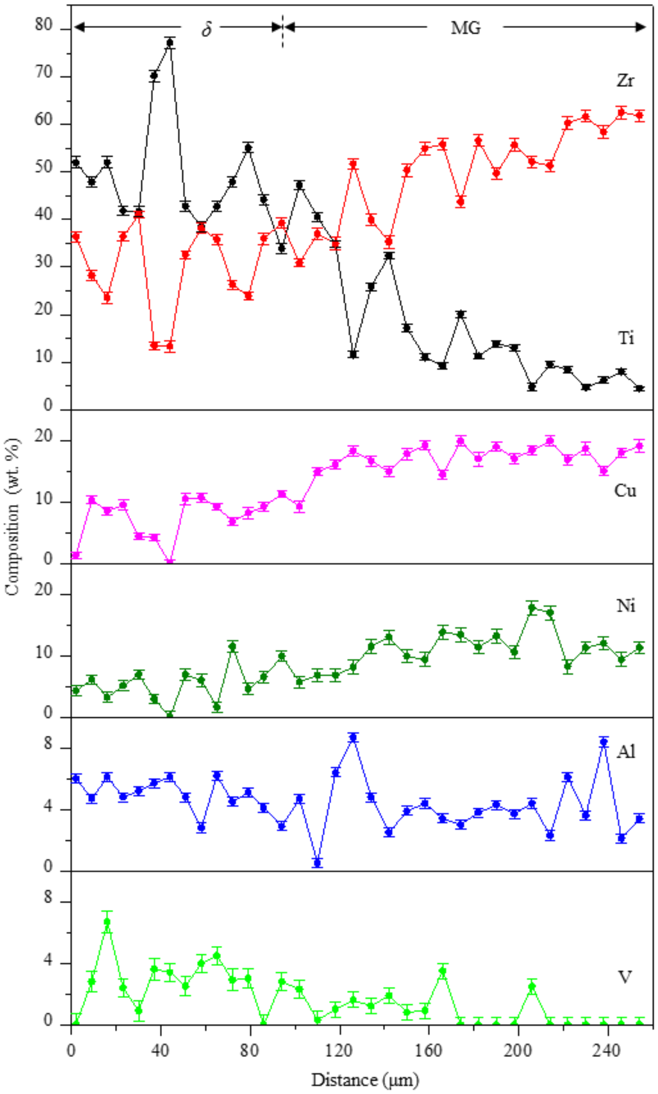

Figure 7. Chemical composition distribution along the white arrow in Figure 6(a).

Figure 9 shows the transverse and longitudinal cross-sections of the bonding area after welding the first layer of MG foil onto the Ti substrate with one Zr intermediate layer. This bonding consists of two interfaces, i.e., Zr−Ti interface and MG−Zr interface. The penetration depths for welding the Zr foil (δ_1) and for welding the MG foil (δ_2) are ~ 70 µm and ~ 60 µm, respectively, as shown in Figure 9(a). Although the MG part peeled off from the substrate during EDM cutting (see Figure 4(b)), cracking was not observed in the bonding area after welding the first layer of MG foil (Figure 9(b)). Subfigures (a) and (b) for Figure 10 are the elemental maps of Zr and Ti at the bottom of the intermediate layer. The chemical compositions of the tested points along the white arrow in Figure 10(b) are plotted in Figure 10(c). It can be seen that the mixing between the melted Ti substrate and the Zr foil is not very uniform due to rapid solidification. Generally, there is ~ 20 wt.% of Ti mixed with Zr in the intermediate layer (Figure 10(c)).

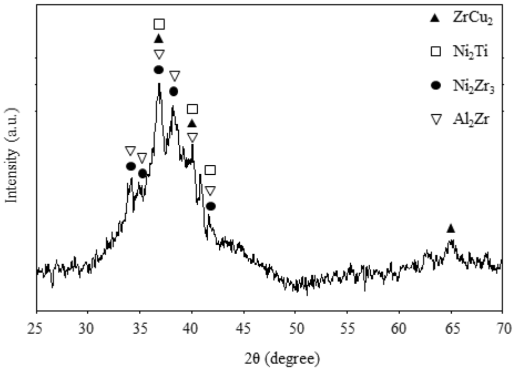

Figure 8. XRD pattern obtained at the MG–Ti interface.

Figure 11 shows the distribution of the constituent elements at the MG−Zr interface corresponding to the rectangular area in Figure 9(a). The results for the EDS point data along the white arrow in Figure 11(a) are plotted in Figure 12. Cu and Ni are the elements only coming from the MG foil, which can be used to indicate the metal flow of MG. Compared with the MG−Ti interface (see Figures 6 and 7), the MG−Zr interface has much lower Ti content and higher Zr content. For example, the MG–Ti interface shown in Figure 7 has ~ 34−77 wt.% of Ti and ~ 13−41 wt.% of Zr, but the MG−Zr interface shown in Figure 12 has ~ 5−13 wt.% of Ti and ~ 62−75 wt.% of Zr. The use of

Zr intermediate layer indeed reduced the cracking susceptibility of the MG−Ti bonding, and this improvement might be contributed by the reduced Ti content and increased Zr content at the MG−Zr interface.

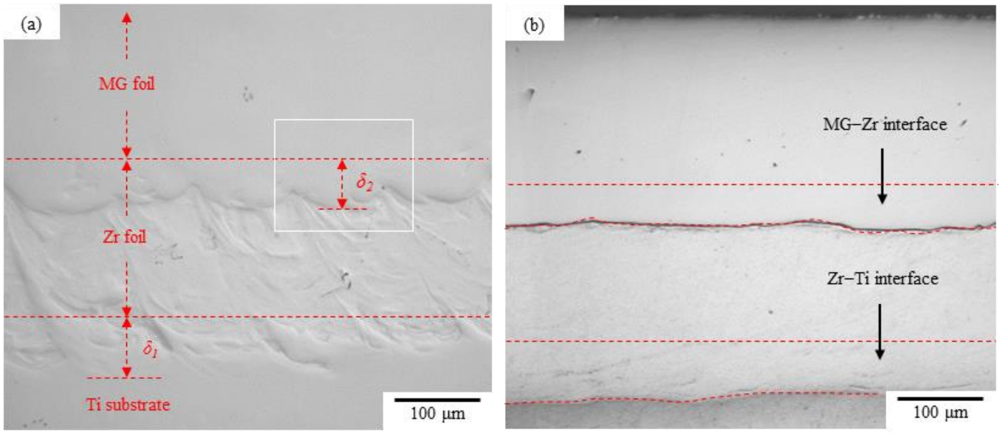

Figure 9. The MG–Ti bonding with one Zr intermediate layer: (a) OM image of the transverse cross-section; (b) OM image of the longitudinal cross-section.

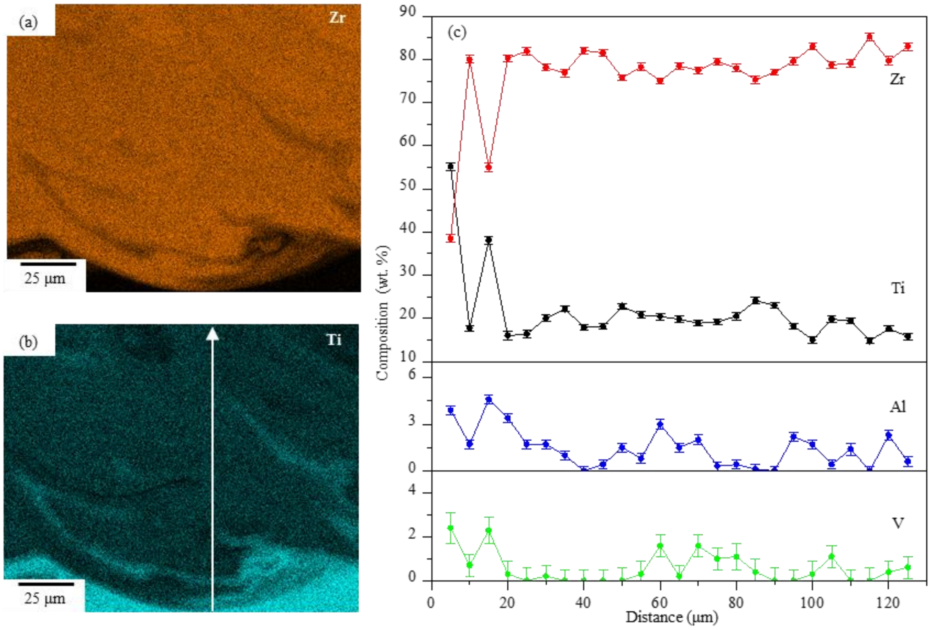

Figure 10. (a) and (b) Elemental maps of Zr and Ti at the Zr–Ti interface; (c) chemical composition distribution along the white arrow in (b).

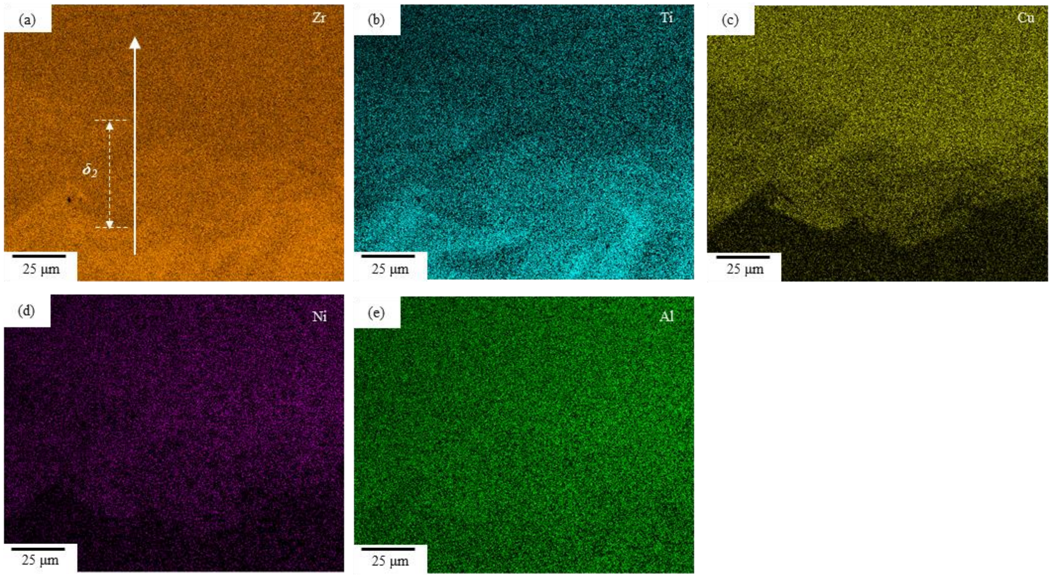

Figure 11. EDS maps of the constituent elements at the MG–Zr interface corresponding to the rectangular area in Figure 9(a).

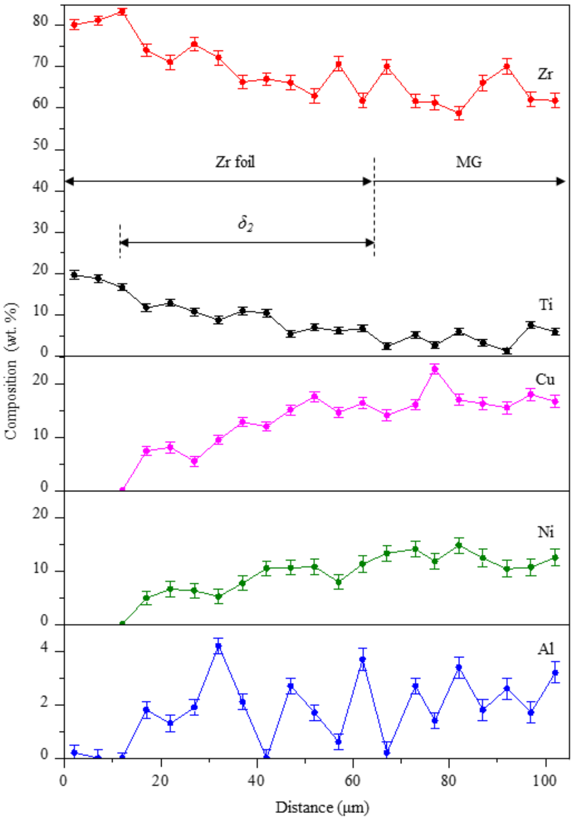

Figure 12. Chemical composition distribution along the white arrow in Figure 11(a).

XRD analysis was conducted at the MG−Zr interface after removing the MG layer and then at the Zr−Ti interface after removing the Zr layer by mechanical grinding, and the results are shown in Figure 13. For comparison, the XRD pattern of the original Zr foil is also included. The original Zr foil is composed of α-Zr phase which has a h.c.p. crystal structure. At the Zr−Ti interface, the formed phase is also α-Zr. However, the XRD pattern of the Zr−Ti interface exhibits peak shift, broadening and change in relative intensities, compared with that of the original Zr foil, which is mainly caused by solid solution effect and preferred orientation. Due to the mixing between the melted Ti substrate and the Zr foil (see Figure 10), Ti, Al and V atoms incorporated in the h.c.p. crystal structure of the pure Zr, leading to the decrease of the lattice parameters of the h.c.p. crystal structure since Ti, Al and V atoms are smaller than Zr atoms. The decrease of the lattice parameters would result in the shift of Bragg peaks to higher diffraction angles and the microstain broadening of Bragg peaks [25]. The degree of variation in the lattice parameters would increase with the solute content. Thus, the nonuniform distribution of chemical composition at the Zr−Ti interface might lead to varying lattice parameters in different locations, which would also cause the changes in the widths and shapes of the Bragg peaks. At the MG−Zr interface, the microstructure is a blend of amorphous phase and intermetallics (could be Ni_2Zr_3, AlZr, Zr_2Ni), which is similar to the MG−Ti interface (see Figure 8).

Figure 14 is the micro-hardness profile of the MG−Ti bonding with one Zr intermediate layer. Because of solid solution hardening, the micro-hardness of the Zr intermediate layer is much higher than that of the original Zr foil (~ 150 HV). Similar to the MG−Ti interface, the MG−Zr interface (indicated by δ_2) also has the highest hardness (can reach ~ 580 HV) in the dissimilar bonding, but it is much smaller than the hardness of the MG−Ti interface, which can reach ~ 800 HV (see Figure 5(c)). Because of the formation of intermetallics and the resultant higher hardness, the MG−Zr interface became the weakest region in the MG−Ti bonding when only one intermediate layer was used. There is a large difference in CTE between Zr (5.8 µm/m-°C) and MG (12.0 µm/m-°C). As the MG part was built up, the residual stresses in the dissimilar bonding accumulated. Once the residual stresses exceeded the bonding strength of the dissimilar bonding, failure occurred, as shown in Figure 4(b).

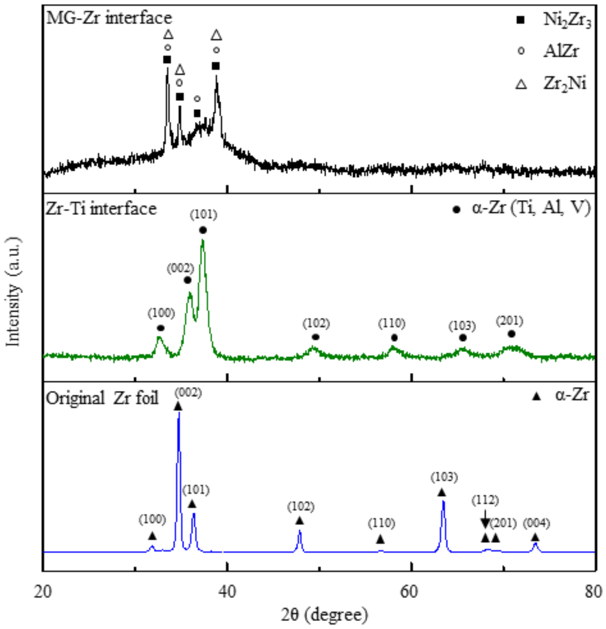

Figure 13. XRD patterns taken at the MG–Zr interface and the Zr–Ti interface, with one Zr intermediate layer.

Figure 15 shows the transverse and longitudinal cross-sections of the MG−Ti bonding with two Zr intermediate layers. The penetration depths δ_1 for welding the first layer of Zr, δ_2 for welding the second layer of Zr, and δ_3 for welding the first layer of MG are around 67 µm, 115 µm, and 84 µm, respectively, as shown in Figure 15(a). This bonding consists of three interfaces, i.e., Zr−Ti interface, Zr−Zr interface and MG−Zr interface (see Figure 15(b)). Cracking is not observed in these three interfaces from the cross-sections.

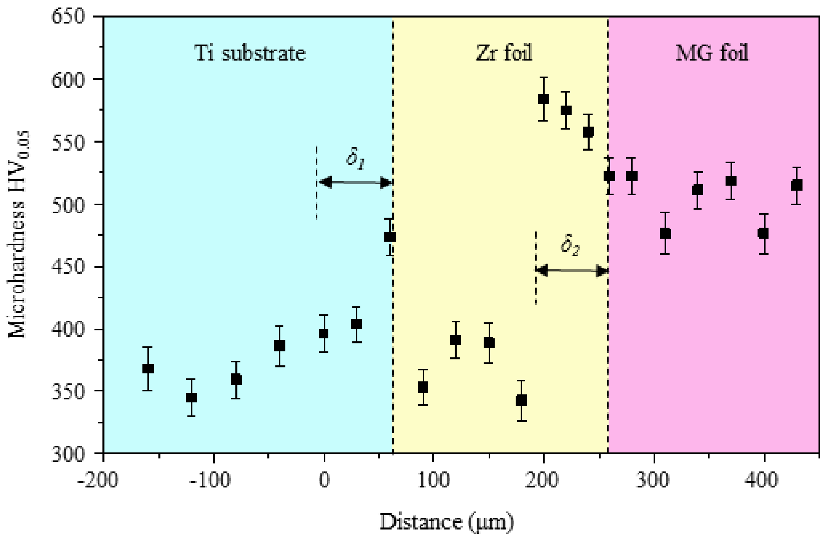

Figure 14. Micro-hardness profile of the MG–Ti bonding with one Zr intermediate layer.

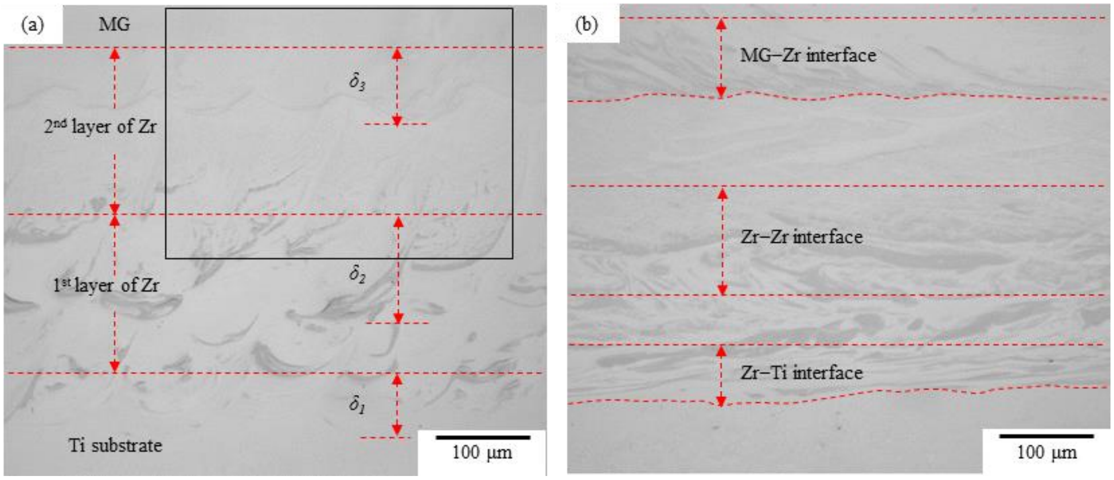

Figure 15. The MG–Ti bonding with two Zr intermediate layers: (a) OM image of the transverse cross-section; (b) OM image of the longitudinal cross-section.

Figure 16 shows the elemental maps taken at the MG−Zr interface, corresponding to the rectangular area in Figure 15(a). The chemical compositions of the tested points along the white arrow in Figure 16(a) are plotted in Figure 17. For the second layer of Zr, the distribution of chemical composition fluctuates in the area close to the first layer of Zr, and becomes relatively uniform in the area close to the MG, as shown in Figures 16 and 17. Additionally, there are ~ 6 wt.% of Ti and ~ 94 wt.% of Zr in the area with uniform chemistry distribution (see Figure 17). Compared with the case with one Zr intermediate layer (Figures 11 and 12), at the MG−Zr interface, the Ti content is further reduced, and meanwhile the increase of Zr content is considerable when two Zr intermediate layers were used (Figures 16 and 17). For example, the MG–Zr interface shown in Figure 17 have ~ 4−6 wt.% of Ti and ~ 75−87 wt.% of Zr, while the MG–Zr interface shown in Figure 12 has ~ 5−13 wt.% of Ti and ~ 62−75 wt.% of Zr.

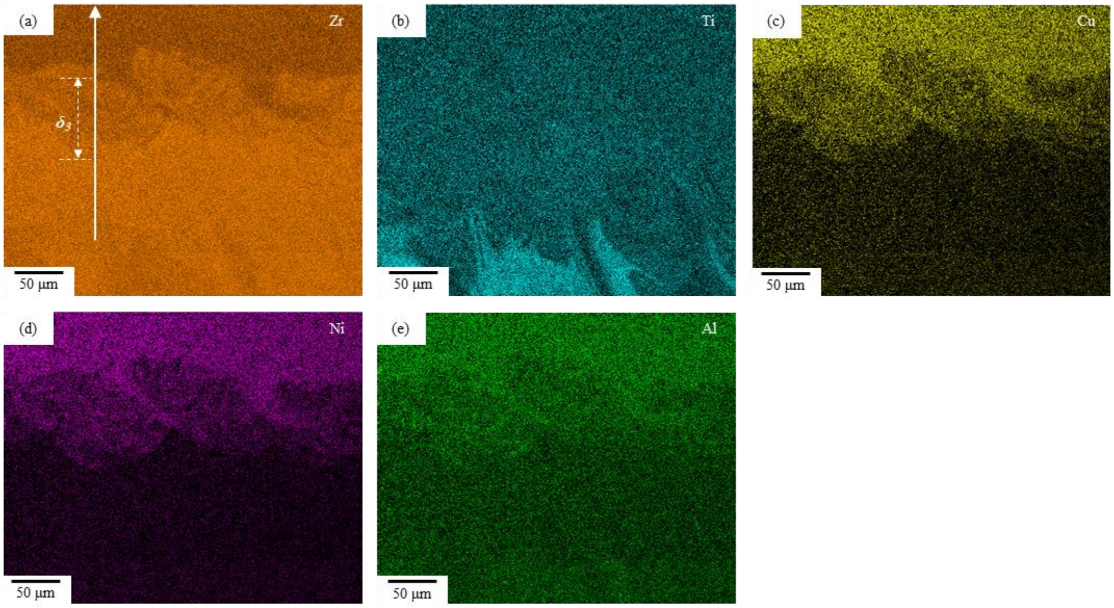

Figure 16. EDS maps of the constituent elements at the MG-Zr interface corresponding to the rectangular area in Figure 15(a).

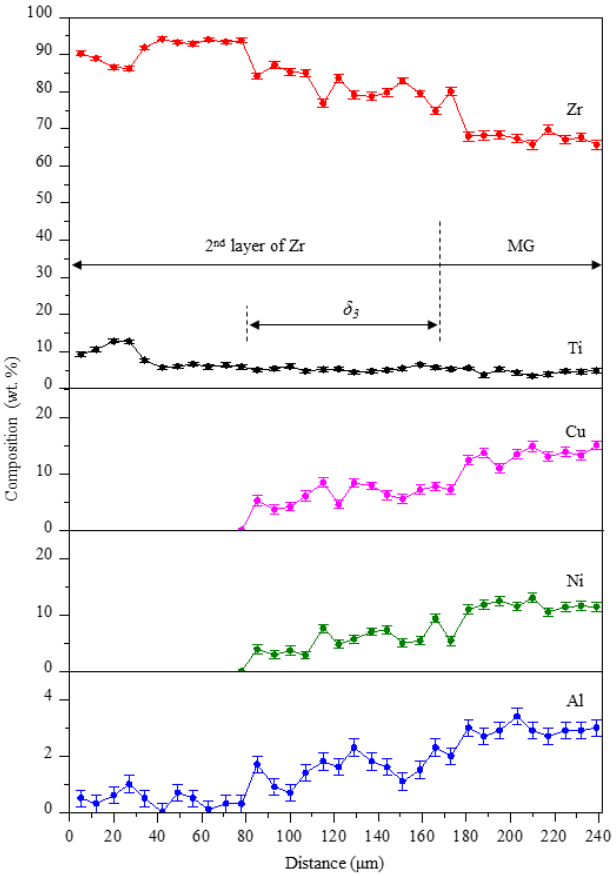

Figure 17. Chemical composition distribution along the white arrow in Figure 16(a).

Figure 18 shows the XRD patterns obtained at the MG−Zr interface after removing the MG and then at the Zr−Zr interface after removing the second layer of Zr by mechanical grinding. The Zr−Zr interface is also composed of α-Zr phase. Since the content of the solute elements (i.e., Ti, Al, or V) is much smaller at the Zr–Zr interface (see Figure 17) than the Zr–Ti interface (see Figure 10), the shift and broadening of Bragg peaks are less pronounced for the Zr–Zr interface (Figure 18). At the MG−Zr interface, because of the very high content of Zr (see Figures 16 and 17), α-Zr phase formed. In addition, amorphous phase and ZrCu intermetallic are also detected. Because of the low content of Cu at the MG−Zr interface, the formation of ZrCu would not considerably contribute to the brittleness of the weldment. Owing to the formation of soft α-Zr phase, the micro-hardness at the MG−Zr interface with two intermediate layers (~ 460 HV, Figure 19) is smaller than that at the MG−Zr interface with only one intermediate layer (~ 560 HV, Figure 14), and is significantly lower than that at the MG−Ti interface without intermediate layer (~ 760 HV, Figure 5(c)).

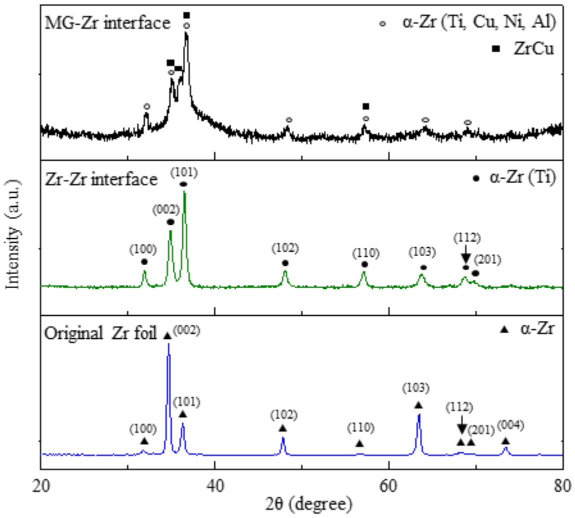

Figure 18. XRD patterns obtained at the MG–Zr interface and the Zr–Zr interface.

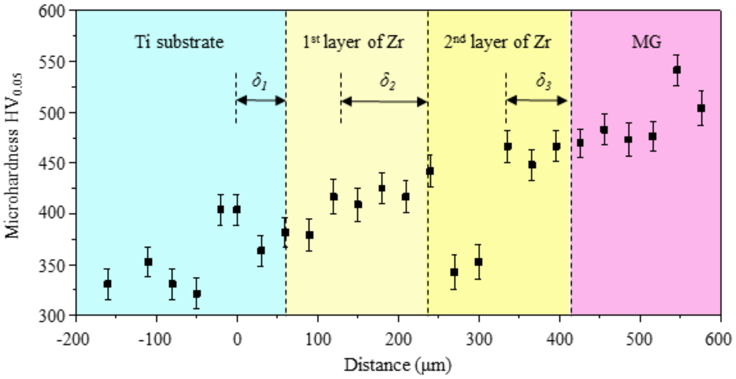

Figure 19. Micro-hardness profile of the MG–Ti bonding with two Zr intermediate layers.

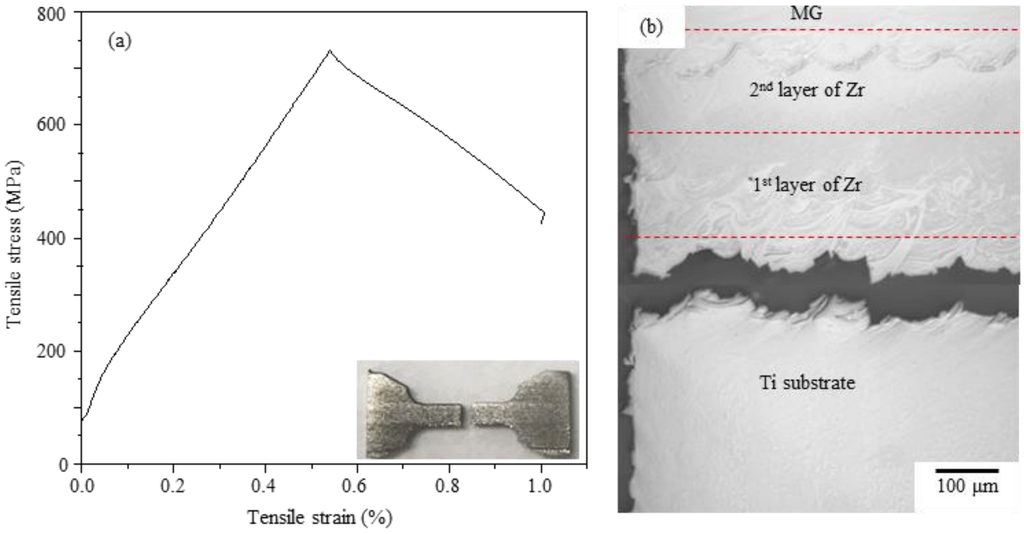

Figure 20. (a) Tensile stress-strain curve of the MG–Ti bonding with two intermediate layers; (b) OM image showing the fracture position of the tensile test specimen.

Tensile test was then performed on the joints with two Zr intermediate layers to measure the bonding strength between the MG part and the Ti substrate. The stress-strain curve is shown in Figure 20(a). Unlike the joint with only one intermediate layer which failed at the MG−Zr interface during EDM cutting, the tensile test specimens with two intermediate layers fractured at the Zr−Ti interface, as shown in Figure 20(b). Apparently, the improved MG−Zr interface when two intermediate layers were used is contributed by the very high Zr content and the resultant formation of α-Zr phase at the MG−Zr interface, as shown in Figures 17 and 18. The average bonding strength between the MG part and the Ti substrate is 758 ± 52 MPa (Figure 20(a)). This strength is 20% less than the UTS of Ti64 alloy (~ 950 MPa), but is 62% higher than the UTS of Zr 702 (~ 468 MPa). This increase of strength is caused by the solid solution strengthening of α-Zr (Figure 13) [20]. However, the specimen shows nearly no plastic deformation prior to failure, indicating a brittle fracture. The fracture surface after tensile test exhibits mostly brittle fracture morphology, with some ductile dimples, as shown in Figure 21. Micro-cracks and pores are also observed from the fracture surface, which may be the sites of fracture initiation. The severely reduced ductility of the Zr−Ti interface might be related to the solid solution hardening and the defects.

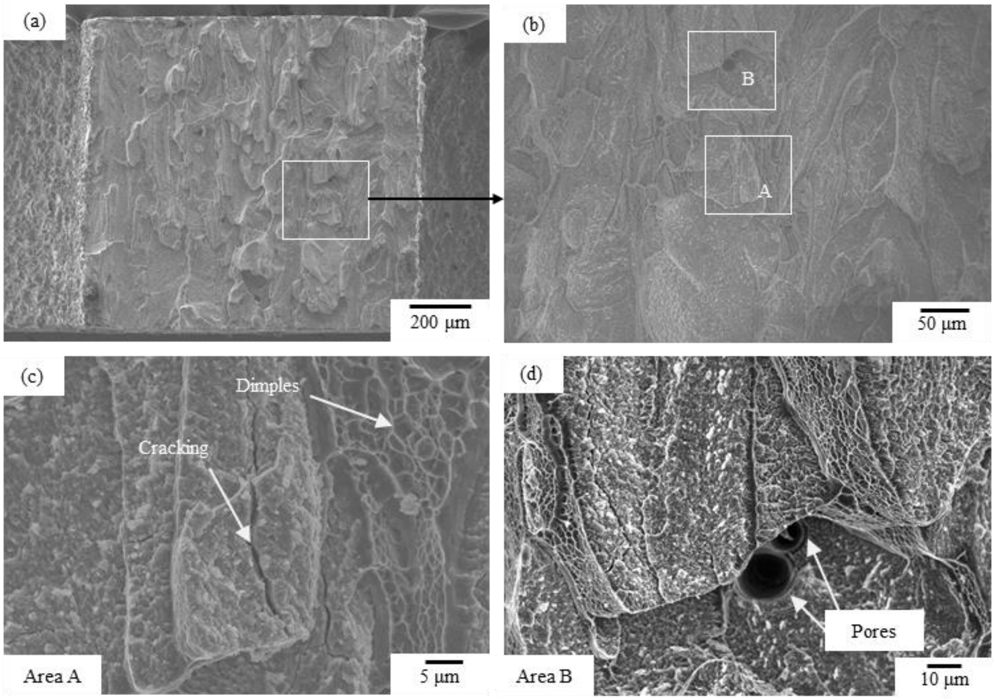

Figure 21. SEM images showing the fracture surface of the MG–Ti bonding with two intermediate layers after tensile test.

4. CONCLUSIONS

$Zr_{65.7}Ti_{3.3}Al_{3.7}Ni_{11.7}Cu_{15.6}$ metallic glass (MG) parts were successfully built upon Ti-6Al-4V substrates by laser-foil-printing additive manufacturing in this paper. The results are summarized as follows:

(1) Pores, cracking, and crystallization were not observed in the printed MG part, and its glass transition temperature, crystallization temperature, micro-hardness, and tensile strength were nearly the same as the original MG material.

(2) When directly building a MG part on the Ti substrate, the welded MG foil peeled off from the substrate due to the formation of hard and brittle intermetallic compounds at the MG−Ti interface caused by excessive mixing of the melted Ti substrate with the MG.

(3) When one Zr intermediate layer (~200 µm thick) was used, there was still ~5−13 wt.% of Ti mixed with the MG and intermetallics formed at the MG−Zr interface. Therefore, the sample fractured at the MG−Zr interface during cutting tensile specimens.

(4) When two Zr intermediate layers were used (~ 400 µm thick), the Ti substrate and the MG part had a bonding strength of ~ 758 MPa, and the tensile test specimen fractured at the Zr−Ti interface. This improved bonding was contributed by the very high Zr content and the resultant formation of α-Zr phase.

ACKNOWLEDGEMENTS

This work was supported by the Department of Energy [grant number DE-FE0012272] and the University of Missouri System [award number FastTrack-16002R].

REFERENCES

[1] J. Schroers, Processing of bulk metallic glass, Adv. Mater. 22 (2010) 1566–1597.

[2] W.H. Wang, C. Dong, C.H. Shek, Bulk metallic glasses, Mater. Sci. Eng. R 44 (2004) 45–89.

[3] A. Inoue, A. Takeuchi, Recent development and application products of bulk glass alloys, Acta Mater. 59 (2011) 2243–2267.

[4] H. Sun, K.M. Flores, Laser deposition of a Cu-based metallic glass powder on a Zr-based glass substrate, J. Mater. Res. 23 (2011) 2692–2703.

[5] H. Sun, K.M. Flores, Microstructural analysis of a laser-processed Zr-based bulk metallic glass, Metall. Mater. Trans. A 41 (2010) 1752–1757.

[6] H.Y. Jung, S.J. Choi, K.G. Prashanth, M. Stoica, S. Scudino, S. Yi, U. Kühn, D.H. Kim, K.B. Kim, J. Eckert, Fabrication of Fe-based bulk metallic glass by selective laser melting: a parameter study, Mater. Des. 86 (2015) 703–708.

[7] X.P. Li, C.W. Kang, H. Huang, L.C. Zhang, T.B. Sercombe, Selective laser melting of an $Al_{86}Ni_6Y_{4.5}Co_2La_{1.5}$ metallic glass: processing, microstructure evolution and mechanical properties, Mater. Sci. Eng. A 606 (2014) 370–379.

[8] Y. Shen, Y. Li, C. Chen, H.L. Tsai, 3D printing of large, complex metallic glass structures, Mater. Des. 117 (2017) 213–222.

[9] B.E. Carroll, R.A. Otis, J.P. Borgania, J. Suh, R.P. Dillon, A.A. Shapiro, D.C. Hofmann, Z. Liu, A.M. Beese, Functionally graded material of 304L stainless steel and inconel 625 fabricated by directed energy deposition: characterization and thermodynamic modeling, Acta Mater. 108 (2016) 46–54.

[10] R. Liontas, J.R. Greer, 3D nano-architected metallic glass: size effect suppresses catastrophic failure, Acta Mater. 133 (2017) 393–407.

[11] G. Wang, Y.J. Huang, M. Shagiev, J. Shen, Laser welding of $Ti_{40}Zr_{25}Ni_3Cu_{12}Be_{20}$ bulk metallic glass, Mater. Sci. Eng. A 541 (2012) 33–37.

[12] H.S. Wang, H.G. Chen, J.S.C. Jang, M.S. Chiou, Combination of a Nd:YAG laser and a liquid cooling device to $(Zr_{53}Cu_{30}Ni_9Al_8)Si_{0.5}$ bulk metallic glass welding, Mater. Sci. Eng. A 528 (2010) 338–341.

[13] N.H. Tariq, B.A. Hasan, J.I. Akhter, Evolution of microstructure in $Zr_{55}Cu_{30}Al_{10}Ni_5$ bulk amorphous alloy by high power pulsed Nd:YAG laser, J. Alloy. Compd. 485 (2009) 212–214.

[14] B. Li, Z.Y. Li, J.G. Xiong, L. Xing, D. Wang, Y. Li, Laser welding of $Zr_{45}Cu_{48}Al_7$ bulk glassy alloy, J. Alloy. Compd. 413 (2006) 118–121.

[15] S. Kagao, Y. Kawamura, Y. Ohno, Electron-beam welding of Zr-based bulk metallic glasses, Mater. Sci. Eng. A 375 (2004) 312−316.

[16] J. Kim, Y. Kawamura, Electron beam welding of the dissimilar Zr-based bulk metallic glass and Ti metal, Scr. Mater. 56 (2007) 709−712.

[17] J. Kim, Y. Kawamura, Electron beam welding of Zr-based BMG/Ni joints: effect of beam irradiation position on mechanical and microstructural properties, J. Mater. Process. Technol. 207 (2008) 112−117.

[18] J. Kim, Y. Kawamura, Dissimilar welding of $Zr_{41}Be_{23}Ti_{14}Cu_{12}Ni_{10}$ bulk metallic glass and stainless steel, Scr. Mater. 65 (2011) 1033−1036.

[19] Y. Li, Y. Shen, C. Chen, M.C. Leu, H.L. Tsai, Building metallic glass structures on crystalline metal substrates by laser-foil-printing additive manufacturing, J. Mater. Process. Technol. 248 (2017) 249–261.

[20] E. Kobayashi, S. Matsumoto, H. Doi, T. Yoneyama, H. Hamanaka, Mechanical properties of the binary titanium-zirconium alloys and their potential for biomedical materials, J. Biomed. Mater. Res. 29 (1995) 943–950.

[21] M. Miller, P. Liaw, Bulk Metallic Glasses, Springer, New York, 2008.

[22] U. Kühn, J. Eckert, N. Mattern, L. Schultz, ZrNbCuNiAl bulk metallic glass matrix composites containing dendritic bcc phase precipitates, Appl. Phys. Lett. 80 (2002) 2478–2480.

[23] T. Massalski, H. Okamoto, P. Subramanian, L. Kacprzak, Binary Alloy Phase Diagrams, ASM, 1986.

[24] Z. Sun, J.C. Ion, Laser welding of dissimilar metal combinations, J. Mater. Sci. 30 (1995) 4205-4214.

[25] E. Mittemeijer, Fundamentals of Materials Science: the Microstructure- property Relationship Using Metals as Model System, Springer, Verlag Berlin Heidelberg, 2011.

III. ADDITIVE MANUFACTURING OF ZR-BASED METALLIC GLASS STRUCTURES ON 304 STAINLESS STEEL SUBSTRATES VIA V/Ti/ZR INTERMEDIATE LAYERS

Yingqi Li, Yiyu Shen, Chia-Hung Hung, Ming C. Leu, and Hai-Lung Tsai

Department of Mechanical and Aerospace Engineering, Missouri University of Science
and Technology, Rolla, MO 65409, United States

ABSTRACT

Welding of dissimilar metals is challenging, particularly between crystalline metals and metallic glasses (MGs). In this study, $Zr_{65.7}Cu_{15.6}Ni_{11.7}Al_{3.7}Ti_{3.3}$ (wt%) MG structures were built on 304 stainless steel (SS) substrates by laser-foil-printing (LFP) additive manufacturing technology in which MG foils were laser welded layer-by-layer onto the SS substrate with a transition route, i.e., SS → V → Ti → Zr → MG. The direct welding of MG on SS would lead to the formation of various brittle intermetallics and the consequent peeling off of the welded MG foils from the SS substrate, which could be resolved via the use of V/Ti/Zr intermediate layers. The chemical composition, formed phases, and micro-hardness were characterized in the dissimilar joints by energy dispersive spectroscopy, X-ray diffraction, and micro-indentation. Since the intermediate materials were highly compatible with the base metals or the adjacent intermediate metals, undesirable intermetallics were not detected in the dissimilar joint. The bonding tensile strength between the SS substrate and the MG part with intermediate layers was measured about 477 MPa.

1. INTRODUCTION

Owing to the amorphous atomic structure, metallic glasses (MGs) usually exhibit high strength, elasticity, hardness, corrosion resistance, wear resistance, etc., compared with conventional crystalline metals [1,2]. However, there are thickness and geometry limitations for current MG products due to the insufficient cooling rate during casting [3].

In the recently developed laser-foil-printing (LFP) additive manufacturing (AM) technology, metal foils are laser welded layer-by-layer to fabricate three-dimensional (3D) structures [4]. The LFP technology has already shown its capability to fabricate freeform 3D MG structures with fully amorphous and large dimensions [5−7], owing to the intrinsic advantage of fabricating complex geometries of AM technology [8] and the high heating and cooling rates of laser processing [5,9]. In LFP, crystalline metals have to be used as the foundation substrates upon which MG structures are built, since thick, large as-cast MG plates are difficult to obtain. A good bonding between the MG and the crystalline metal is therefore essential to avoid peeling off of the welded MG foils from the crystalline substrate before the desired structure has been built.

On the other hand, joining dissimilar materials is increasingly needed as engineering applications are seeking creative new structures with local tailored functions and properties [10]. For example, a structure may need good corrosion resistance in one area and high toughness in another location. The LFP technology is able to directly build up a freeform structure with varied properties by welding dissimilar metal foils at different desired locations during fabrication. Despite high strength, hardness, corrosion resistance, etc., monolithic MGs lack macroscopic ductility since they do not possess crystalline structures, which makes them unsuitable for structural engineering applications [1]. For example, $Zr_{65.7}Cu_{15.6}Ni_{11.7}Al_{3.7}Ti_{3.3}$ MG, which is selected for this study, has a yield strength of ~1524 MPa, a Vickers micro-hardness of ~563, and superior corrosion resistance to 316 stainless steel (SS); however, it exhibits negligible tensile ductility (~1.6%) (data source: Liquidmetal® datasheet). Moreover, to date many commercially available MGs are very costly, since they are made from expensive metals with high purity, e.g., high-purity Zr [11]. 304SS is widely used in industrial applications, such as chemical equipment, marine equipment, pressure vessels, etc. In addition, 304SS has much higher ductility (minimum ~40%, annealed condition [12]) and is also much cheaper than Zr-based MG. Therefore, the ability to fabricate multi-material structures from Zr-based MG and 304SS using LFP technology would either offer more flexibility in the design of MG products or provide additional functions to the 304SS parts.

In this study, we attempted to fabricate $Zr_{65.7}Cu_{15.6}Ni_{11.7}Al_{3.7}Ti_{3.3}$ MG structures on 304SS substrates using LFP technology. One of the challenges in building such multi-material structure is to obtain a sound dissimilar joint between 304SS and Zr-based MG. Welding of SS to Zr-based MG is rarely reported in the literature [13,14]. Direct fusion welding of SS to Zr-based MG could lead to the formation of various brittle intermetallics due to the compositional mixing of dissimilar materials, lack of solubility, atomic structure mismatch between different elements (i.e., Fe, Cr, Ni, Zr, Al, Cu, and Ti), etc. [13,15]. A feasible way to reduce the brittleness caused by the formation of intermetallics is application of intermediate metal that is highly compatible with both the 304SS and Zr-based MG. Unfortunately, there is no single metal meeting this requirement.

A proper combination of intermediate metals that are highly compatible with the adjacent materials would be useful to suppress the formation of intermetallics between 304SS and Zr-based MG. When Zr-based MG parts are built on Zr substrates using LFP, a sound joint between the Zr substrate and the Zr-based MG part can be obtained due to the formation of αZr solid solution [16]. Hence, Zr can be chosen as the intermediate material adjacent to the Zr-based MG. The metals that do not form intermetallics with Zr include Ti, Nb, Hf and Ta. Among them, Ti is the most commonly used material. In addition, in our previous study, the bonding strength between Zr-based MG part and Ti substrate with Zr intermediate layers could reach 758 MPa [6]. On the other hand, welding Ti to SS has been extensively studied in the literature [17−23]. Direct fusion welding of Ti to SS would result in the formation of highly brittle Fe–Ti intermetallics [21]. To suppress the formation of brittle Fe–Ti intermetallics, intermediate materials that have substantial extent of solid solubility in Fe, such as Cu [22] and Ni [20], have been used to prevent direct interaction between Ti and SS. However, the formation of other intermetallics, e.g., Ni–Ti intermetallics, Cu–Ti intermetallics, occurred, and the tensile strength of such joints rarely exceeded 360 MPa. V is another candidate of intermediate materials for welding Ti to SS, since it is completely soluble in Ti or Cr according to the Ti–V and Cr–V equilibrium phase diagrams [15]. In addition, V has considerable solid solubility in Fe. Although there is a possibility of forming brittle σ phase that precipitates from a solid solution between Fe and V [15,19], some researchers have reported that σ phase between Fe and V is difficult to form under rapid cooling in laser welding [17], TIG welding [18], or electron beam welding [24]. Based on the above analysis, a transition route, i.e., 304SS → V → Ti → Zr → Zr-based MG, was designed to improve the dissimilar joint between 304SS and Zr-based MG in this study. The properties of the printed Zr-based MG part have been discussed in our other publication [6], and this paper will focus on the study of the dissimilar joint between the 304SS substrate and the Zr-based MG part from the aspects of chemistry, formed phases, and mechanical properties. For comparison, the direct joint between 304SS and Zr-based MG is also discussed in this paper. This work would lay the foundation for manufacture of freeform multi-material structures from SS and Zr-based MG using AM technology.

2. EXPERIMENTAL

The LFP AM technology was used in this experiment. The detailed discussion of the LFP system can be found in [4,5]. However, to facilitate and help understanding the following discussion, a short description of the LFP process is given below. A layer of metal foil was placed on a substrate which was mounted on a three-axis motion stage (Aerotech). Two lasers were used: a continuous wave fiber laser (IPG YLP-1000) with 1070 nm wavelength for welding and a pulsed UV laser (Coherent AVIA-355X) with 355 nm wavelength and 30 ns pulse duration for foil-cutting. The welding laser beam entered a scanner (SCANLAB) and then was focused on the foil surface. The beam diameter (*D*) at the focus was about 170 µm. First, the foil was fixed onto the substrate via laser spot welding using a mold-plate with a predetermined hole-pattern which would prevent the foil from curving/distortion in the subsequent welding. Then, the scanner scanned multiple overlapped passes to weld the foil onto the substrate in selected regions. After the welding process was done, the motion stage shifted the workpiece to the location under the UV laser and the foil was cut by the UV laser along the contours of the welded regions to remove the excessive foil. Another layer of fresh foil was placed on the top of the workpiece for the process of next layer. The above processes were repeated until the desired part was built. All samples were processed inside a chamber with Ar shielding gas flow.

A 12-mm-thick 304SS (AISI type) plate was used as the substrate in this experiment. The MG part was fabricated by welding MG foils onto the substrate layer-by-layer. The nominal chemical composition of the selected MG foil was $Zr_{65.7}Cu_{15.6}Ni_{11.7}Al_{3.7}Ti_{3.3}$ (wt%) (Liquidmetal®, LM105), with a thickness of ~200 µm for each layer. A combination of pure V foils (purity 99.8%, 2 layers), pure Ti foils (purity 99.2%, 3 layers), and pure Zr foils (Grade 702, 2 layers) was used as the intermediate layers between the SS substrate and the MG part, as shown in Figure 1(a). The thickness of a layer of V foil, Ti foil, and Zr foil was 125, 100, and 200 µm, respectively. The selection of foil thickness was just based on availability. Two or three layers of each intermediate material were used in order to minimize the undesired elements from the previous adjacent material to migrate and mix with the next adjacent material. For example, two layers of V foil were used between SS and Ti to reduce the content of Fe in the Ti layers to less than 5 wt%. After the V foils, Ti foils and Zr foils were welded sequentially, 25 layers of MG foil were welded onto the workpiece to construct a 5-mm-thick MG part (Figure 1(b)). Before laser processing, the substrate and foils were slightly grinded using abrasive papers to remove possible surface oxides, and then cleaned using ethanol. The laser power (P), laser scanning speed (v) and hatch space (Δd) for each layer of welding are listed in Table 1. The P and v values were selected after a parametric study to ensure continuous and stable welding passes and small penetration depth at the same time. Note that there was no intention to optimize the process parameters, but the selected parameters aparently could achieve sound welding. To reduce heat accumulation, the time lapse between two adjacent scan passes was 10 s.

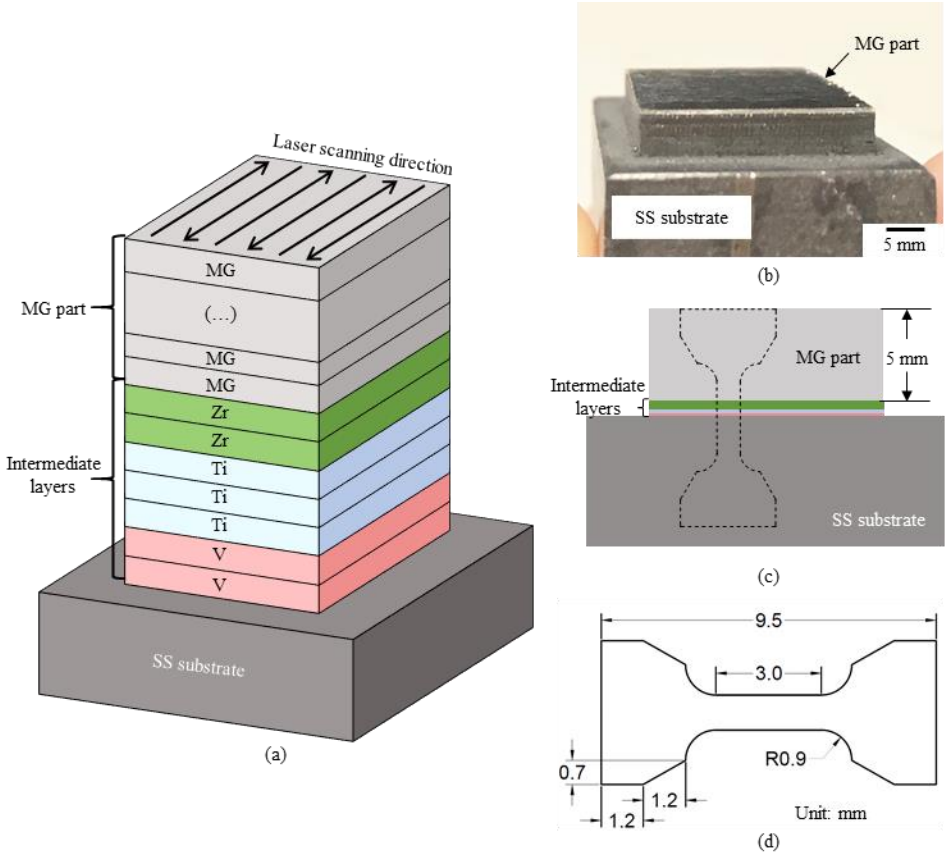

Figure 1. (a) Schematic showing the arrangement of the intermediate layers when printing a MG part on a SS substrate; (b) image showing a MG part printed on a SS substrate; (c) schematic showing how a tensile test specimen was extracted; (d) dimensions of the tensile test specimen. Note, (a) and (c) are not drawn to scale.

After the MG part was built, miniature tensile test specimens were cut from the substrate and the MG part by wire electric discharge machining (EDM) to test their bonding strength, as schematically shown in Figure 1(c). Figure 1(d) shows the dimensions of the miniature tensile test specimens with a thickness of 1 mm. The tensile test was conducted on an INSTRON-5969 universal testing machine with a clip-on extensometer. The extensometer was removed when the strain reached 1%. After removing the extensometer, the specimen was pulled to fracture and the strain was measured by the machine crosshead. The speed of the machine crosshead was maintained at 0.015 mm/mm/min throughout the test. Seven specimens were tested, and the average value with one standard deviation was reported.

Table 1. Parameters for each layer of welding

Layer	**Laser power *(P)* (W)**	**Laser scanning speed (*v*) (mm/s)**	**Hatch space (*Δd*) (mm)**
1st V layer	500	500	0.12
2nd V layer	500	450	0.12
1st Ti layer	400	600	0.12
2nd Ti layer	400	650	0.12
3rd Ti layer	400	650	0.12
1st Zr layer	500	470	0.12
2nd Zr layer	500	450	0.12
1st MG layer	500	590	0.12
2nd–25th MG layer	500	650	0.14

X-ray diffraction (XRD, Philips X'pert MRD), optical microscope (OM, Nikon Epiphot 200), and scanning electron microscope (SEM, Helios Nano Lab 600) were used to investigate the formed phases, cross-sections, and fracture surfaces after tensile testing. The chemical composition was analyzed by energy dispersive spectroscopy (EDS, Oxford AZtec) on the same SEM system with a silicon drift detector (Oxford X-Max). The accelerating voltage, emission current, and working distance for EDS analysis were 25 kV, 1.4 nA and 5 mm, respectively. Factory standardizations (Oxford, AZtec Version 3.3) were used for the calculation of quantitative results. The metallographic specimens for OM, SEM and EDS analyses were first grinded using 240 grit and 600 grit silicon carbide papers, and then polished using 9 μm and 3 μm diamond suspensions. This was followed by a final polishing with the application of 0.04 μm colloidal silica suspension. The micro-hardness was measured using a Vickers micro-hardness tester (Struers, Duramin 5) with 50 or 100 g load and 10 s load duration. The reported micro-hardness value was the average of five measurements with one standard deviation.

3. RESULTS AND DISCUSSION

The direct joining between SS and MG without intermediate layer will be discussed first. Figure 2 shows the weld surface and the transverse cross-section (perpendicular to the laser scanning direction) after welding a layer of MG foil onto the SS substrate at $P = 500$ W, $v = 600$ mm/s, $\Delta d = 0.15$ mm. It can be seen that the direct SS−MG joint is highly brittle. On the weld surface, the transverse cracking nearly passes through the whole surface (see Figure 2(a)). Cracking is also observed from the cross-section, especially at the bottom of the weld metal (see Figure 2(b)).

Figure 3 shows the EDS maps of the constituent elements in the direct SS−MG joint corresponding to Figure 2(b). The chemical composition distribution along the white arrow in Figure 3(a) is shown in Figure 4. From the EDS maps, a large-scale mixing between the melted SS and MG can be observed. At the bottom of the weld metal, the compositional mixing is more significant than the other areas in the joint (see Figure 4). In addition, the bottom of the weld metal has the highest cracking susceptibility on the transverse cross-section (see Figure 2(b)), which indicates that the formation of cracking is mainly associated with the compositional mixing between dissimilar materials.

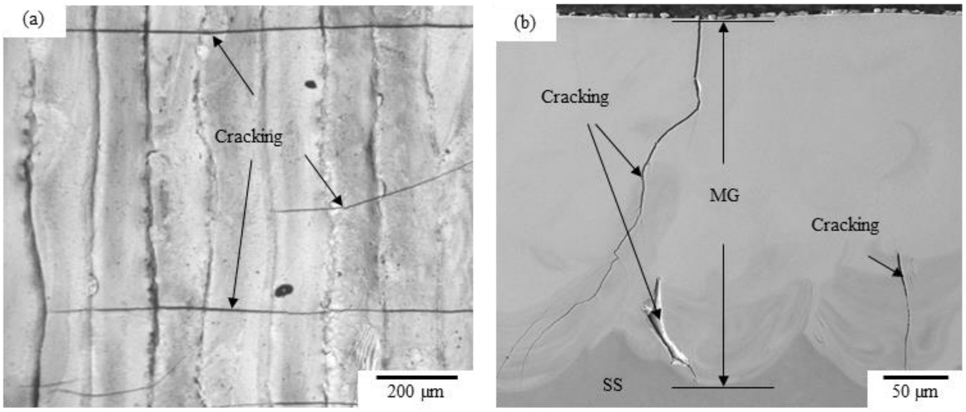

Figure 2. The direct SS−MG joint: (a) OM image of the weld surface; (b) secondary electron image of the transverse cross-section.

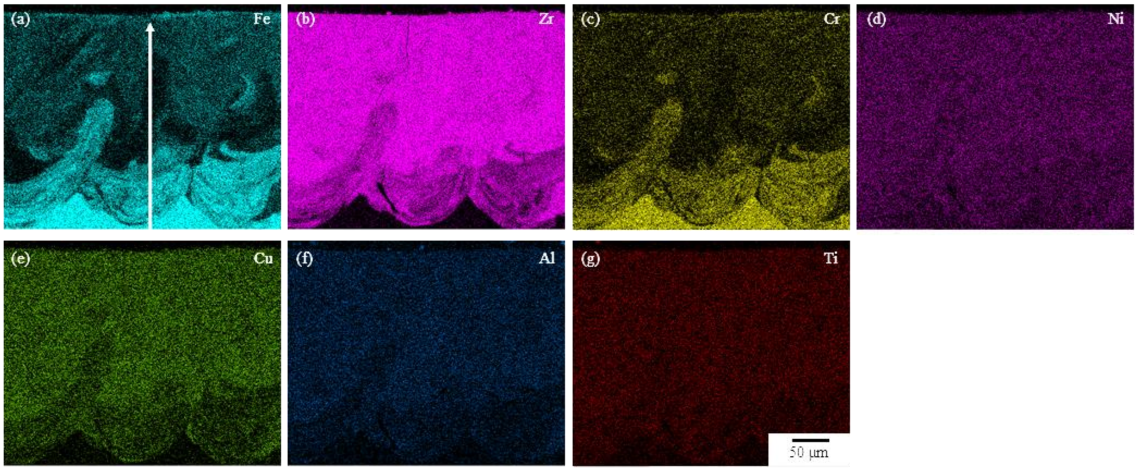

Figure 3. EDS maps of the constituent elements corresponding to Figure 2(b).

At least seven elements (Zr, Fe, Cr, Ni, Al, Cu and Ti) were detected in the weld metal (Figure 4). Due to lack of solubility between these elements, for example, Zr and Fe, various intermetallics formed in the direct SS−MG joint, which can be seen from the

XRD pattern obtained on the weld surface (see Figure 5). It is difficult to exactly identify all the formed intermetallics, since at least seven elements are present in the weld metal, and their ternary or higher order phase diagrams are usually not available. Hence, only several possible intermetallics based on the binary systems, i.e., ZrCu, $AlNi_3$, $NiZr_2$, $Al_{13}Cr_2$, and $FeZr_4$, are labeled in Figure 5, and there might be other binary, ternary or higher order intermetallics formed but not identified.

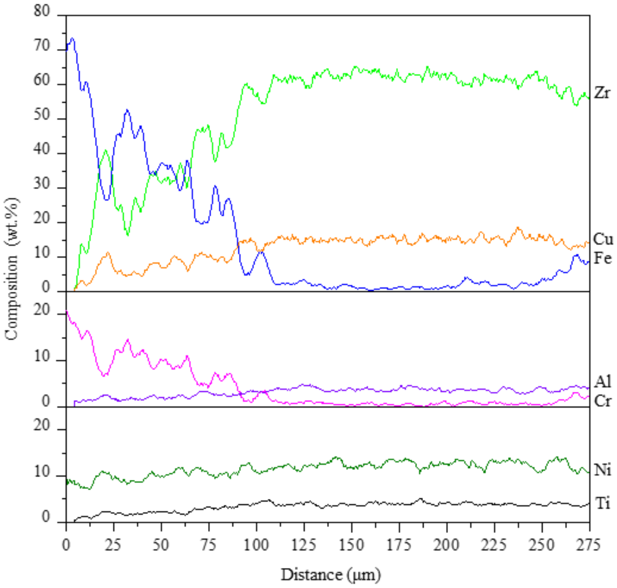

Figure 4. Chemical composition distribution along the white arrow in Figure 3(a).

Figure 6 is the Vickers micro-hardness profile of the direct SS–MG joint. It can be seen that the micro-hardness value of the direct SS–MG joint, especially at the bottom of the weld metal, is much higher than that of the original SS (~300 HV), and even larger than that of the original MG material (~560 HV). Obviously, the significantly increased micro-hardness is caused by the formation of intermetallics in the direct SS–MG joint. Residual stresses were developed during welding due to the thermal expansioncontraction mismatch caused by the differences in coefficient of thermal expansion between dissimilar materials. Since the direct SS−MG joint was highly brittle owing to the formation of intermetallics, the developed residual stresses would cause it to crack easily and promptly. When additional layers of MG foil were further welded onto it, the MG layers peeled off from the substrate before the desired MG part was built.

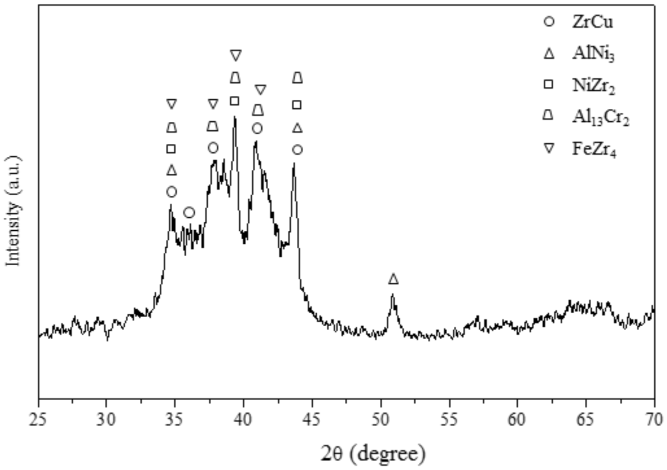

Figure 5. XRD pattern obtained on the weld surface when a layer of MG foil was directly welded onto a SS substrate.

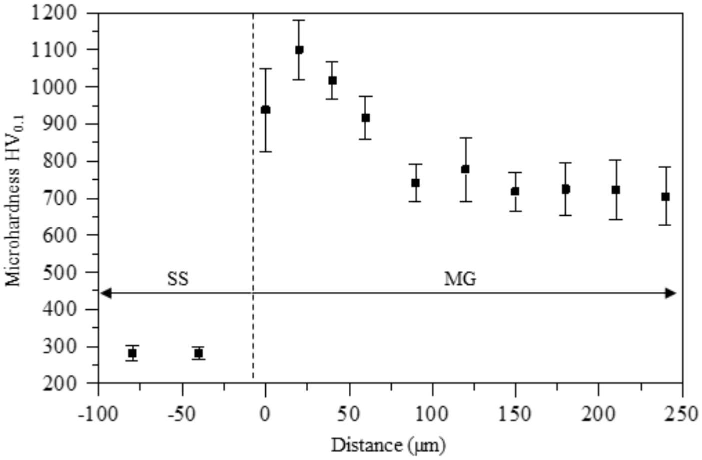

Figure 6. Micro-hardness profile of the direct SS−MG joint.

V, Ti and Zr intermediate layers were then welded between SS and MG layer-by-layer according to the sequence as shown in Figure 1(a) to suppress the formation of intermetallics. Figure 7 shows the transverse and longitudinal (parallel with the laser scanning direction) cross-sections of the SS−MG joint with V, Ti and Zr intermediate layers. It is difficult to perform effective etching on this joint since it has very complicated chemistry. Therefore, the cross-sections shown in Figure 7 were not etched. Unlike the direct SS−MG joint, cracking is not observed from the cross-sections of the SS−MG joint with intermediate layers, indicating an improved joint. In this paper, the penetration depth is defined as the distance that fusion extends into the substrate or the previous layer from the surface during welding. Since there is an overlap in the penetration area between two consecutive layers, to facilitate the following discussion, when a layer is labeled on a cross-section, it only includes the area from the bottom of its penetration to the bottom of its next layer's penetration. For each intermediate material, e.g., Ti, the penetration depth is not constant for every layer since the laser scanning speed (see Table 1) or the underlying material is different for each layer of welding. For example, the 2nd Ti layer was welded to the 1st Ti layer with high V content, while the 3rd Ti layer was welded to the 2nd Ti layer with lower V content. Therefore, the thickness for the labeled layers on Figure 7 might be slightly different for each intermediate material, although the original foils have the same thickness.

In this paper, one of the purposes of each intermediate material is to prevent the adjacent material (below) from mixing with another adjacent material (above). Therefore, the chemistry evolution from the SS to the MG was firstly characterized by EDS.

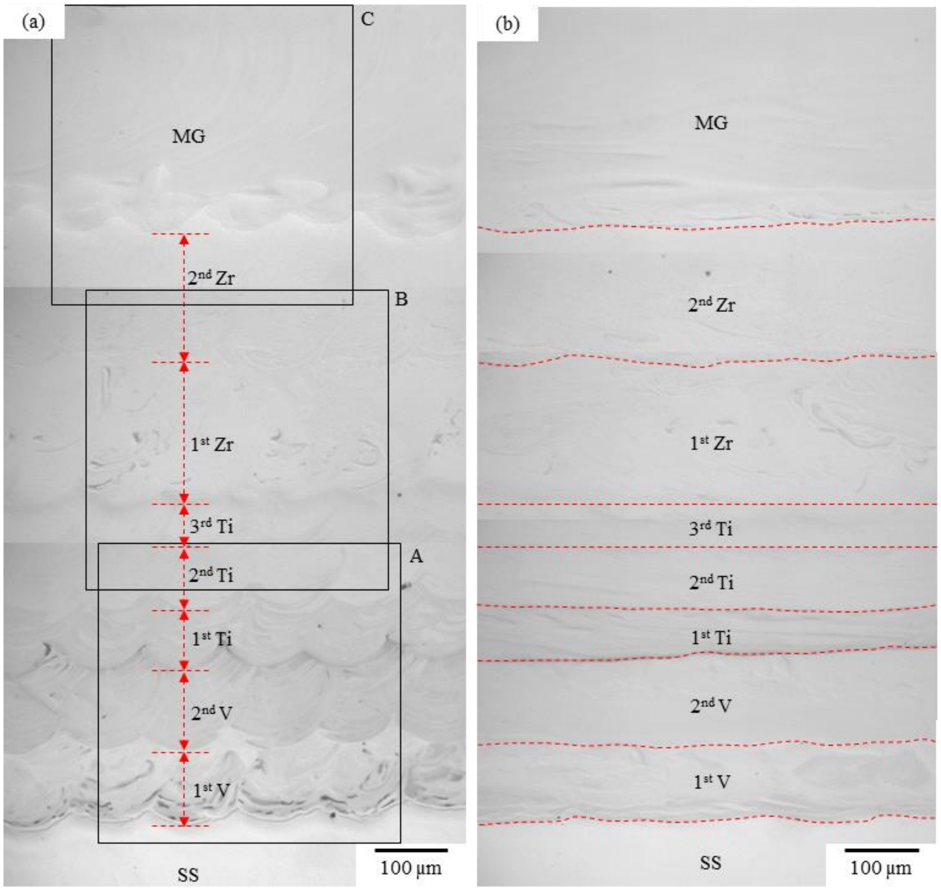

Figure 7. OM images of the SS–MG joint with V/Ti/Zr intermediate layers: (a) transverse cross-section; (b) longitudinal cross-section.

Figure 8 shows the EDS maps of the constituent elements in the SS substrate, the 1st and 2nd V layers, and the 1st and 2nd Ti layers corresponding to the area A in Figure 7(a). The EDS line scan was used to determine the chemistry as a function of position along the white arrow in Figure 8(a), and the quantitative results are shown in Figure 9. The EDS measured compositions of the SS substrate (Cr: ~18–20 wt%, Ni: 8–11 wt%, Fe: 71–72 wt%, see Figure 9) nearly do not deviate from the nominal compositions of AISI type 304SS (Cr: 18–20 wt%, Ni: 8–10.5 wt%, Fe: 66.345–74 wt%, Mn: max 2%). Mn (~2 wt%) was detected in the SS substrate by EDS but was not shown in Figures 8 and 9. Note, the EDS technique has an intrinsic uncertainty of ~1 wt% [10]. As expected, from the SS substrate to the Ti layers, the content of Fe, Cr and Ni decreases. In the 1st V layer, a large number of Fe, Ni and Cr elements are present (see Figures 8 and 9). However, the chemical composition distribution within the 1st V layer varies significantly (Figure 9). For example, along the white arrow on Figure 8(a), the V content varies in the range of 73–97 wt% and the Fe content fluctuates in the range of 1–20 wt%, as shown in Figure 9. In the 2nd V layer, the chemical composition distribution becomes relatively stable. Additionally, the V content and the Fe content are around 91–96 wt% and 2–6 wt%, respectively (Figure 9). Cr and Ni are also present in the 2nd V layer, and their total content is ~2–3 wt%.

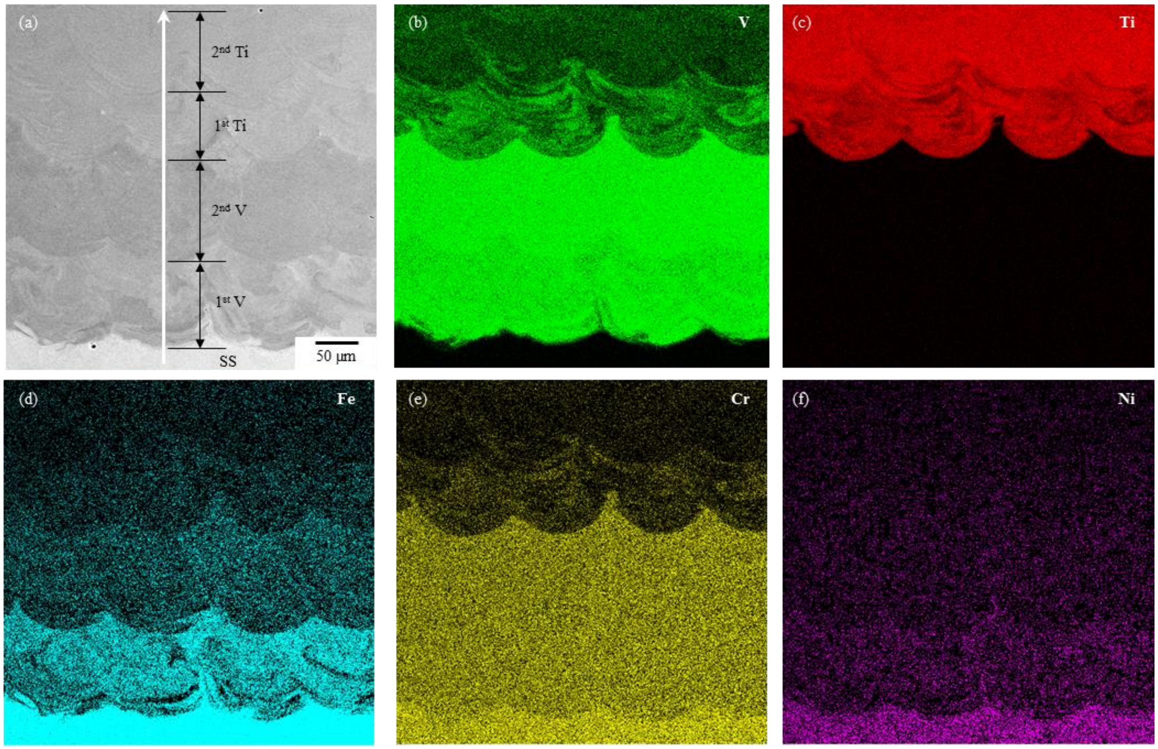

Figure 8. Secondary electron image (a) and EDS maps of the constituent elements (b–f) corresponding to area A in Figure 7(a).

Since the melted SS has been considerably diluted with the V layers, there are only small amounts of Fe, Cr and Ni in the Ti layers (totally ~1–4 wt%, see Figure 9). In the 1st Ti layer, a pronounced swirling distribution of V is observed (see Figure 8(b)), which is accompanied by a significant fluctuation of chemical composition distribution (see Figure 9). The Ti content and the V content in the 1st Ti layer vary in a range of 44–88 wt% and 10–51 wt%, respectively. In laser welding, the melted dissimilar materials were entrained upward and backward by the recoil pressure (forced convection) while the laser beam was moving in one direction [25], leading to a large-scale mixing between the molten dissimilar materials. In addition, the natural convection caused by the difference in density between dissimilar materials would enhance the forced convection. However, the mixing was incomplete and was “frozen” by rapid solidification of laser welding. The aforementioned phenomena would result in a swirling type mixing and a nonuniform chemical composition distribution in the weld metal. As the V content decreases, the swirling type distribution becomes less pronounced in the 2nd Ti layer (see Figure 8 and Figure 9).

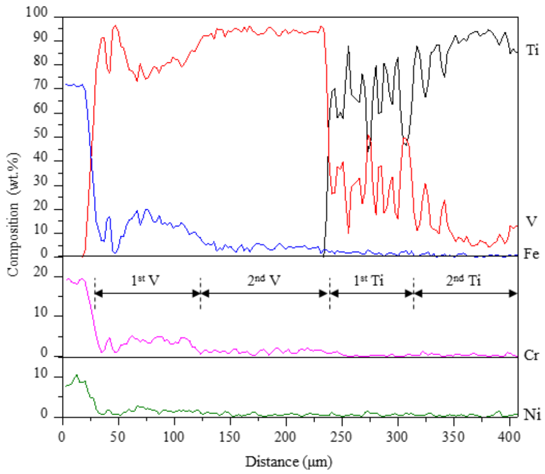

Figure 9. Chemical composition distribution along the white arrow in Figure 8(a).

Figure 10 shows the EDS maps of the constituent elements in the 2nd and 3rd Ti layers, and the 1st and 2nd Zr layers corresponding to the area B in Figure 7(a). Figure 11 shows the measured composition of the constituent elements along the white arrow in Figure 10(a). Fe, Cr and Ni were detected in the Ti layers but not detected in the Zr layers. Through the dilution with three layers of Ti, the detected V content is only ~1–4 wt% in the 1st Zr layer and ~1 wt% in the 2nd Zr layer (see Figure 11). In the 1st Zr layer, a swirling distribution of Zr and Ti is also observed (Figures 10 and 11), in which the content of Ti fluctuates in a range of 3–90 wt% and 8–97 wt% for Zr (Figure 11). However, the Ti content becomes relatively stable in the area close to the MG side. This is because the Ti content in the upper area of the 2nd Zr layer is very small (~5–7 wt%), and thus the variation in Ti distribution becomes much less prominent in this area.

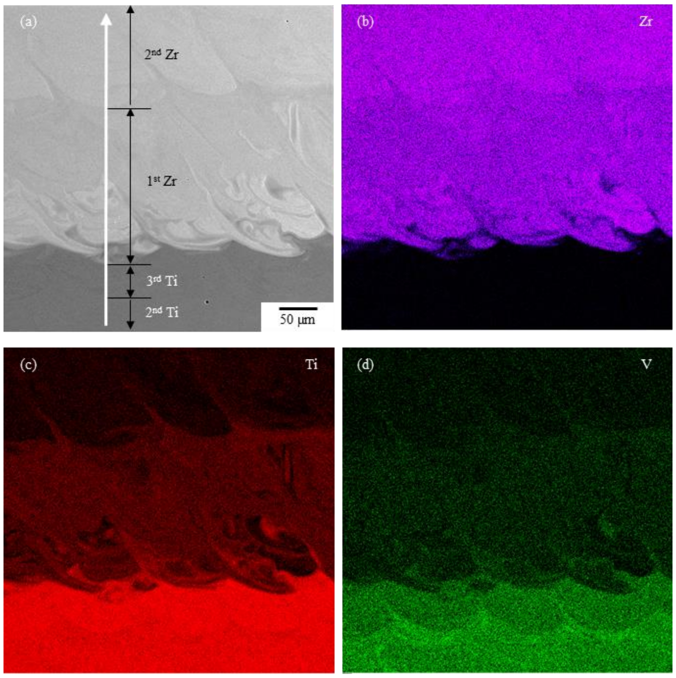

Figure 10. Secondary electron image (a) and EDS maps of the constituent elements (b–d) corresponding to area B in Figure 7(a).

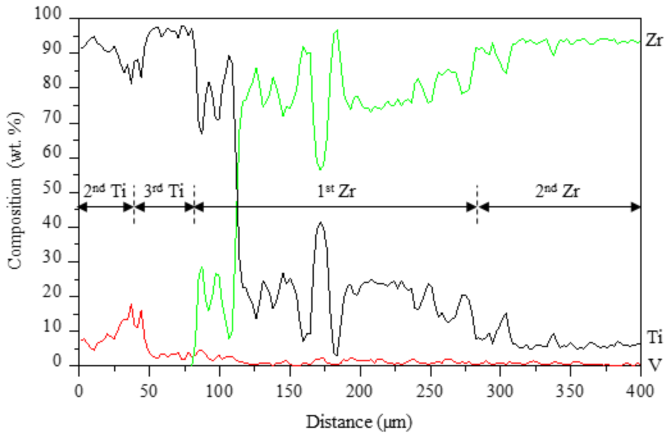

Figure 11. Chemical composition distribution along the white arrow in Figure 10(a).

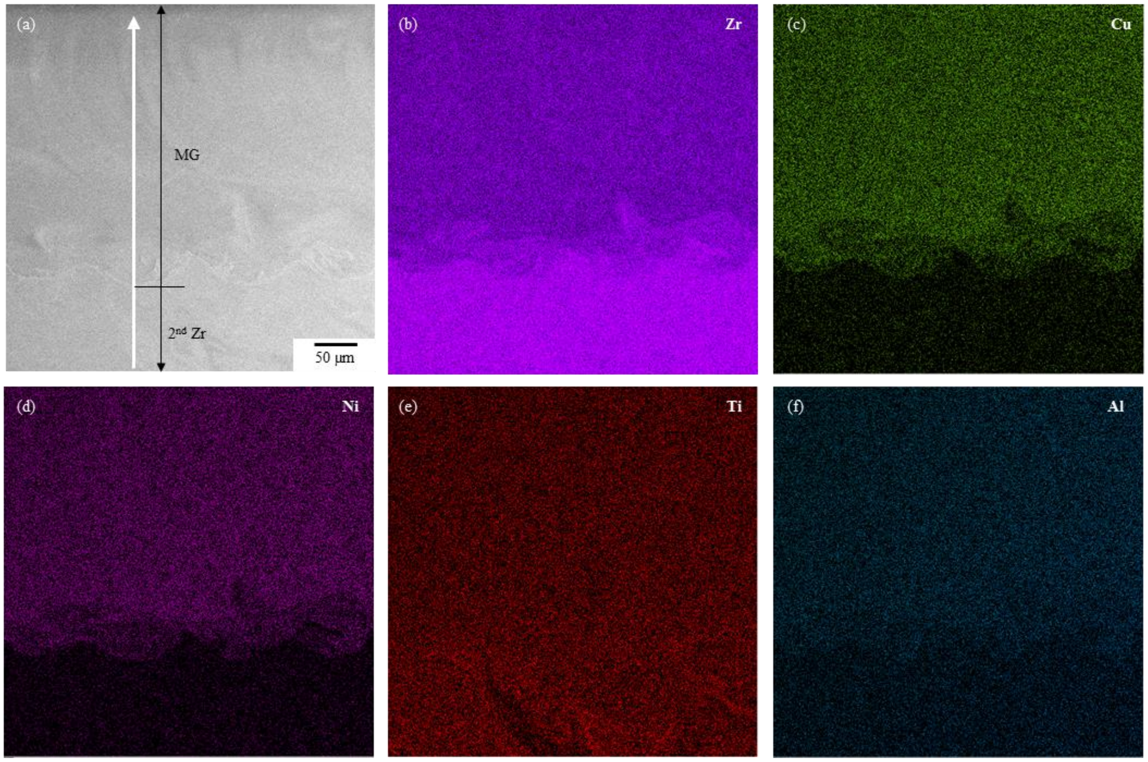

Figure 12. Secondary electron image (a) and EDS maps of the constituent elements (b–f) corresponding to area C in Figure 7(a).

Figure 12 shows the EDS maps of the constituent elements in the 2nd Zr layer and the 1st MG layer corresponding to the area C in Figure 7(a). The chemical composition distribution along the white arrow in Figure 12(a) is shown in Figure 13. Only Zr, Al, Ni, Cu and Ti elements are present in the 1st MG layer. It can be seen that the bottom of the MG has very high content of Zr (~80 wt%) owing to the mixing between the 2nd Zr layer and MG. Beyond this area, the chemical compositions in the MG do not deviate significantly from those of the original MG material (Zr: 64 wt%, Cu: 15 wt%, Ni: 12 wt%, Ti: 4 wt%, Al: 4 wt%, average of five spectra).

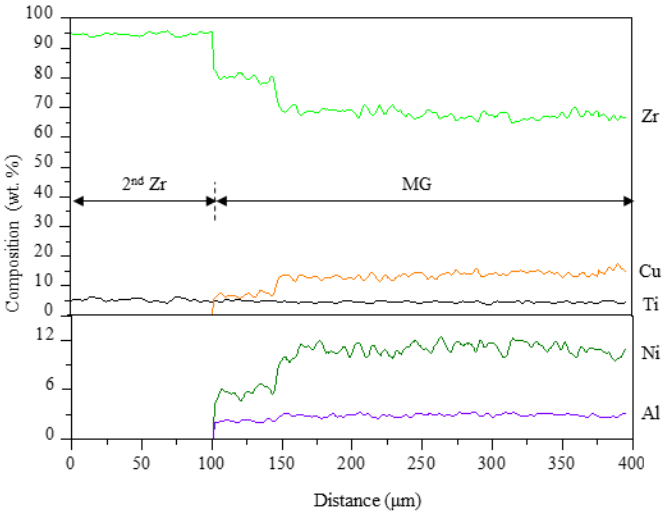

Figure 13. Chemical composition distribution along the white arrow in Figure 12(a).

XRD was then used to investigate if any intermetallic was formed in the intermediate layers. Since the irradiation area of the X-ray beam was larger than 2 × 2 mm^2 and the layer thickness was around or less than 0.2 mm, more than 10 layers would be included in the XRD pattern if the XRD test was directly performed on the cross-section, which would make the phase identification difficult. Hence, the XRD test was performed on the weld surface immediately after welding each intermediate layer, and the results are shown in Figure 14. For comparison, the XRD patterns of the original V foil, Ti foil and Zr foil are also included in Figure 14. The constituent phase of the original V foil, Ti foil, and Zr foil is V, αTi and αZr, respectively. αTi and αZr both have h.c.p. crystal structures, while V has a b.c.c. crystal structure.

According to the equilibrium Fe−V phase diagram [15], σ phase might be formed when the content of V is in the range of 22−88 wt%. Therefore, the 1st V layer, in which the V content is within this composition range (see Figure 9), has a risk of forming σ phase. However, the XRD pattern obtained on the weld surface of the 1st V layer does not show the diffraction peaks of σ phase; instead, the formed phase is V solid solution. This result is consistent with the results reported by Chu et al. during the TIG welding of V to steel [18] and Tomashchuk et al. during the laser welding of Ti64 to 316SS with V intermediate layer [24], in which σ phases were also not detected by XRD. The absence of σ phase might be contributed by rapid cooling of laser welding [17]. In the 2nd V layer, the content of V is above 92 wt%. Based on the Fe−V phase diagram, the constituent phase of the 2nd V layer should be V solid solution, which agrees with the XRD pattern obtained on the weld surface.

From the above chemical composition analysis (see Figures 9 and 11), it can be seen that the contents of the undesirable elements in the Ti layers, i.e., Fe, Cr and Ni, are trivial (less than 4 wt% in total). Therefore, in the Ti layers, the contents of Fe−Ti, Cr−Ti, Ni−Ti intermetallics, if formed, should be small. Moreover, the XRD patterns obtained on the weld surfaces after welding the 1st, 2nd and 3rd Ti layers do not show any intermetallic. Unlike the original Ti foil which is composed of αTi phase, the constituent phase of the 1st Ti layer is βTi solid solution. At room temperature, pure Ti has a h.c.p. crystal structure referred to as α phase. At 883 °C, the α phase transforms to a b.c.c.

structure known as β phase. The addition of V in pure Ti would decrease the transformation temperature from α phase to β phase and thus stabilize the β phase. Besides V, Fe, Cr and Ni are also β phase stabilizers [26]. V is completely miscible in the β phase. If the content of V is greater than 14–15 wt%, the β phase may be completely retained at room temperature with appropriate cooling rates [18]. In this study, the V content in most area of the 1st Ti layer is much higher than 15 wt% (see Figure 9); thus, the 1st Ti layer mainly consists of βTi solid solution. As the V content decreases in the Ti layers, its effect on stabilizing β phase reduces. Therefore, in the 2nd Ti layer, the structure becomes a mixture of αTi phase and βTi solid solution because of lower V content (~10 wt%). As the V content further decreases in the 3rd Ti layer (~2–4 wt%), only αTi phase is present in the XRD pattern. The maximum solubility of V in αTi is around 2 wt% [15].

In the Zr layers, the content of the undesired element, i.e., V, is also small (less than 4 wt%, see Figure 11). Therefore, the possibility of forming V–Zr intermetallics in the Zr layers is minimized. The XRD patterns obtained on the weld surfaces after welding the 1st and 2nd Zr layers indeed only show the diffraction peaks from αZr solid solutions. Compared to the XRD patterns of the original foils, the XRD patterns obtained on the intermediate layers exhibit the peak shift, peak broadening or change in relative intensity, which is mainly caused by solid solution effect and preferred orientation. The incorporation of solute elements in the crystal structure of pure metal would result in the change of lattice parameters, leading to the shift of Bragg peaks to higher or lower diffraction angles and the microstrain broadening of the Bragg peaks. The degree of variation in the lattice parameters is influenced by the content and the atomic radius of the solute elements.

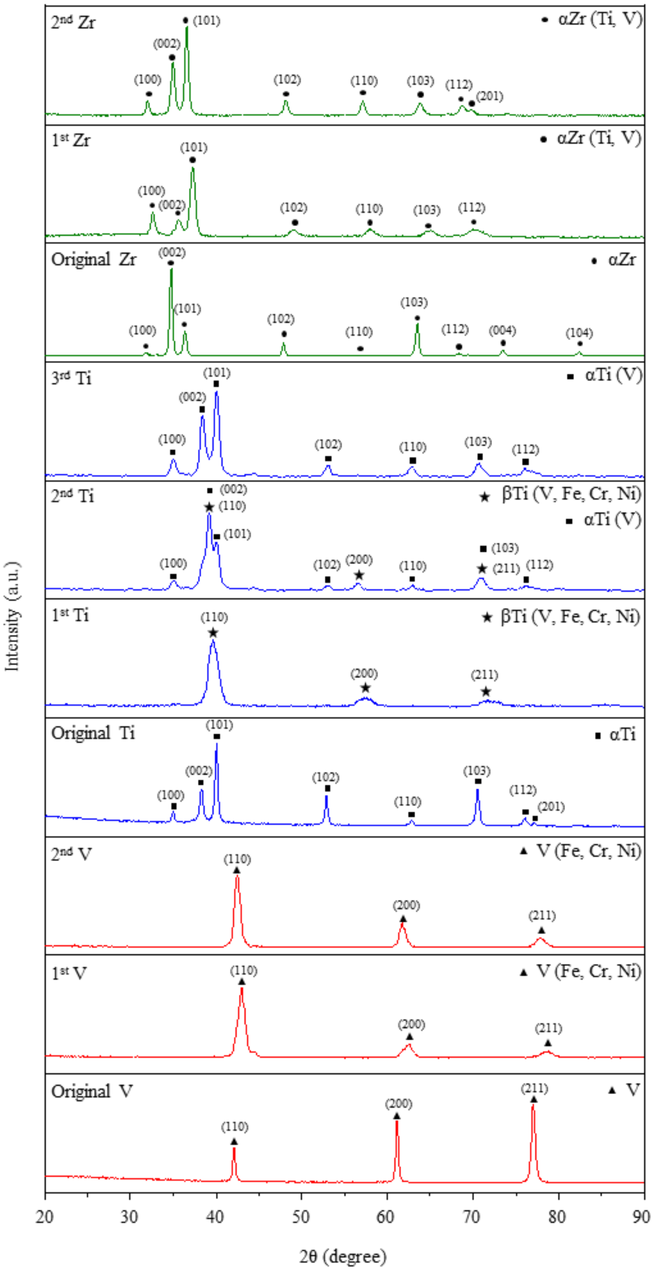

Figure 14. XRD patterns obtained on the weld surface after welding each intermediate layer.

XRD analysis was also conducted on the weld surfaces after welding the 1st and the 2nd MG layers, and then on the transverse cross-section of the fabricated MG part after removing the substrate and the intermediate layers, in order to investigate the microstructure evolution of the MG part during LFP. The results are shown in Figure 15. This figure also includes an XRD pattern obtained on the sample surface after removing about 200 µm thick material of the 1st MG layer by mechanical grinding, which shows the formed phases at the bottom of the 1st MG layer. It can be seen that at the bottom of the 1st MG layer αZr phase formed because of the very high Zr content (see Figure 13). The formation of αZr phase is beneficial for improving the bonding between MG and Zr [6,16]. In addition, βZr phase, amorphous phase and ZrCu intermetallic are also detected. Because of the low content of Cu at the bottom of the 1st MG layer (see Figure13), the formation of ZrCu would not considerably contribute to the brittleness of the weldment. For the XRD pattern obtained on the weld surface of the 1st MG layer, the fact that the sharp Bragg peak overlapping with the broad peak indicates that the MG foil was partially crystallized after laser welding. Since there is only one obvious Bragg peak present, the formed crystalline phase was not identified. However, no crystalline phase was observed by XRD on the weld surface of the 2nd MG. This result is consistent with that reported in our previous publication [16]. The partial crystallization of the 1st MG layer was caused by the change in chemical composition from the optimal chemistry of the original MG foil in local areas. During the welding of the 1st MG layer, considerable melting of the 2nd Zr layer occurred. The melted Zr was mixed with the melted MG by convection, leading to the change of chemical composition of the 1st MG layer which deteriorated its glass-forming ability [16]. For the 2nd MG layer, the adverse influence of

Zr layer on the glass-forming ability was trivial; thus, partial crystallization was not observed on the weld surface. The dilution (diluting the MG foil with the Zr layer) necessitates the second or more layers of MG foil in order to achieve fully amorphous state. The XRD result of the MG part confirms that the MG part is fully amorphous within the detection limit of XRD.

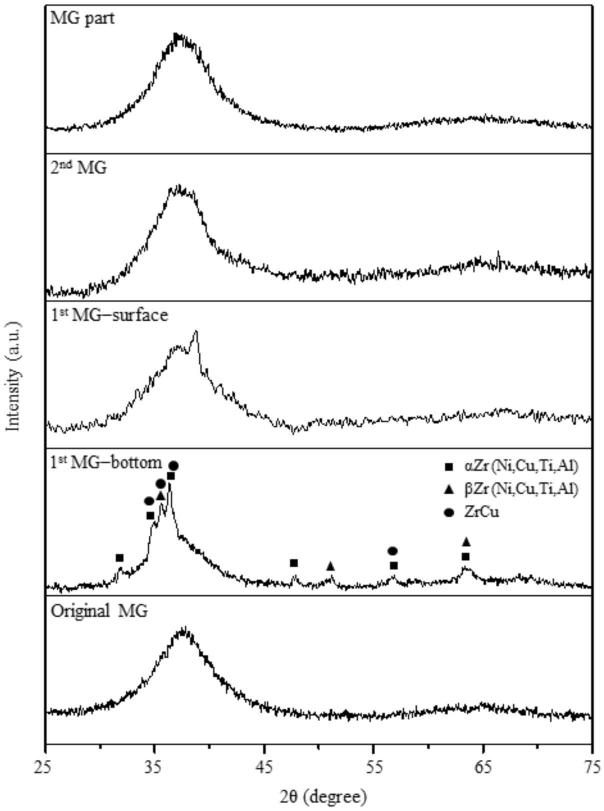

Figure 15. XRD patterns of the original MG foil, the 1st MG layer, the 2nd MG layer and the MG part.

Intermetallics usually exhibit very high hardness, and their formation would significantly harden the weld metal. When welding V to 316SS using electron beam, Nogami et al. found that the hardness of the weld metal was ~335–372 HV if the matrix phase was solid solution, but it would grow up to 900−1000 HV owing to the formation of σ phase after post welding heat treatment [24]. In addition, the hardness of Fe−Ti intermetallics can be as high as ~1000 HV [13]. Thus, the micro-hardness of the SS−MG joint with intermediate layers was measured to further check if there was any hard intermetallic formed. The micro-hardness test was performed on the longitudinal cross-section from the SS substrate through the intermediate layers to the MG part, and the results are shown in Figure 16. The SS substrate has a hardness of ~280 HV, while the hardness of the MG part is ~525 HV. In the 1st V layer, the hardness value is in the range of 370−460 HV, and this value is very close to the results reported by Tomashchuk et al. [17] and Nogami et al [24], which might indicate the absence of σ phase in the 1st V layer. The hardness value of the 2nd V layer (~260 HV) is smaller than that of the 1st V layer owing to the lower content of solute elements (see Figure 9). For the Ti layers, the hardness values do not exceed 450 HV. In the Zr layers, the hardness value in the 1st Zr layer (~410 HV) is much larger than that of the original Zr foil (~150 HV) because of the solid solution hardening, and then followed by a steep decrease due to the reduced solute content (i.e., Ti content) in the 2nd Zr layer (see Figure 11). At the bottom of the 1st MG layer, the hardness is slightly lower than that of the MG part due to the formation of softer αZr phase caused by the very high Zr content in this area [6]. Overall, along the micro-hardness profile, there is no area exhibiting remarkable high hardness, which indicates that there is no obvious formation of hard phases in the SS−MG joint with intermediate layers.

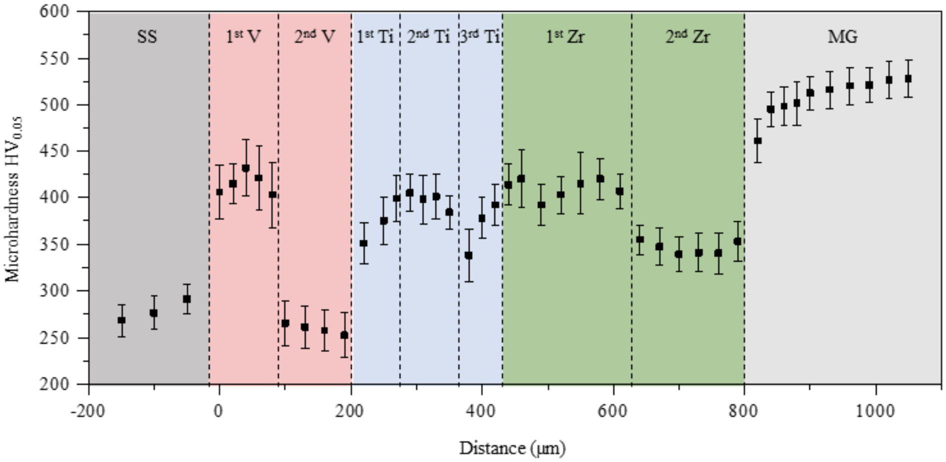

Figure 16. Micro-hardness profile of the SS−MG joint with intermediate layers.

The bonding strength of the SS−MG joint with intermediate layers was then measured by tensile test. The tensile stress−strain curve and the OM image of the cross-section showing the fracture position are provided in Figure 17. The tensile stress−strain curve shows a sudden stress drop at the strain around 1%. This stress drop was caused by removing the extensometer at the 1% strain during the tensile test. The tensile test specimen fractured at the V layers (Figure 17(b), with an ultimate tensile strength (UTS) of 477 ± 56 MPa (Figure 17(a)). This strength is slightly smaller than the UTS of annealed 304SS (~515 MPa) and annealed pure V (~538 MPa) [26]. In addition, the tensile specimen nearly did not show any plastic deformation prior to failure, indicating a brittle fracture (Figure 17(a)). Figure 18 shows the fracture surface after tensile test, and it can be seen that the fracture occurred by cleavage, producing distinct cleavage fracture surface features, such as flat regions, river patterns, and cleavage steps. Although undesirable σ phase between Fe and V was not formed in the V layers, the incorporation of Fe, Cr and Ni in V crystal structure might shift the ductile-to-brittle transition point of V above ambient temperature, leading to the brittle fracture behavior [17].

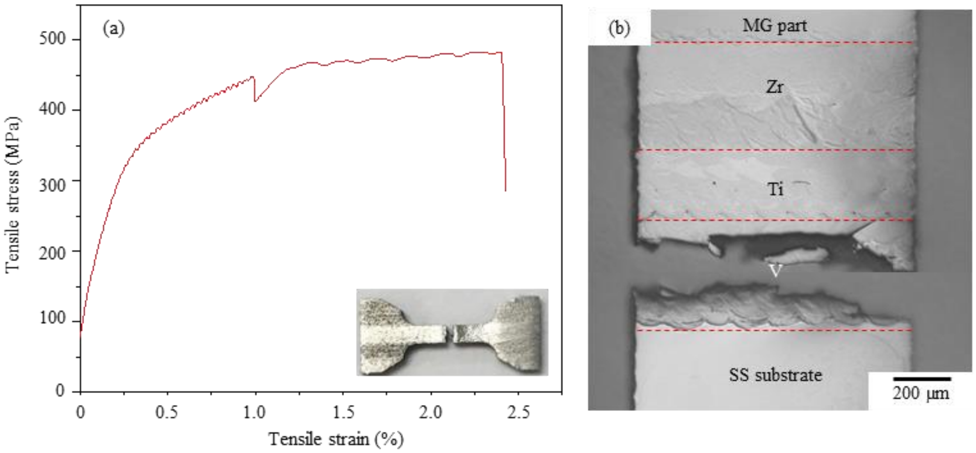

Figure 17. (a) Tensile stress–strain curve; (b) OM image showing the fracture position of the tensile specimen.

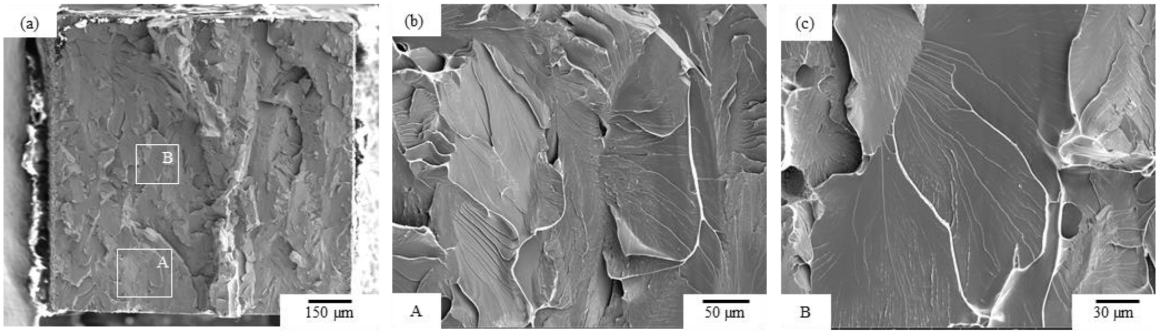

Figure 18. Secondary electron images of the fracture surface after tensile test.

4. CONCLUSIONS

In this paper, $Zr_{65.7}Cu_{15.6}Ni_{11.7}Al_{3.7}Ti_{3.3}$ metallic glass (MG) parts were built on 304 stainless steel (SS) substrates using laser-foil-printing additive manufacturing technology. The dissimilar joints between the SS substrate and the MG part with and without intermediate layers were studied and discussed in detail. The main conclusions are as follows:

(1) The direct SS−MG joint was highly brittle due to the formation of various hard and brittle intermetallics caused by the compositional mixing between SS and MG, lack of solubility between different elements (i.e., Fe, Cr, Ni, Zr, Al, Cu, and Ti).

(2) Through using a combination of V foils, Ti foils and Zr foils as intermediate layers, the SS−MG joint was significantly improved. Since the intermediate materials were highly compatible with the adjacent materials, and the contents of undesirable elements in each material were minimized through dilution, hard intermetallics were not detected in the joint. The main constituent phases of the joint were various solid solutions, e.g., V, βTi, αTi and αZr solid solutions.

(3) The tensile bonding strength of the SS−MG joint with V/Ti/Zr intermediate layers was about 477 MPa, and the tensile test specimen fractured in the V layers in a brittle manner.

ACKNOWLEDGEMENTS

This work was supported by the Department of Energy [grant number DE-FE0012272] and the University of Missouri System [award number FastTrack-16002R].

REFERENCES

[1] J. Qiao, H. Jia, P.K. Liaw, Metallic glass matrix composites, Mater. Sci. Eng. R 100 (2016) 1–69.

[2] A. Inoue, A. Takeuchi, Recent development and application products of bulk glass alloys, Acta Mater. 59 (2011) 2243–2267.

[3] J. Schroers, Processing of bulk metallic glass, Adv. Mater. 22 (2010) 1566–1597.

[4] C. Chen, Y. Shen, H.L. Tsai, A foil-based additive manufacturing technology for metal parts, ASME J. Manuf. Sci. Eng. 139 (2016) 024501.

[5] Y. Shen, Y. Li, C. Chen, H.L. Tsai, 3D printing of large, complex metallic glass structures, Mater. Des. 117 (2017) 213–222.

[6] Y. Li, Y. Shen, M.C. Leu, H.L. Tsai, Building Zr-based metallic glass part on Ti-6Al-4V substrate by laser-foil-printing additive manufacturing, Acta Mater. 144 (2018) 810–821.

[7] P. Bordeenithikasem, Y. Shen, H.L. Tsai, D.C. Hofmann, Enhanced mechanical properties of additively manufactured bulk metallic glasses produced through laser foil printing from continuous sheetmetal feedstock, Addit. Manuf. 19 (2018) 95–103.

[8] Y. Huang, M.C. Leu, J. Mazumder, A. Donmez, Additive manufacturing: current state, future potential, gaps and needs, and recommendations, ASME J. Manuf. Sci. Eng. 137 (2014) 014001.

[9] G. Wang, Y.J. Huang, M. Shagiev, J. Shen, Laser welding of $Ti_{40}Zr_{25}Ni_3Cu_{12}Be_{20}$ bulk metallic glass, Mater. Sci. Eng. A 541 (2012) 33–37.

[10] B.E. Carroll, R.A. Otis, J.P. Borgonia, J. Suh, R.P. Dillon, A.A. Shapiro, D.C. Hofmann, Z. Liu, A.M. Beese, Functionally graded material of 304L stainless steel and inconel 625 fabricated by directed energy deposition: characterization and thermodynamic modeling, Acta Mater. 108 (2016) 46–54.

[11] W.L. Johnson, J. Plummer, Is metallic glass poised to come of age? Nat. Mater. 14 (2015) 553–555.

[12] ASM International Handbook Committee, ASM Handbook: Properties and Selection: Irons, Steels, and High-performance Alloys, ASM International, 1990.

[13] J. Kim, Y. Kawamura, Dissimilar welding of $Zr_{41}Be_{23}Ti_{14}Cu_{12}Ni_{10}$ bulk metallic glass and stainless steel, Scr. Mater. 65 (2011) 1033–1036.

[14] S. Fukumoto, M. Minami, A. Soeda, M. Matsushima, M. Takahashi, Y. Yokoyama, K. Fujimoto, Microstructural development at weld interface between Zr-based glassy alloy and stainless steel by resistance microwelding, J. Phys.: Conf. Ser. 379 (2012) 012027.

[15] ASM International Handbook Committee, ASM Handbook: Alloy Phase Diagrams, ASM International, 1990.

[16] Y. Li, Y. Shen, C. Chen, M.C. Leu, H.L. Tsai, Building metallic glass structures on crystalline metal substrates by laser-foil-printing additive manufacturing, J. Mater. Process. Technol. 248 (2017) 249–261.

[17] I. Tomashchuk, D. Grevey, P. Sallamand, Dissimilar laser welding of AISI 316L stainless steel to Ti6–Al4–6V alloy via pure vanadium interlayer, Mater. Sci. Eng. A 622 (2015) 37–45.

[18] Q. Chu, M. Zhang, J. Li, C. Yan, Z. Qin, Influence of vanadium filler on the properties of titanium and steel TIG welded joints, J. Mater. Process. Technol. 240 (2017) 293–304.

[19] M.K. Lee, J.G. Lee, Y.H. Choi, D.W. Kim, C.K. Rhee, Y.B. Lee, S.J. Hong, Interlayer engineering for dissimilar bonding of titanium to stainless steel, Mater. Lett. 64 (2010) 1105–1108.

[20] W. Li, F. Liou, J. Newkirk, K.M.B. Taminger, W.J. Seufzer, Investigation on Ti6Al4V-V-Cr-Fe-SS316 multi-layers metallic structure fabricated by laser 3D printing, Sci. Rep. 7 (2017) 7977.

[21] S. Chen, M. Zhang, J. Huang, C. Cui, H. Zhang, X. Zhao, Microstructures and mechanical property of laser butt welding of titanium alloy to stainless steel, Mater. Des. 53 (2014) 504–511.

[22] I. Tomashchuk, P. Sallamand, H. Andrzejewski, D. Grevey, The formation of intermetallics in dissimilar Ti6Al4V/copper/AISI 316 L electron beam and Nd:YAG laser joints, Intermetallics 19 (2011) 1466–1473.

[23] C.H. Muralimohan, M. Ashfaq, R. Ashiri, V. Muthupandi, K. Sivaprasad, Analysis and characterization of the role of Ni interlayer in the friction welding of titanium and 304 austenitic stainless steel, Metall. Mater. Trans. A 47 (2015) 347–359.

[24] S. Nogami, J. Miyazaki, A. Hasegawa, T. Nagasaka, T. Muroga, Study on electron beam weld joints between pure vanadium and SUS316L stainless steel, J. Nucl. Mater. 442 (2013) S562–S566.

[25] J. Zhou, H.L. Tsai, P.C. Wang, Transport phenomena and keyhole dynamics in pulsed laser welding, ASME J. Heat Transf. 128 (2006) 680–690.

[26] ASM International Handbook Committee, ASM Handbook: Properties and Selection: Nonferrous Alloys and Special-purpose Materials, ASM International, 1990.

IV. MECHANICAL PROPERTIES OF ZR-BASED BULK METALLIC GLASS PARTS FABRICATED BY LASER-FOIL-PRINTING ADDITIVE MANUFACTURING

Yingqi Li, Yiyu Shen, Ming C. Leu, and Hai-Lung Tsai

Department of Mechanical and Aerospace Engineering, Missouri University of Science and Technology, Rolla, MO 65409, United States

ABSTRACT

The application of bulk metallic glasses (BMGs) has been traditionally limited to parts with small dimensions and simple geometries, due to the requirement of fast cooling during the conventional process of casting. This research exemplifies a promising additive manufacturing method, i.e., laser-foil-printing (LFP), to fabricate high-quality BMG parts with large dimensions and complex geometries. In this study, $Zr_{52.5}Ti_5Al_{10}Ni_{14.6}Cu_{17.9}$ BMG parts were fabricated by LFP technology in which MG foils are laser welded layer-by-layer upon a substrate. The mechanical properties of the fabricated BMG parts were measured using micro-indentation, tensile test and four-point bending test, and compared to as-cast BMG parts. Through LFP, as rapid cooling rates can be achieved, fully amorphous and nearly fully dense BMG parts without cracking have been successfully made. The glass transition temperature, crystallization temperature, and melting temperature of the fabricated parts are nearly the same as those of the as-cast parts. Additionally, the fabricated BMG parts exhibit mechanical properties, including micro-hardness, tensile strength, and flexural strength, comparable to the as-cast BMG parts.

1. INTRODUCTION

Metallic glasses (MGs), also known as amorphous alloys, are solid metallic materials with amorphous atomic structures [1]. MG can be formed if a molten metal is cooled down fast enough to avoid crystallization. Owing to the amorphous atomic structure and concomitant lack of grain boundaries or dislocations which are the "weak regions" of crystalline metals, MGs usually exhibit many exceptional properties, such as high strength (even an ultrahigh strength of over 5 GPa), hardness, elasticity, corrosion resistance, wear resistance, etc., compared to conventional crystalline metals [1,2].

The first MG, with a chemical composition of $Au_{75}Si_{25}$, was synthesized in 1960 by Duwez's group at Caltech [3]. Because metal atoms crystallize so rapidly, they developed rapid quenching techniques to cool the liquid metal down at very high rates of 10^5–10^6 K/s. Since then, a large number of studies on the conventional MGs fabricated by rapid quenching techniques, e.g., melt spinning method, have been carried out [4]. However, because of the required high cooling rate to obtain amorphous structure, conventional MGs could only be tens or hundreds of microns thick, which is too thin for most practical applications.

The thickness limitation was drastically reduced by the findings of bulk metallic glass (BMG) alloy compositions. BMGs are typically multicomponent alloys designed near deep eutectics which require much lower critical cooling rates (as low as ~ 0.1 K/s) to suppress crystallization during solidification [4]. Many kinds of BMG alloy compositions have been developed including Pd-based, Zr-based, Ti-based, Ni-based, Cu-based, Mg-based, Fe-based, etc. [5,6]. The dramatic decrease in the critical cooling rate has enabled the production of thicker MG parts, and a change in the production method from rapid quenching to copper mold casting. The critical plate thickness, which is defined as the largest plate thickness of glass formation achieved by copper mold casting, has reached > 10 mm for BMG systems based on Zr, Pd, Pt, Mg, La, Ni and Cu, and > 5 mm for BMG systems based on Fe, Co and Ti [7,8].

Although the critical cooling rates for glass formation have been significantly reduced, the thickness of as-cast BMG parts does not “proportionally” increase. For example, the critical cooling rate of $Zr_{52.5}Ti_5Al_{10}Ni_{14.6}Cu_{17.9}$ BMG, which is selected for this study, is ~ 10 K/s, but its critical plate thickness is only around 4 mm [8]. As heat at the internal locations of an ingot must be transferred by conduction to the outer surface and then dissipates to the surroundings, the center of an ingot has the lowest cooling rate. As long as the critical cooling rate can be achieved at the center of an ingot, the entire sample will be amorphous. The cooling rates inside the metal are controlled by its thermophysical properties (e.g., thermal conductivity). Generally, BMGs have lower melting temperatures and thermal conductivities than those of the major individual elements of the alloys [9]. For example, Zr-based BMGs have very low thermal conductivity (~ 7 W/m·K) as compared to that of the major elements in the alloy, e.g., Zr (~ 23 W/m·K). Heat cannot be rapidly conducted to the outer surface and then dissipated to the surrounding cooling medium, especially when the part has a large cross-section area. This greatly limits the fabrication of large-size BMG parts by casting. In addition, only a limited range of geometries can be fabricated through direct casting of BMGs, since ideal molding conditions demand slow filling of mold cavity, which is problematic when fast cooling is required for glass formation [2]. To exploit the potential of BMGs, there is a necessity to explore new processing techniques for the fabrication of complicated BMG parts with larger dimensions.

Laser-based additive manufacturing (AM) technology is a promising method to overcome the size and geometry limitations of BMG products imposed by casting. As a layer-by-layer manufacturing technology, AM has an intrinsic advantage of fabricating 3D parts with intricate geometries [10]. In addition, the requirement of high cooling rates can be decoupled from the part dimensions in AM as it fragments the “casting” process of a part into many thin layers [11]. Theoretically, as long as high cooling rates can be fulfilled in each layer, BMG parts of any dimension can be made. On the other hand, the heating and cooling rates of laser processing are usually very high (10^4–10^5 K/s), which highly facilitates the formation of amorphous layer and could even allow the processing of BMGs with weak glass-forming ability.

A number of studies have been conducted using laser-based AM to fabricate 3D BMG parts from Zr-based and Ti-based BMGs with large glass-forming ability as well as Fe-based BMGs with weak glass forming ability [11–24]. Most of these studies were conducted through selective laser melting (SLM). SLM uses metal powder as feedstock material and a part is made by melting selected areas of the powder bed pass-by-pass and layer-by-layer using a laser beam. SLM is widely used to build highly dense metallic parts, such as stainless steel [25], titanium [26,27], aluminum [28], etc. However, when using powder as feedstock to fabricate BMG parts, challenges exist to reduce the porosity and make the part fully amorphous at the same time as explained below. First, the powder bed density is not high, leading to as much as 40–50% free space [29]. One consequence of this free space is that the powder bed has much lower thermal conductivity than the bulk material. For example, the measured thermal conductivity of a 316L stainless steel powder bed is only about 0.3–5% of that of the bulk material [25]. Such low thermal conductivity is problematic for the processing of BMG which requires the heat to be removed rapidly. Hence, to suppress crystallization, small laser energy input is required. On the other hand, the gas present in the powder bed will significantly increase the possibility of forming pores. To fully melt powder and reduce porosity, higher laser energy input is usually desired; however, it might cause crystallization of BMG, especially in the heat-affected zone (HAZ). Pauly et al. have conducted a detailed parametric study on the SLM synthesis of $Zr_{52.5}Ti_5Al_{10}Ni_{14.6}Cu_{17.9}$ BMG with a focus on porosity and phase formation to identify the process window [11]. With the optimized parameters, fully amorphous parts with a relative density of up to 98.5% can be obtained. Through increasing energy input, higher relative density (99%) can be achieved; however, the parts were crystallized. Once crystallization occurs, cracks are easily formed since crystallized BMGs are usually brittle.

Metal foil is another kind of feedstock material that can be used for AM. For AM of BMG parts, metal foil has advantages over metal powder since foils have no pores inside while powders have empty spaces in between. First, the heating and cooling rates when using foil should be higher than those when using powder at the same or similar laser processing conditions because powder bed has very low thermal conductivity compared to foil [20,25]. Second, less effort is needed to reduce porosity when using foil because powder bed has lower density and consequent more entrapped gas than foil [20,30,31]. Hence, when using foil as feedstock, crystallization of BMG should be less likely to occur and parts with lower porosity can be achieved.

Therefore, to overcome the limitations caused by powder feedstock in AM of BMG, in this study, we utilize MG foil as feedstock using a newly developed AM technology, called laser-foil-printing (LFP), which has been previously demonstrated [20,32]. In LFP, 3D parts are fabricated through laser welding of metal foils layer-by-layer in selected areas and cutting along the contour of the welded areas. The objective is to further reduce the porosity of an additive manufactured BMG part without sacrificing its fully amorphous structure through using foil as feedstock. $Zr_{52.5}Ti_5Al_{10}Ni_{14.6}Cu_{17.9}$ BMG was selected for this study since it has excellent glass-forming ability and is commercially available. In addition, this BMG exhibits very high strength (a yield strength of ~1524 MPa), high hardness (Vickers ~563), large elasticity (~1.8%), and superior corrosion resistance to 316 stainless steel and titanium [33]. It has potential application in biomedical implants, medical devices, sporting goods, etc. We have demonstrated the capability of LFP technology to fabricate dense, crack-free and fully amorphous Zr-based BMG parts with 3D geometries and thicknesses exceeding the critical plate thickness in previous publications [20,22]. The present paper focuses on the mechanical properties of BMG parts fabricated by LFP, and compares them to as-cast parts, in order to demonstrate the potential of LFP for achieving high-quality BMG parts.

2. EXPERIMENTAL

The LFP process was used in this study. More details explaining the LFP process and the system developed for this technology at Missouri S&T can be found in our other publication [32]. To facilitate discussion below, a short description is given here. The

LFP system mainly consists of two lasers: a continuous wave fiber laser with 1070 nm wavelength for foil-welding and a pulsed UV laser with 355 nm wavelength and 30 ns pulse duration for foil-cutting. In the process of fabricating each layer, a metal foil is fixed upon a flat substrate by laser spot-welding, and then a laser raster-scan welding process is done to achieve the full fusion and bonding of foil in selected regions. After the laser welding is done, the workpiece is translated to the location under the UV laser beam. Then, the UV laser cuts the welded foil along the contour of the sliced cross section of the 3D part to be fabricated. After the laser cutting is completed, the foil left is removed and a fresh foil is placed on the top of the workpiece for fabricating the next layer. This procedure is repeated until the desired 3D part is completely built. The process is performed inside a chamber with Ar shielding gas.

In this study, $Zr_{52.5}Cu_{17.9}Ni_{14.6}Al_{10}Ti_5$ (at.%) MG foil was used as the feedstock (see Figure 1(a)). The MG foil was commercial grade alloy and was manufactured through slow melt spinning (produced by Liquidmetal Technologies, Inc.). Each layer of foil is 200 μm thick. Before the LFP process, the foil was slightly polished using 240 grit SiC paper followed by ethanol cleaning in order to remove possible surface oxides. Rectangular BMG parts were then fabricated by LFP on a Ti-6Al-4V substrate. To achieve a good bonding between the BMG part and the Ti substrate, two layers of pure Zr foil (200 μm thick for each layer) were firstly welded onto the substrate as the intermediate layers, as shown in Figure 1(b). After that, MG foils were welded layer-by-layer onto the workpiece to fabricate a BMG part (Figure 1(c)). More discussion on the dissimilar metals bonding between the BMG part and the Ti substrate can be found in our previous publication [22].

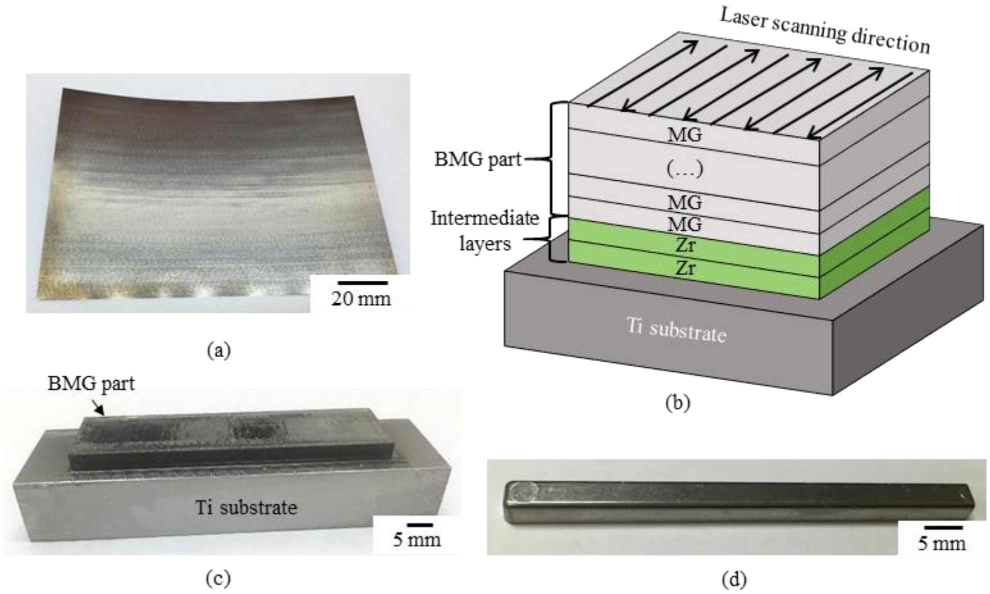

Figure 1. (a) MG foil used as the feedstock for LFP; (b) schematic of a LFP part building process; (c) a BMG part fabricated on a Ti substrate; (d) as-cast BMG beam.

For the welding of MG foil, the laser power (P = 500 W), the hatch space between two laser scanning passes (Δd = 0.15 mm), and the beam diameter (d = 170 μm) were kept constant. Crystallization of BMG during laser processing is related to laser energy input (E). For example, a 15 percent increase of laser energy input might lead to the formation of crystalline phases in $Zr_{52.5}Cu_{17.9}Ni_{14.6}Al_{10}Ti_5$ BMG [11]. In this study, $E = \frac{P}{v \cdot \Delta d \cdot t}$ [11], where v is the laser scanning speed and t is the layer thickness. Therefore, in this experiment, two laser scanning speeds were used, i.e., v = 500 mm/s and 350 mm/s, to achieve a relatively low energy input (E = 33 J/mm^3) and a relatively high energy input (E = 48 J/mm^3). The selected two energy inputs led to a fully amorphous part and a partially crystallized part. In addition, the above parameters were selected after parametric studies to ensure continuous, stable and sound welding passes.

After the BMG parts were built, they were cut from the substrates using wire electrical discharge machining (EDM) for characterization. For comparison, as-cast BMG parts with the same chemical composition were also characterized. The as-cast parts were also commercial grade alloy and were fabricated by injection molding (also produced by Liquidmetal Technologies, Inc.). It should be noted that except tensile test all other characterizations in the following were performed on as-cast beams that were 3.5 mm thick, 3.8 mm wide, and 60 mm long (see Figure 1(d)).

X-ray diffraction (XRD, Philips X'pert MPD) was used to characterize the formed phases. Optical microscopy (Nikon Epiphot 200) was performed on the cross-section of the LFP samples to analyze the microstructure and possible defects. The metallographic specimens for optical microscope analysis were first grinded using 240 grit and 600 grit SiC papers, and then polished using 9 μm and 3 μm diamond suspensions. This was followed by a final polishing with the application of 0.04 μm colloidal silica suspension. A differential scanning calorimeter (DSC, TA Instruments SDT Q600) was used to measure the glass transition temperature, crystallization temperature, and melting temperature at a heating rate of 20 °C/min. The densities of the cast part and the LFP parts were measured using Archimedean principle. The porosity was determined by the image analysis method using optical microscopy. The image analysis method measured the part's porosity by calculating the area fraction of pores on polished cross-sections.

The micro-hardness was measured using a Vickers micro-hardness tester (Struers, Duramin 5) with 500 g load and 10 s load duration. The tensile strength of the LFP part along the laser scan direction was tested. The dimensions of the tensile specimen can be found in [22], with a thickness of around 0.8 mm. The tensile specimens for the as-cast part were cut from a 0.75-mm-thick plate. 50-mm-long beams with 3 mm square cross-section were cut from the LFP part and the as-cast part using wire EDM for four-point bending test. The tension side of the four-point bending beam was ground to a final 600 grit surface finish, while other sides were ground to a 120 grit surface finish. The tensile and four-point bending tests were conducted on an INSTRON universal testing machine. The speed of the machine crosshead was maintained at 0.015 mm/mm/min for tensile test and 0.50 mm/min for four-point bending test. The tensile strain was measured by a clip-on extensometer, while the bending displacement was measured by the crosshead. The load span and the support span for the four-point bending test were 20 mm and 40 mm, respectively. All the samples were bent in the thickness direction. Three specimens were tested for each group, and the average value with one standard deviation was reported. After fracture, the specimens were investigated by scanning electron microscope (SEM, Hitachi S4700) and optical microscope to study the fracture surfaces and the fracture features.

3. RESULTS AND DISCUSSION

The XRD patterns of the cast sample, the foil feedstock, and the LFP samples are shown in Figure 2(a). The XRD pattern of the cast sample was obtained on the cross-section perpendicular to the length direction. For the LFP samples, the XRD analysis was conducted on the cross-section perpendicular to the laser scanning direction. The irradiation area of the X-ray beam was larger than 2×2 mm^2. Hence, the XRD result in Figure 2(a) is a representative of the entire sample. It can be seen that the XRD patterns of the foil feedstock, the cast sample and the LFP sample with E = 33 J/mm^3 all only show the characteristic broad peak from the amorphous structure, indicating that they are fully amorphous within the detection limit of XRD (~ 2%) [34]. For the LFP sample with E = 48 J/mm^3, its X-ray pattern shows the broad peak from the amorphous structure as well as several sharp Bragg peaks from crystalline phases, indicating that this sample is partially crystallized. Since there are five elements (Zr, Al, Ni, Cu, and Ti) involved and too few Bragg peaks detected, it is difficult to identify the possible crystalline phases present in this sample. The formed crystalline phases may be $NiZr_2$, $CuTi_3$, $AlZr_2$, Al_3Ti, etc.

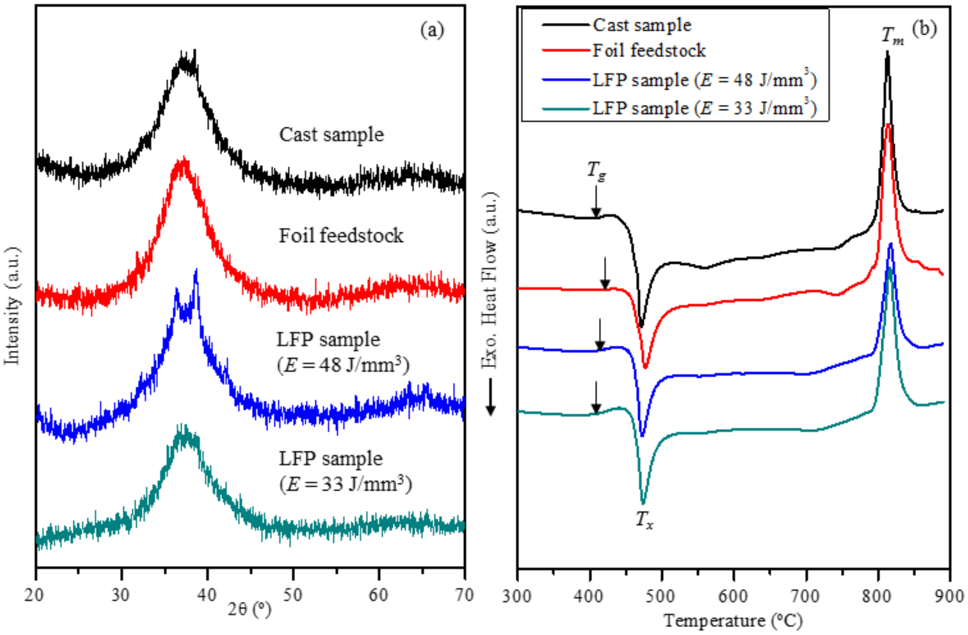

Figure 2. (a) XRD patterns and (b) DSC curves of the cast sample, foil feedstock, and LFP samples.

Figure 2(b) shows the DSC curves of the cast sample, the foil feedstock, and the LFP samples. The glass transition temperature (T_g), crystallization temperature (T_x), and melting temperature (T_m) measured through the DSC curves are summarized in Table 1. For the sake of simplicity, the maximum temperatures of the crystallization peak and the melting peak are used to define T_x and T_m, respectively. It can be seen that all samples show a glass transition around 400–410 °C. The T_x values of these samples are very close and are around 470 °C. In addition, all samples experienced melting around 810 °C. Several indicators that reflect the glass-forming ability of BMG, including the reduced glass transition temperature T_{rg} (= T_g / T_m), the supercooled liquid region ΔT_{xg} (= $T_x - T_g$), and γ (= T_x / (T_g + T_l), are calculated and also listed in Table 1. We can see that these indicators do not show apparent differences among these samples.

Table 1. Summary of T_g, T_x, T_m, T_{rg}, ΔT_{xg}, and γ determined from Figure 2(b).

Sample	**T_g (°C)**	**T_x (°C)**	**T_m (°C)**	**T_{rg} (= T_g / T_m)**	**ΔT_{xg} (= $T_x - T_g$)**	**γ (= T_x / (T_g + T_m))**
Cast sample	404	471	813	0.497	67	0.387
Foil feedstock	411	477	809	0.508	66	0.391
LFP sample (E = 48 J/mm^3)	407	472	817	0.498	65	0.386
LFP sample (E = 33 J/mm^3)	401	474	817	0.491	73	0.389

Figures 3(a) and 3(b) are the optical micrographs of the cross-sections from the bottom to the top surface of the LFP samples with E = 48 J/mm^3 and with E = 33 J/mm^3, respectively. The cross-sections of different locations were inspected by optical microscope, and Figures 3(a) and 3(b) just show the representative optical micrographs. For the LFP sample with E = 48 J/mm^3, visible pores were not observed from its cross-sections, while the cross-sections of the LFP sample with E = 33 J/mm^3 have few pores, as shown in Figure 3(b). Through using Archimedean principle, the density of the LFP part with *E* = 48 J/mm^3 was measured to be 6.668 ± 0.042 g/cm^3, while the LFP part with *E* = 33 J/mm^3 has a slightly lower density of 6.646 ± 0.036 g/cm^3. Both values are slightly higher than the measured density of the cast part which is 6.602 ± 0.039 g/cm^3. ImageJ software was used to measure the part porosity through calculating the area fraction of pores on the optical micrographs (same magnification as Figure 3(b)) of several cross-sections with a total area of ~ 10 × 3.5 mm^2. The measured porosity of the LFP part with *E* = 33 J/mm^3 is only ~ 0.1%, while the measured porosity of the LFP part with *E* = 48 J/mm^3 is zero (no pores).

In addition, cracking is not observed from the cross-sections of both LFP samples, although partial crystallization occurred in the LFP sample with *E* = 48 J/mm^3 (see Figure 2(a)). Figure 3(c) is the optical micrograph of the weld surface of the LFP sample showing the overlapped laser scanning passes. It can be seen that the weld surface of the LFP sample is smooth. The cross-sections of the LFP samples were then etched using a solution of 100 ml H_2O, 2 ml H_2O_2 and 0.1 ml HF to reveal their microstructures. For the LFP sample with *E* = 33 J/mm^3, its optical micrograph of the cross-section after etching, which is not shown here because it is similar to Figure 3(b), is featureless since this sample is fully amorphous, which is consistent with the XRD result (see Figure 2(a)). For the LFP sample with *E* = 48 J/mm^3, its optical micrographs of the cross-section after etching are shown in Figures 3(d) and 3(e). Small crystals (appear dark) are observed in the LFP sample with *E* = 48 J/mm^3, which disperse throughout the amorphous matrix (appears bright). The size of the crystals is around 7 µm. Using ImageJ, the area fraction of crystals for Figures 3(d) and 3(e) is calculated to be ~ 4%.

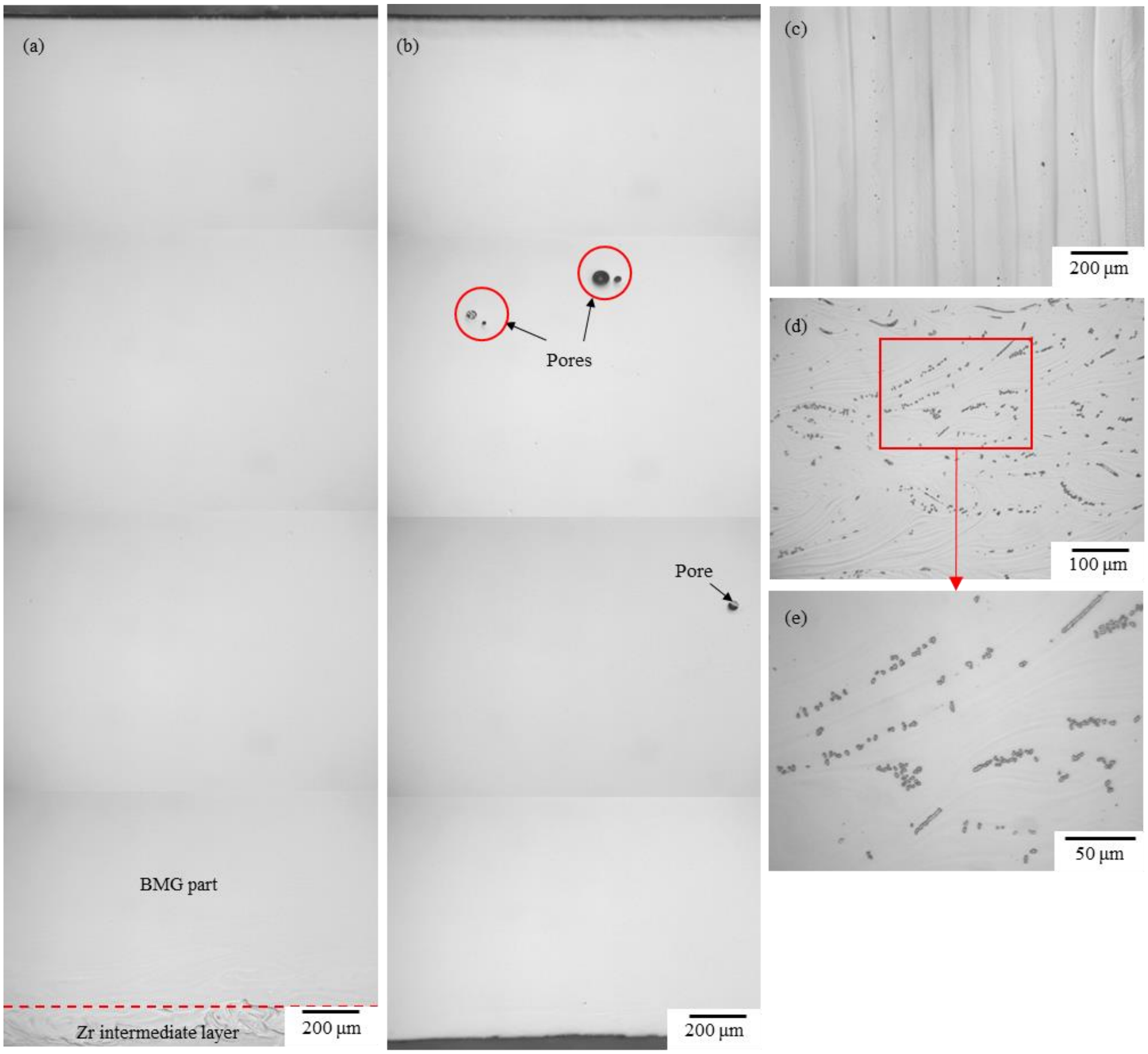

Figure 3. Optical micrographs of the LFP samples: (a) cross-section of the sample with *E* = 48 J/mm^3; (b) cross-section of the sample with *E* = 33 J/mm^3; (c) top surface showing the overlapped scanning passes; (d) and (e) magnified cross-section views of the sample with *E* = 48 J/mm^3 after etching showing the formed crystalline phases (dark) dispersing in the amorphous matrix (bright).

The crystals dispersing in the amorphous matrix (see Figure 3(d)) were induced by the complex thermal history that the part experienced during laser multi-pass and multi-layer processing. Figure 4 shows the calculated nucleation rate (*I*) and crystal growth rate (*U*) as a function of temperature for the selected BMG based on the classical nucleation theory [35]. The dash lines on Figure 4 represent the schematic thermal histories at the fusion zone (FZ) and heat-affected zone (HAZ) during laser welding. For this BMG, the maximum nucleation rate occurs at ~ 780 K, while the maximum growth rate occurs at ~ 1030 K and then drops rapidly to zero at T_m. During heating, nuclei generate in the amorphous matrix, and they will grow during further heating. If the heating rate is not high enough, they will grow to detectable crystals. Because of the fact that the maximum nucleation rate is at a lower temperature than the temperature of the maximum growth rate, in order to avoid a detectable crystallization during heating, the required heating rate is about two orders of magnitude higher (~ 10^3 K/s) than the critical cooling rate (~ 10 K/s) [2]. For the FZ, all nuclei and possible crystals formed during heating will be eliminated when melting occurs. In contrast, for the HAZ, all nuclei and possible crystals formed during heating will remain and keep growing during cooling. In addition, new nuclei will also form in both the FZ and HAZ during cooling. If the cooling rate is higher than the critical cooling rate, they will not grow to detectable crystals during cooling. In other words, a certain amount of nuclei will inevitably exist in the sample after each laser scanning, even if the sample does not show any detectable crystal under XRD or optical microscopy examination. The density of the formed nuclei is determined by the heating and cooling rates. Higher heating and cooling rates result in lower nuclei density.

During scanning subsequent passes or welding subsequent layers, the nuclei existing in the nearby area or previous layers are heat-affected and may grow to detectable crystals if they are exposed to a high temperature region where the growth rate is large with enough time (see Figure 4). On the other hand, the nuclei density will affect the position of the time-temperature-transformation (TTT) diagram which depicts the time until crystallization begins for a given temperature on the time axis. The critical cooling rate and required heating rate to avoid crystallization can be determined from TTT diagrams. Generally, the higher nuclei density will lead the TTT diagram shifting to shorter times, increasing the ability to crystallize. The critical cooling rate and required heating rate to avoid crystallization increase accordingly. More details about the effect of nuclei density on the crystallization behavior of this BMG during laser welding will be discussed in our other publication. Therefore, in laser processing, lowering energy input is necessary to reduce the nuclei density and suppress crystal growth.

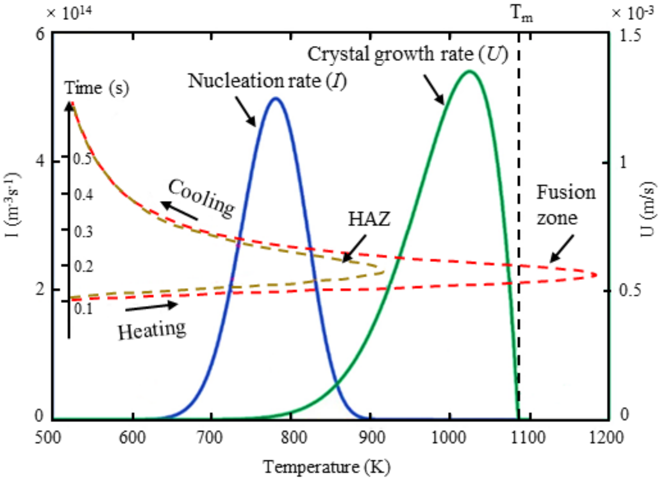

Figure 4. The calculated nucleation rate and crystal growth rate as functions of temperature. Dash lines: schematic thermal histories at fusion zone and HAZ. Adapted from Ref. [35].

Micro-hardness, tensile and four-point bending tests were then conducted to evaluate the mechanical properties of the LFP samples. The micro-hardness values of the cast sample and the LFP samples are listed in Table 2. The reported micro-hardness value is an average of ten measurements with one standard deviation. The micro-hardness value of the cast sample averages to 549 HV. The LFP sample with E = 33 J/mm^3, which is fully amorphous, has nearly the same micro-hardness value as the cast sample. For the LFP sample with E = 48 J/mm^3, which is partially crystallized, its micro-hardness value is around 579 HV, which is slightly higher than those of the cast sample and the LFP sample with E = 33 J/mm^3. The increased micro-hardness of the LFP sample with E = 48 J/mm^3 is caused by the formation of crystals in the amorphous matrix. The formed crystalline phases are intermetallic compounds (see Figure 2(a)) which are usually harder than the amorphous phase [22].

Table 2. Micro-hardness, ultimate tensile strength, and maximum flexural strength of the cast sample and LFP samples.

Sample	**Cast sample**	**LFP sample (E = 48 J/mm^3)**	**LFP sample (E = 33 J/mm^3)**
Micro-hardness ($HV_{0.5}$)	549 ± 11	579 ± 11	551 ± 18
Ultimate tensile strength (MPa)	1791 ± 30	1856 ± 17	1796 ± 60
Maximum flexural strength (MPa)	2096 ± 212	2096 ± 108	2186 ± 109

Figure 5(a) shows the representative tensile stress–strain curves of the cast sample and the LFP samples. The ultimate tensile strength (UTS) with one standard deviation values are summarized in Table 2. It can be seen that the LFP sample with E = 33 J/mm^3 exhibits nearly the same UTS as the cast sample, which is 1791 ± 30 MPa. Similar to the micro-hardness results, the UTS of the LFP sample with E = 48 J/mm^3, which is 1856 ± 17 MPa, is also slightly higher than those of the cast sample and the LFP sample with E = 33 J/mm^3. This might be caused by the strengthening effect of the crystalline phases [36].

In addition, all the samples nearly show zero tensile ductility and exhibit catastrophic fracture. The total tensile strain prior to fracture is about 1.2%.

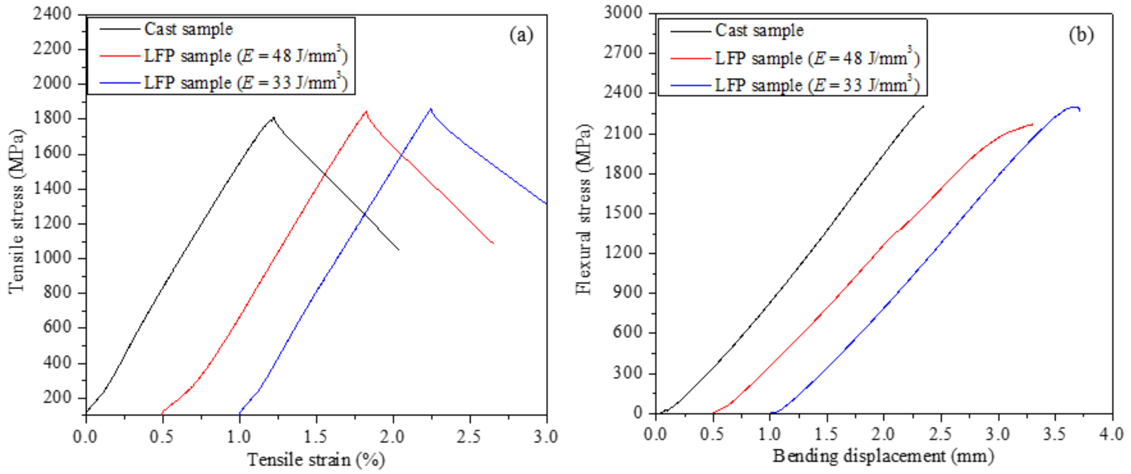

Figure 5. (a) Tensile stress–strain curves and (b) flexural stress–bending displacement curves of the cast sample and LFP samples. Note the curves have been offset in the x-axis for clarity.

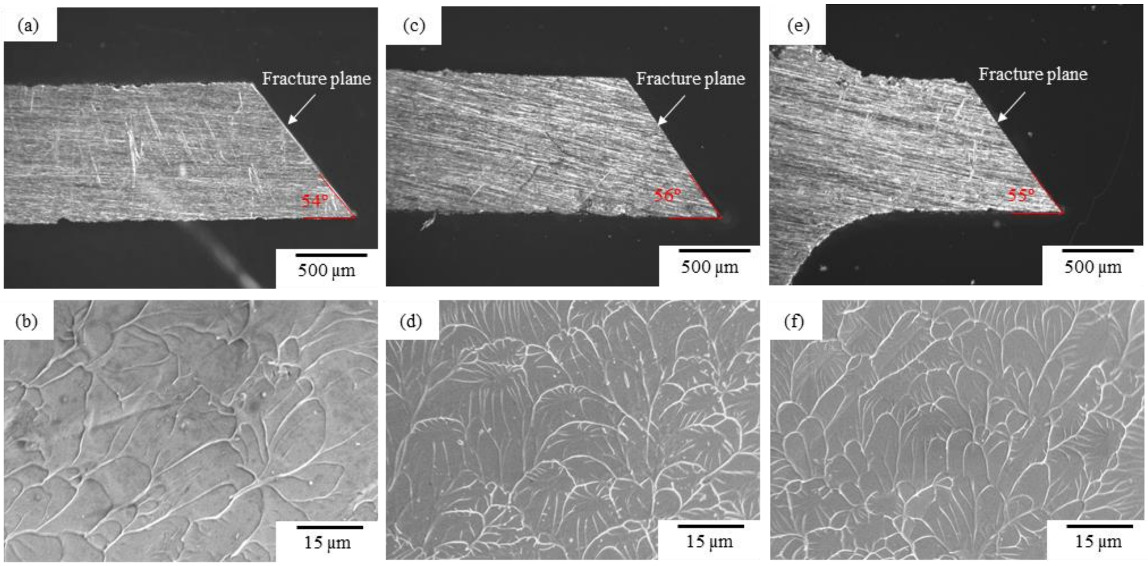

Figure 6. Optical micrographs (the first row) showing the shear fracture and SEM images showing the fracture surfaces (the second row) of the tensile specimens: (a) and (b) cast sample; (c) and (d) LFP sample with E = 48 J/mm^3; (e) and (f) LFP sample with E = 33 J/mm^3.

The optical micrographs in Figure 6 show that the tensile specimens of the cast sample and the LFP samples all fractured in a shear mode. The formation and propagation of one major shear band dominated the fracture process during tensile test. The lack of tensile ductility of BMG is caused by the free and rapid propagation of the shear band since there are no microstructure or other stabilizing features to arrest the slipping shear band [37]. As shown in Figures 6(a), 6(c) and 6(e), the tensile fracture angle between the tensile axis and the fracture plane is measured around 55º for all samples. This fracture angle deviates from the angle of the maximum shear stress plane which is 45º. It might be caused by the effect of normal tension stress acting on the fracture plane that can promote the shear fracture of BMGs, and the larger fracture angle corresponds to a higher normal tension stress [38]. The SEM micrographs of the fracture surfaces are shown in Figures 6(b), 6(d) and 6(f). It can be seen that the fracture surfaces are relatively smooth and they all exhibit a vein pattern which is the characteristic tensile or compression fracture morphology of BMGs. The vein pattern was attributed to temperature rise and subsequent local melting within the shear band induced by the high elastic energy in instantaneous fracture [38,39]. Due to the melting of MG within the shear band, the molten MG easily flows and appears in a vein pattern.

In addition to tensile strength, flexural strength was also measured through four-point bending test. The maximum flexural strength values of the cast sample and the LFP samples are summarized in Table 2. Figure 5(b) shows the typical flexural stress–bending displacement curves of the cast sample and the LFP samples. We can see that the LFP sample with E = 48 J/mm^3 has the same maximum flexural strength as the cast sample, which is averaged to 2096 MPa. Unlike the tensile test results in which the LFP sample with E = 48 J/mm^3 demonstrates the highest UTS, the maximum flexural strength of the LFP sample with E = 33 J/mm^3 is the highest one and its average value is 2187 MPa. For all samples, the beams show limited plastic deformation prior to failure (see Figure 5(b)). Figure 7 shows the optical micrographs of the fractured four-point bending beams as viewed from the tension side. It can be seen that all samples show a winding crack path. In addition, many shear bands, which are perpendicular to the beam's length, are observed on the tension side. It should be noted that the scratches from the grinding are in the direction longitudinal to the beam.

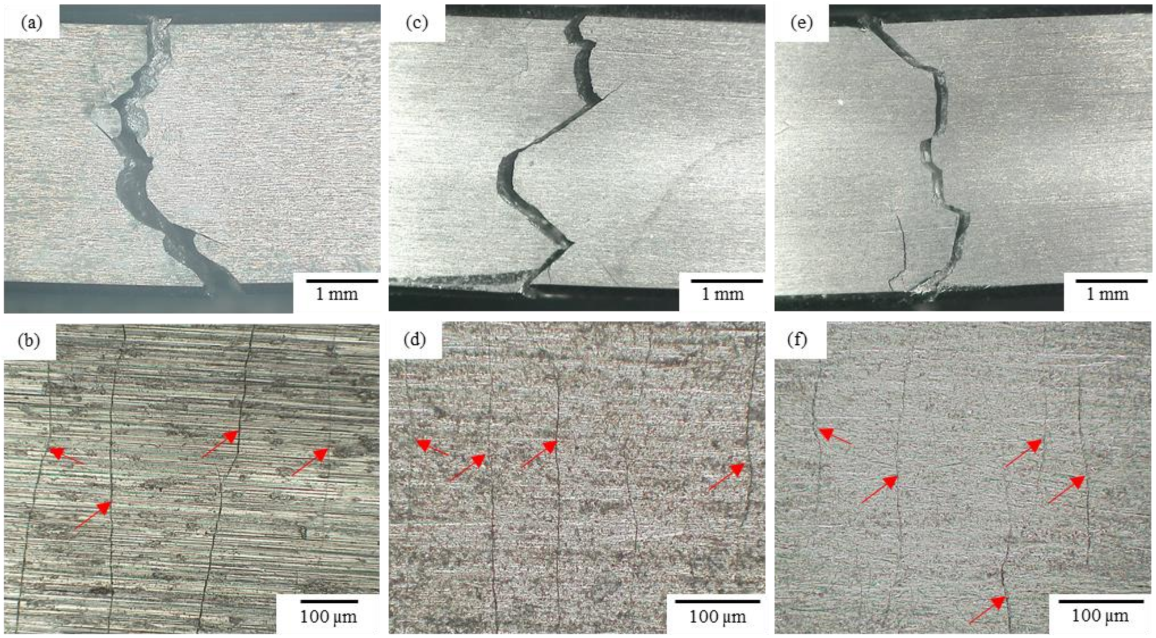

Figure 7. Optical micrographs of the fractured four-point bending beams as viewed from the tension side: (a) and (b) cast sample; (c) and (d) LFP sample with E = 48 J/mm^3; (e) and (f) LFP sample with E = 33 J/mm^3. Arrows indicate the most prominent shear bands.

From the above mechanical testing results, we can see that the LFP samples exhibit nearly the same mechanical properties as the cast sample. Even in the presence of a small amount of crystals (~ 4%), the LFP sample with E = 48 J/mm^3 still displays comparable or even higher strength in bending and tensile test than the cast sample, indicating that a small amount of crystals embedded in the amorphous matrix would not deteriorate the mechanical properties of the BMG parts [40]. However, if the volume fraction of crystalline phases in the BMG part is too high, the part will become very brittle [11,36,40].

4. CONCLUSIONS

$Zr_{52.5}Cu_{17.9}Ni_{14.6}Al_{10}Ti_5$ bulk metallic glass (BMG) parts were fabricated by laser-foil-printing (LFP) additive manufacturing. The mechanical properties of the LFP parts were measured and compared to parts made by conventional casting. The results show that LFP is able to produce fully amorphous BMG parts with nearly full density (~ 99.9%). The glass transition temperature, crystallization temperature and melting temperature of the LFP part are nearly the same as those of the cast part. The LFP sample with fully amorphous has a micro-hardness of 551 ± 18 HV, an ultimate tensile strength of 1796 ± 60 MPa, and a maximum flexural strength of 2186 ± 109 MPa, while the cast sample has a micro-hardness of 549 ± 11 HV, an ultimate tensile strength of 1791 ± 30 MPa, and a maximum flexural strength of 2096 ± 212 MPa. Even in the presence of a small amount of crystals (~ 4%), the partially crystallized LFP part still displays comparable or even higher strengths in bending and tensile tests than the cast part. This study demonstrates that LFP has a high potential for fabricating high-quality BMG parts with mechanical properties comparable to cast parts. The properties of the LFP parts can be further enhanced if the quality (purity, contamination, etc.) of the foil feedstock and the manufacturing technology (shielding chamber, cooling media, etc.) are improved.

ACKNOWLEDGEMENTS

This work was supported by the Department of Energy [grant number DE-FE0012272], the University of Missouri System [award number FastTrack-16002R], and the Intelligent Systems Center of Missouri S&T.

REFERENCES

[1] W.H. Wang, C. Dong, C.H. Shek, Bulk metallic glasses, Mater. Sci. Eng. R 44 (2004) 45–89.

[2] J. Schroers, Processing of bulk metallic glass, Adv. Mater. 22 (2010) 1566–1597.

[3] W.K. Jun, R. Willens, P. Duwez, Non-crystalline structure in solidified gold–silicon alloys, Nature 187 (1960) 869.

[4] M. Chen, A brief overview of bulk metallic glasses, NPG Asia Mater. 3 (2011) 82–90.

[5] A. Inoue, F.L. Kong, S.L. Zhu, E. Shalaan, F.M. Al-Marzouki, Production methods and properties of engineering glassy alloys and composites, Intermetallics 58 (2015) 20–30.

[6] A. Inoue, A. Takeuchi, Recent progress in bulk glassy, nanoquasicrystalline and nanocrystalline alloys, Mater. Sci. Eng. A 375–377 (2004) 16–30.

[7] A. Inoue, A. Takeuchi, Recent development and application products of bulk glassy alloys, Acta Mater. 59 (2011) 2243–2267.

[8] J. Na, G. Garrett, K. Han, G. Kaltenboeck, C. Crewdson, M.D. Demetriou, W.L. Johnson, Zirconium-titanium-copper-nickel-aluminum glasses with high glass forming ability and high thermal stability, US20170241006A1, US, 2017.

[9] M. Yamasaki, S. Kagao, Y. Kawamura, K. Yoshimura, Thermal diffusivity and conductivity of supercooled liquid in Zr41Ti 14Cu12Ni10Be23 metallic glass, Appl. Phys. Lett. 84 (2004) 4653.

[10] Y. Huang, M.C. Leu, J. Mazumder, A. Donmez, Additive manufacturing: current state, future potential, gaps and needs, and recommendations, ASME J. Manuf. Sci. Eng. 137 (2014) 014001.

[11] S. Pauly, C. Schricker, S. Scudino, L. Deng, U. Kühn, Processing a glass-forming Zr-based alloy by selective laser melting, Mater. Des. 135 (2017) 133–141.

[12] L. Deng, S. Wang, P. Wang, U. Kühn, S. Pauly, Selective laser melting of a Ti-based bulk metallic glass, Mater. Lett. 212 (2018) 346–349.

[13] H.Y. Jung, S.J. Choi, K.G. Prashanth, M. Stoica, S. Scudino, S. Yi, U. Kuhn, D.H. Kim, K.B. Kim, J. Eckert, Fabrication of Fe-based bulk metallic glass by selective laser melting: a parameter study, Mater. Des. 86 (2015) 703–708.

[14] X.P. Li, M.P. Roberts, S. O'Keeffe, T.B. Sercombe, Selective laser melting of Zr-based bulk metallic glasses: processing, microstructure and mechanical properties, Mater. Des. 112 (2016) 217–226.

[15] Z. Mahbooba, L. Thorsson, M. Unosson, P. Skoglund, H. West, T. Horn, C. Rock, E. Vogli, O. Harrysson, Additive manufacturing of an iron-based bulk metallic glass larger than the critical casting thickness, Appl. Mater. Today 11 (2018) 264–269.

[16] D. Ouyang, N. Li, L. Liu, Structural heterogeneity in 3D printed Zr-based bulk metallic glass by selective laser melting, J. Alloy. Compd. 740 (2018) 603–609.

[17] D. Ouyang, N. Li, W. Xing, J. Zhang, L. Liu, 3D printing of crack-free high strength Zr-based bulk metallic glass composite by selective laser melting, Intermetallics 90 (2017) 128–134.

[18] S. Pauly, L. Löber, R. Petters, M. Stoica, S. Scudino, U. Kühn, J. Eckert, Processing metallic glasses by selective laser melting, Mater. Today 16 (2013) 37–41.

[19] C. Yang, C. Zhang, W. Xing, L. Liu, 3D printing of Zr-based bulk metallic glasses with complex geometries and enhanced catalytic properties, Intermetallics 94 (2018) 22–28.

[20] Y. Shen, Y. Li, C. Chen, H.L. Tsai, 3D printing of large, complex metallic glass structures, Mater. Des. 117 (2017) 213–222.

[21] P. Bordeenithikasem, Y. Shen, H.L. Tsai, D.C. Hofmann, Enhanced mechanical properties of additively manufactured bulk metallic glasses produced through laser foil printing from continuous sheetmetal feedstock, Addit. Manuf. 19 (2018) 95–103.

[22] Y. Li, Y. Shen, M.C. Leu, H.L. Tsai, Building Zr-based metallic glass part on Ti-6Al-4V substrate by laser-foil-printing additive manufacturing, Acta Mater. 144 (2018) 810–821.

[23] Y. Li, Y. Shen, C.H. Hung, M.C. Leu, H.L. Tsai, Additive manufacturing of Zr-based metallic glass structures on 304 stainless steel substrates via V/Ti/Zr intermediate layers, Mater. Sci. Eng. A 729 (2018) 185–195.

[24] Y. Li, Y. Shen, C. Chen, M.C. Leu, H.L. Tsai, Building metallic glass structures on crystalline metal substrates by laser-foil-printing additive manufacturing, J. Mater. Process. Technol. 248 (2017) 249–261.

[25] L.C. Wei, L.E. Ehrlich, M.J. Powell-Palm, C. Montgomery, J. Beuth, J.A. Malen, Thermal conductivity of metal powders for powder bed additive manufacturing, Addit. Manuf. 21 (2018) 201–208.

[26] H. Attar, M. Calin, L.C. Zhang, S. Scudino, J. Eckert, Manufacture by selective laser melting and mechanical behavior of commerically pure titanium, Mater. Sci. Eng. A 593 (2014) 170–177.

[27] H. Attar, S. Ehtemam-Haghighi, D. Kent, M. Dargusch, Recent developments and opportunities in additive manufacturing of titanium-based matrix composites: a review, Int. J. Mach. Tool. Manuf. 133 (2018) 85–102.

[28] K.G. Prashanth, H.S. Shahabi, H. Attar, V.C. Srivastava, N. ellendt, V. Uhlebwinkel, J. Eckert, S. Scudino, Production of high strength $Al_{85}Nd_8Ni_5Co_2$ alloy by selective laser melting, Addit. Manuf. 6 (2015) 1–5.

[29] T.G. Spears, S.A. Gold, In-process sensing in selective laser melting (SLM) additive manufacturing, Integr. Mater. Manuf. Innov. 5 (2016).

[30] G. Jacob, A. Donmez, J. Slotwinski, S. Moylan, Measurement of powder bed density in powder bed fusion additive manufacturing processes, Meas. Sci. Technol. 27 (2016) 115601.

[31] T. DebRoya, H.L. Wei, J.S. Zuback, T. Mukherjee, J.W. Elmer, J.O. Milewski, A.M. Beese, A. Wilson-Heid, A. De, W. Zhang, Additive manufacturing of metallic components-process, structure and properties, Prog. Mater. Sci. 92 (2018) 112–224.

[32] C. Chen, Y. Shen, H.L. Tsai, A foil-based additive manufacturing technology for metal parts, ASME J. Manuf. Sci. Eng. 139 (2016), p. 024501.

[33] http://www.liquidmetal.com/when-am/.

[34] B.A. Sarsfield, M. Davidovich, S. Desikan, M. Fakes, S. Futernik, J.L. Hilden, J.S. Tan, S. Yin, G. Young, B. Vakkalagadda, K. Volk, Powder X-ray diffraction detection of crystalline phase in amorphous pharmaceuticals, Int. Cent. Diffr. Data (2006) 322–327.

[35] Y. Shen, Y. Li, H.L. Tsai, Evolution of crystalline phase during laser processing of Zr-based metallic glass, J. Non-Cryst. Solids 481 (2018) 299–305.

[36] J. Eckert, J. Das, S. Pauly, C. Duhamel, Mechanical properties of bulk metallic glasses and composites, J. Mater. Res. 22 (2011) 285–301.

[37] Z.F. Zhang, J. Eckert, L. Schultz, Difference in compressive and tensile fracture mechanisms of Zr59Cu20Al10Ni8Ti3 bulk metallic glass, Acta Mater. 51 (2003) 1167–1179.

[38] J. Qiao, H. Jia, P.K. Liaw, Metallic glass matrix composites, Mater. Sci. Eng. R 100 (2016) 1–69.

[39] M. Chen, Mechanical behavior of metallic glasses: microscopic understanding of strength and ductility, Annu. Rev. Mater. Res. 38 (2008) 445–469.

[40] Jittisa Ketkaew, Zr Liu, Wen Chen, Jan Schroers, Critical crystallization for embrittlement in metallic glasses, Phys. Rev. Lett. 115 (2015) 265502.

SECTION

2. CONCLUSIONS

In this dissertation, $Zr_{52.5}Cu_{17.9}Ni_{14.6}Al_{10}Ti_5$ metallic glass (MG) parts were fabricated on different crystalline metal substrates, including pure Zr metal, Ti-6Al-4V alloy, and 304L stainless steel, by laser-foil-printing (LFP) additive manufacturing. The MG parts were made by welding MG foils layer-by-layer onto the substrates. The dissimilar joints between the MG parts and different crystalline metals were studied and then improved by using appropriate intermediate layers. The microstructure, thermal properties, and mechanical properties of the fabricated MG parts by LFP were also characterized and compared to parts made by conventional casting. The major results are summarized as follows:

(1) Zr is a suitable substrate for Zr-based MG parts. Compared to other crystalline metals, Zr exhibits good compatibility and weldability with Zr-based MG. Under all tested parameters, crack-free weld joints between Zr and Zr-based MG can be obtained. In their bonding, soft α-Zr, instead of brittle intermetallics, were formed, which contributes to the sound joint between Zr and Zr-based MG.

(2) The direct bonding between Ti alloy and Zr-based MG is highly brittle due to the formation of various intermetallics. When directly building a MG part on the Ti substrate, the welded MG foil peeled off from the substrate before the part was built. The dissimilar bonding between Ti and Zr-based MG can be improved by using pure Zr foil as intermediate layers. The Zr intermediate layers prevented the direct interaction

between the MG part and the Ti substrate, and therefore the formation of undesirable intermetallic phases was avoided. With the use of Zr intermediate layers, the bonding strength between the printed MG part and the Ti substrate can reach 758 MPa.

(3) The direct joint between MG and stainless steel is highly brittle due to the formation of various hard and brittle intermetallics caused by the compositional mixing between stainless steel and MG, lack of solubility between different elements (i.e., Fe, Cr, Ni, Zr, Al, Cu, and Ti). By using a combination of V foils, Ti foils and Zr foils as intermediate layers, the joint between stainless steel and MG is significantly improved. Since the intermediate materials are highly compatible with the adjacent materials, and the contents of undesirable elements in each material are minimized through dilution, hard intermetallics are not detected in the joint. The main constituent phases of the joint are various solid solutions, e.g., V, βTi, αTi and αZr solid solutions. The tensile bonding strength of the SS–MG joint with V/Ti/Zr intermediate layers is about 477 MPa, and the tensile test specimen fractured in the V layers in a brittle manner.

(4) LFP is able to produce fully amorphous MG parts with nearly full density (~ 99.9%). The glass transition temperature, crystallization temperature and melting temperature of the LFP part are nearly the same as those of the cast part. The LFP sample with fully amorphous has a micro-hardness of 551 ± 18 HV, an ultimate tensile strength of 1796 ± 60 MPa, and a maximum flexural strength of 2186 ± 109 MPa, while the cast sample has a micro-hardness of 549 ± 11 HV, an ultimate tensile strength of 1791 ± 30 MPa, and a maximum flexural strength of 2096 ± 212 MPa. Even in the presence of a small amount of crystals (~ 4%), the partially crystallized LFP part still displays comparable or even higher strengths in bending and tensile tests than the cast part.

3. RECOMMENDATIONS FOR FUTURE WORK

Although the LFP technology has been invented and demonstrated for additive manufacturing of metallic parts, there is a lack of understanding of the fundamental physical processes, the underlying science of metallurgical structure, the properties of the fabricated parts, the printability of various engineering alloys, the origin of various defects and their remedies, the process control methods, the residual stress mitigation, etc. Extensive and deep studies on these aspects are needed to enable efficient production of high-performance parts and wider application of LFP.

In LFP of MG parts, the complex thermal history that the part experiences during laser multi-pass and multi-layer processing makes the crystallization behavior of MG become much more complicated than those in casting and in laser single-pass welding. Understanding the crystallization behavior of MG in LFP is crucial for the manufacture of fully amorphous MG parts and the selection of proper processing parameters to maintain the fully amorphous structure. In addition to experimental studies, computational modeling and simulation are needed to understand the complex crystallization behavior of MGs under complex thermal cycles.

For the fabrication of multi-material components by LFP, although the joints between Zr-based MG and Ti alloy or stainless steel have been improved from the aspect of bonding strength by using intermediate layers, the joints exhibited brittle fracture behaviors. In addition, the chemistry and microstructure fluctuated significantly in the dissimilar bonding. Additional studies are still needed to increase the plasticity and uniform the chemistry and microstructure of the dissimilar bonding.

BIBLIOGRAPHY

[1] W.H. Wang, C. Dong, C.H. Shek, Bulk metallic glasses, Materials Science and Engineering R 44 (2004) 45–89.

[2] M. Chen, A brief overview of bulk metallic glasses, NPG Asia Materials 3 (2011) 82–90.

[3] J. Schroers, Processing of bulk metallic glass, Advanced Materials 22 (2010) 1566–1597.

[4] M. Miller, P. Liaw, Bulk metallic glasses, Springer, New York, 2008.

[5] W.L. Johnson, J. Plummer, Is metallic glass poised to come of age?, Nature Materials 14 (2015) 553–555.

[6] A. Inoue, A. Takeuchi, Recent development and application products of bulk glassy alloys, Acta Materialia 59 (2011) 2243–2267.

[7] D.C. Hofmann, Designing bulk metallic glass matrix composites with high toughness and tensile ductility, Dissertation (Ph.D.), California Institute of Technology, 2009.

[8] A. Inoue, F.L. Kong, S.L. Zhu, E. Shalaan, F.M. Al-Marzouki, Production methods and properties of engineering glassy alloys and composites, Intermetallics 58 (2015) 20–30.

[9] A. Inoue, A. Takeuchi, Recent progress in bulk glassy, nanoquasicrystalline and nanocrystalline alloys, Materials Science and Engineering A 375–377 (2004) 16–30.

[10] Y. Huang, M.C. Leu, J. Mazumder, A. Donmez, Additive manufacturing: current state, future potential, gaps and needs, and recommendations, Journal of Manufacturing Science and Engineering 137 (2014) 014001.

[11] S. Pauly, C. Schricker, S. Scudino, L. Deng, U. Kühn, Processing a glass-forming Zr-based alloy by selective laser melting, Materials & Design 135 (2017) 133–141.

[12] J.M. William M. Steen, Laser material processing, Springer, London, 2010.

[13] L. Deng, S. Wang, P. Wang, U. Kühn, S. Pauly, Selective laser melting of a Ti-based bulk metallic glass, Materials Letters 212 (2018) 346–349.

[14] H.Y. Jung, S.J. Choi, K.G. Prashanth, M. Stoica, S. Scudino, S. Yi, U. Kuhn, D.H. Kim, K.B. Kim, J. Eckert, Fabrication of Fe-based bulk metallic glass by selective laser melting: a parameter study, Materials & Design 86 (2015) 703–708.

[15] X.P. Li, M.P. Roberts, S. O'Keeffe, T.B. Sercombe, Selective laser melting of Zr-based bulk metallic glasses: Processing, microstructure and mechanical properties, Materials & Design 112 (2016) 217–226.

[16] Z. Mahbooba, L. Thorsson, M. Unosson, P. Skoglund, H. West, T. Horn, C. Rock, E. Vogli, O. Harrysson, Additive manufacturing of an iron-based bulk metallic glass larger than the critical casting thickness, Applied Materials Today 11 (2018) 264–269.

[17] D. Ouyang, N. Li, L. Liu, Structural heterogeneity in 3D printed Zr-based bulk metallic glass by selective laser melting, Journal of Alloys and Compounds 740 (2018) 603–609.

[18] D. Ouyang, N. Li, W. Xing, J. Zhang, L. Liu, 3D printing of crack-free high strength Zr-based bulk metallic glass composite by selective laser melting, Intermetallics 90 (2017) 128−134.

[19] S. Pauly, L. Löber, R. Petters, M. Stoica, S. Scudino, U. Kühn, J. Eckert, Processing metallic glasses by selective laser melting, Materials Today 16 (2013) 37−41.

[20] C. Yang, C. Zhang, W. Xing, L. Liu, 3D printing of Zr-based bulk metallic glasses with complex geometries and enhanced catalytic properties, Intermetallics 94 (2018) 22–28.

[21] Y. Shen, Y. Li, C. Chen, H.L. Tsai, 3D printing of large, complex metallic glass structures, Materials & Design 117 (2017) 213–222.

[22] P. Bordeenithikasem, Y. Shen, H.L. Tsai, D.C. Hofmann, Enhanced mechanical properties of additively manufactured bulk metallic glasses produced through laser foil printing from continuous sheetmetal feedstock, Additive Manufacturing, 19 (2018) 95–103.

[23] Y. Li, Y. Shen, M. C. Leu, H.L. Tsai, Building Zr-based metallic glass part on Ti-6Al-4V substrate by laser-foil-printing additive Manufacturing, Acta Materialia 144 (2018) 810–821.

[24] Y. Li, Y. Shen, C.H. Hung, M.C. Leu, H.L. Tsai, Additive manufacturing of Zr-based metallic glass structures on 304 stainless steel substrates via V/Ti/Zr intermediate layers, Materials Science and Engineering A 729 (2018) 185–195.

[25] Y. Li, Y. Shen, C. Chen, M.C. Leu, H.L. Tsai, Building metallic glass structures on crystalline metal substrates by laser-foil-printing additive manufacturing, Journal of Materials Processing Technology 248 (2017) 249–261.

[26] T.G. Spears, S.A. Gold, In-process sensing in selective laser melting (SLM) additive manufacturing, Integrating Materials and Manufacturing Innovation 5 (2016).

[27] L.C. Wei, L.E. Ehrlich, M.J. Powell-Palm, C. Montgomery, J. Beuth, J.A. Malen, Thermal conductivity of metal powders for powder bed additive manufacturing, Additive Manufacturing 21 (2018) 201–208.

[28] G Jacob, A Donmez, J Slotwinski, and S Moylan, Measurement of powder bed density in powder bed fusion additive manufacturing processes, Measurement Science and Technology 27 (2016) 115601.

[29] T. DebRoya, H.L. Wei, J.S. Zuback, T. Mukherjee, J.W. Elmer, J.O. Milewski, A.M. Beese, A. Wilson-Heid, A.De, W. Zhang, Additive manufacturing of metallic components-Process, structure and properties, Progress in Materials Science 92 (2018) 112–224.

[30] C. Chen, Y. Shen, H.L. Tsai, A Foil-based additive manufacturing technology for metal parts, Journal of Manufacturing Science and Engineering 139 (2016) 024501.

[31] L.D. Bobbio, R.A. Otis, J.P. Borgonia, R.P. Dillon, A.A. Shapiro, et al., Additive manufacturing of a functionally graded material from Ti-6Al-4V to Invar: Experimental characterization and thermodynamic calculations, Acta Materialia 127 (2017) 133–142.

[32] J. Qiao, H. Jia, P.K. Liaw, Metallic glass matrix composites, Materials Science and Engineering R 100 (2016) 1–69.

[33] Z. Sun, ION, J. C. , Laser welding of dissimilar metal combinations, Journal of Materials Science 30 (1995) 4205–4214.

[34] B. Chen, T. Shi, G. Liao, Laser welding of $Zr_{41}Ti_{14}Cu_{12}Ni_{10}Be_{23}$ bulk metallic glass and zirconium metal, Journal of Wuhan University of Technology-Mater. Sci. Ed. 29 (2014) 786–788.

[35] B. Chen, T.L. Shi, M. Li, F. Yang, F. Yan, et al., Laser welding of annealed $Zr_{55}Cu_{30}Al_{10}Ni_5$ bulk metallic glass, Intermetallics 46 (2014) 111–117.

[36] Y. Kawahito, T. Terajima, H. Kimura, T. Kuroda, K. Nakata, et al., High-power fiber laser welding and its application to metallic glass $Zr_{55}Cu_{30}Al_{10}Ni_5$, Materials Science and Engineering B 148 (2008) 105–109.

[37] J. Kim, D. Lee, S. Shin, C. Lee, Phase evolution in $Cu_{54}Ni_6Zr_{22}Ti_{18}$ bulk metallic glass Nd:YAG laser weld, Materials Science and Engineering A 434 (2006) 194–201.

[38] J.H. Kim, C. Lee, D.M. Lee, J.H. Sun, S.Y. Shin, et al., Pulsed Nd:YAG laser welding of $Cu_{54}Ni_6Zr_{22}Ti_{18}$ bulk metallic glass, Materials Science and Engineering A 449–451 (2007) 872–875.

[39] B. Li, Z.Y. Li, J.G. Xiong, L. Xing, D. Wang, et al., Laser welding of $Zr_{45}Cu_{48}Al_7$ bulk glassy alloy, Journal of Alloys and Compounds 413 (2006) 118–121.

[40] D.V. Louzguine-Luzgin, G.Q. Xie, T. Tsumura, H. Fukuda, K. Nakata, et al., Structural investigation of Ni–Nb–Ti–Zr–Co–Cu glassy samples prepared by different welding techniques, Materials Science and Engineering B 148 (2008) 88–91.

[41] W. Pilarczyk, The investigation of the structure of bulk metallic glasses before and after laser welding, Crystal Research and Technology 50 (2015) 700–704.

[42] L. Shao, A. Datye, J. Huang, J. Ketkaew, S. Woo Sohn, et al., Pulsed laser beam welding of $Pd_{43}Cu_{27}Ni_{10}P_{20}$ bulk metallic glass, Scientific Report 7 (2017) 7989.

[43] N.H. Tariq, B.A. Hasan, J.I. Akhter, Evolution of microstructure in $Zr_{55}Cu_{30}Al_{10}Ni_5$ bulk amorphous alloy by high power pulsed nd:Yag laser, Journal of Alloys and Compounds 485 (2009) 212–214.

[44] H.D. Vora, S. Mridha, S. Katakam, H.S. Arora, S. Mukherjee, et al., Thermodynamics and kinetics of laser induced transformation in zirconium based bulk metallic glass, Journal of Non-Crystalline Solids 432 (2016) 237–245.

[45] G. Wang, Y.J. Huang, M. Shagiev, J. Shen, Laser welding of $Ti_{40}Zr_{25}Ni_3Cu_{12}Be_{20}$ bulk metallic glass, Materials Science and Engineering A 541 (2012) 33–37.

[46] H. Wang, H. Chen, J.S. Jang, Microstructure evolution in Nd:YAG laser-welded $(Zr_{53}Cu_{30}Ni_9Al_8)Si_{0.5}$ bulk metallic glass alloy, Journal of Alloys and Compounds 495 (2010) 224–228.

[47] H. Wang, M. Chiou, H.-G. Chen, J.S. Jang, J.-W. Gu, Microstructure evolution of the laser spot welded Ni-free Zr-based bulk metallic glass composites, Intermetallics 29 (2012) 92–98.

[48] H.S. Wang, H.G. Chen, J.S.C. Jang, M.S. Chiou, Combination of Nd:YAG laser and a liquid cooling device to $(Zr_{53}Cu_{30}Ni_9Al_8)Si_{0.5}$ bulk metallic glass welding, Materials Science and Engineering A 528 (2010) 338–341.

[49] H.-S. Wang, H.-G. Chen, J.S.-C. Jang, D.-Y. Lin, J.-W. Gu, Interfacial analysis of the ex-situ reinforced phase of a laser spot welded Zr-based bulk metallic glass composite, Materials Characterization 86 (2013) 242−249.

[50] H.-S. Wang, M.-S. Chiou, H.-G. Chen, J.S.-C. Jang, The effects of initial welding temperature and welding parameters on the crystallization behaviors of laser spot welded Zr-based bulk metallic glass, Materials Chemistry and Physics 129 (2011) 547−552.

[51] H.-S. Wang, Y.-Z. Su, J. Shian-Ching Jang, H.-G. Chen, A comparison of crystallization behaviors of laser spot welded Zr–Cu–Ag–Al and Zr–Cu–Ni–Al bulk metallic glasses, Materials Chemistry and Physics 139 (2013) 215−219.

[52] H.-S. Wang, J.-Y. Wu, Y.-T. Liu, Effect of the volume fraction of the ex-situ reinforced ta additions on the microstructure and properties of laser-welded Zr-based bulk metallic glass composites, Intermetallics 68 (2016) 87−94.

[53] C. Xia, L. Xing, W.-Y. Long, Z.-Y. Li, Y. Li, Calculation of crystallization start line for $Zr_{48}Cu_{45}Al_7$ bulk metallic glass at a high heating and cooling rate, Journal of Alloys and Compounds 484 (2009) 698−701.

[54] S. Kagao, Y. Kawamura, Y. Ohno, Electron-beam welding of Zr-based bulk metallic glasses, Materials Science and Engineering A 375 (2004) 312–316.

[55] J. Kim, Y. Kawamura, Electron beam welding of the dissimilar Zr-based bulk metallic glass and Ti metal, Scripta Materialia 56 (2007) 709–712.

[56] J. Kim, Y. Kawamura, Electron beam welding of Zr-based bmg/Ni joints: Effect of beam irradiation position on mechanical and microstructural properties, Journal of Materials Processing Technology 207 (2008) 112−117.

[57] J. Kim, Y. Kawamura, Dissimilar welding of $Zr_{41}Be_{23}Ti_{14}Cu_{12}Ni_{10}$ bulk metallic glass and stainless steel, Scripta Materialia 65 (2011) 1033–1036.

[58] http://www.liquidmetal.com/when-am/

VITA

Yingqi Li was born in Hunan, China. She received her B.E. degree and M.S. degree in Materials Science and Engineering from Taiyuan University of Technology, Shanxi, China, in 2012 and 2015, respectively. Yingqi Li joined the Laser-based Manufacturing Laboratory and the Innovative Additive Manufacturing Laboratory in August 2015, and started working on metal additive manufacturing with a focus on metallic glass and dissimilar metals bonding. In May 2019, she received her Ph.D. degree in Mechanical Engineering from Missouri University of Science and Technology, Rolla, Missouri, United States, advised by Prof. Ming C. Leu and Prof. Hai-Lung Tsai. During her Ph.D. studies, Yingqi Li published four journal papers and two conference papers. She was also the co-author of four journal papers, one conference paper, and one patent. In addition, Yingqi Li won the best paper award at the 28th Annual International Solid Freeform Fabrication Symposium (2017) and the second prize at the 14th Annual Missouri S&T Intelligent Systems Center Poster Presentation (2018).